Uncertainty Informed Integrated Computational Materials Engineering for Design and Development of Fatigue Critical Alloys

A Ph.D. Dissertation
Submitted to
The Academic Faculty

By

Gary F. Whelan

In Partial Fulfillment
of the Requirements for the Degree
Doctor of Philosophy in the
School of Materials Science and Engineering

Georgia Institute of Technology
December 2020

Uncertainty Informed Integrated Computational Materials Engineering for Design and Development of Fatigue Critical Alloys

Reading Committee:
Dr. David L. McDowell, Advisor
George W. Woodruff School of
Mechanical Engineering
Georgia Institute of Technology

Dr. Richard W. Neu
George W. Woodruff School of
Mechanical Engineering
Georgia Institute of Technology

Dr. Hamid Garmestani
School of Material Science and
Engineering
Georgia Institute of Technology

Dr. Laura P. Swiler
Optimization and Uncertainty
Quantification Dept.
Sandia National Laboratories

Dr. Yan Wang
George W. Woodruff School of
Mechanical Engineering
Georgia Institute of Technology

Date Approved: November 23rd, 2020

Acknowledgements

First and foremost, I would like to give my immense thanks to my Ph.D. advisor Dr. David McDowell for his exceptional guidance, vision, and patience over the course of my time are Georgia Tech. From the first day I met Dr. McDowell he was totally open to listening to what motivated me and what aspect of research I would like to focus on. At the same time he had the big picture vision to help guide my focus towards impactful areas within the scheme of the research being conducted by our group. As someone who values autonomy, but also appreciates constructive criticism and guidance when needed, I couldn't have asked for a better Ph.D. advisor than Dr. McDowell. He always seems to know the right times to lay back and let me work things out for myself or to step in and help guide me, while consistently having an open door whenever I needed anything.

I give special thanks to my dissertation committee, Dr. Richard W. Neu, Dr. Hamid Garmestani, Dr. Laura P. Swiler, and Dr. Yan Wang for taking the time and energy to read my dissertation and participating in my proposal and defense presentations. In particular I would like to give extra thanks to Dr. Laura Swiler who helped guide my research efforts with many valuable discussions and advice.

To my colleagues in the McDowell group, thank you for everything I have learned from you as well as for the great collaboration and friendship over these past several years. I would like to give special thanks to Krzysztof Stopka, who came to Georgia Tech at the same time as me in 2016 and who I have worked closely with on a major three year ONR project making up the bulk of each of our respective research efforts. Kris has been extremely reliable and I can honestly say I would not have been able to achieve the same degree of success that I have had in my research at Georgia Tech without his vital

collaboration and support. I would also like to thank Adrienne Muth and Aaron Tallman for each guiding me as senior members of the McDowell group when I arrived at Georgia Tech. Both Adrienne and Aaron have been a great source of knowledge and support both for the technical aspects of my research and for the important everyday life aspects of navigating graduate school. Lastly, I thank Luke Costello, Theodore Zirkle, Kevin Chu, Alex Selimov, Thomas Payne, Dr. Shuozhi Xu, Dr. Dengke Chen, and Dr. Tang Gu, all of whom made our workspace, MRDC 3338, a pleasant and productive work environment as well as providing motivation with their respective immense productivity and dedication to work and to being genuinely good people.

I give my deepest thanks to my partner, family, and friends to whom I owe endless gratitude for their emotional support. I would never be able to accomplish anything without the love and friendship that they provide. In particular, my dad, Gary Sr., encouraged and guided my decisions throughout my life as I chose to follow in his footsteps as a mechanical engineer and then further to choose my graduate degree program. My mom, Jeanette, has been a pillar of support throughout my life, teaching me to embrace hard work as well as compassion from a young age. My brothers, Oliver and Joshua, helped encourage and drive me and are always there if I need to talk. Finally, my partner, Lindsay Benson, who has been there for me every single day through the ups and downs as a constant and unmatched source of love and support.

This work was sponsored in part by the Office of Naval Research (ONR), under grant number N00014-17-1-2036. In addition, I am grateful for the support of the Carter N. Paden, Jr. Distinguished Chair in Metals Processing.

Table of Contents

Acknowledgements ..... **iii**

List of Tables ..... **viii**

List of Figures ..... **ix**

List of Equations ..... **xii**

List of Abbreviations and Symbols ..... **xiii**

Summary ..... **xvi**

Chapter 1: Introduction 1

1.1 Motivation 1

1.2 Key Concepts 2

1.3 Dissertation Outline 5

Chapter 2: Background 9

2.1 Alpha-Beta Titanium Alloys 9

2.2 Process-Structure-Property-Performance Mapping 11

2.3 Modeling Fatigue 13

2.4 Digital Representation of Microstructures 17

2.5 Uncertainty Quantification for ICME Workflows 19

2.6 Inductive Design Exploration Method 24

Chapter 3: Calibration, Sensitivity Analysis, and Importance Sampling Based Uncertainty Quantification for a Microstructure Sensitive ICME workflow in Fatigue Critical Applications 28

3.1 Uncertainty Quantification in PSPP Framework 28

3.2 Fatigue PSPP Mapping 29

3.3 Crystal Plasticity Finite Element Models for Ti64 and Al7075-T6 33

3.3.1 Ti64 Model 33

3.3.2 Ti64 Model Calibration 34

3.3.3 Al7075-T6 Model 39

3.3.4 Al7075-T6 Model Calibration 40

3.4 Fatigue Indicator Parameters 42

3.5 Sensitivity Analysis 46

3.5.1 Ti64 Sensitivity Analysis 46

3.5.2 Al7075-T6 Sensitivity Analysis 52

3.6 Weighted Sampling Based Uncertainty Quantification 63

3.7 Chapter Summary 68

Chapter 4: Epistemic Model Form and Model Parameter Uncertainty Quantification in ICME Workflows for Fatigue Critical Computational Modeling 69
4.1 Digital Twin for Material Systems 69
4.2 Digital Representation of Microstructures 71
4.3 Epistemic Uncertainty Quantification Methodology 72
4.4 Results and Discussion 74
4.4.1 SVE Convergence Study 74
4.4.2 Model Parameter Sensitivity 78
4.4.3 Uncertainty in Localized Response Resulting from Macroscale Informed Model Parameters 83
4.5 Chapter Summary 89
Chapter 5: Machine Learning-Enabled Aleatory Uncertainty Quantification for Modeling Structure-Property Linkages for Fatigue Critical Engineering Alloys Using an ICME Workflow 91
5.1 Uncertainty Quantification in Materials Design 91
5.2 Aleatory Uncertainty Quantification and Propagation Methodology 93
5.3 Results and Discussion 96
5.3.1 Ti64 PSPP Map 98
5.3.2 Uncertainty Quantification and Reduction for CPFEM Simulations 99
5.3.3 Training and Validation of Gaussian Process Surrogate Models 106
5.3.4 Propagation of Aleatory Microstructure Statistic Uncertainty 116
5.4 Chapter Summary 120
Chapter 6: Uncertainty Informed Inductive Design Exploration Method Case Study: Robust Design of Ti64 Microstructure for Multiaxial Fatigue Loading 122
6.1 Modern Simulation-Informed Materials Design 122
6.2 Methodology 123
6.2.1 Uncertainty Quantification 123
6.2.2 Inductive Design Exploration Method 125
6.2.3 Multiaxial Fatigue 131
6.3 Results and Discussion 132
6.3.1 Establishing a Deductive Structure-Property Path Using CPFEM Simulations for Ti64 Subjected to Multiaxial Fatigue 135
6.3.2 Training Gaussian Process Regression Models for Uncertainty Propagation through Structure-Property Linkages 142
6.3.3 Uncertainty Informed Inductive Design of Ti64 Microstructure for Multiaxial Fatigue Conditions 147
6.4 Chapter Summary 155

Chapter 7: Conclusions and Recommendations 157
7.1 Overview of Contributions 157
7.2 Recommendations for Future Work 160
7.2.1 Investigation of Constitutive Model Form Uncertainty 160
7.2.2 Extension of Uncertainty Quantification and Propagation Methodology to Process-Structure Models 161
7.2.3 Extension of Aleatory Uncertainty Quantification Framework to Quantify Uncertainty in Additional Key Microstructure Attributes 162
7.2.4 Utilization of Multiscale Experimental and Modeling Techniques to Reduce Epistemic Uncertainty 163
Appendix A: Crystal Plasticity Finite Element Models 165
A.1 Crystal Plasticity Framework 165
A.2 Ti64 Power Law Flow Rule Crystal Plasticity Model 166
A.3 Al7075-T6 Constitutive Model 171
References 175

List of Tables

Table 3.1. Calibration parameters for the Ti64 model. 39
Table 3.2. Constant parameters for Ti64 sensitivity analysis. 50
Table 3.3. Constant parameters for Al7075-T6 sensitivity analysis. 53
Table 3.4. Relative dimensions for rolled Al7075-T6. 54
Table 3.5. Texture sensitivity analysis parameters for Al7075-T6. 59
Table 4.1. Computational test parameters. 76
Table 4.2. Ti64 model parameters investigated in sensitivity study. 79
Table 4.3. FIP sensitivity analysis for model parameter intervals. 82
Table 4.4. Parameter combinations giving output interval bounds for predicted 99^{th} percentile extreme value FIPs. 85
Table 5.1. Computational simulation parameters. 97
Table 6.1. Computational simulation parameters. 135
Table 6.2. Noise in predicted 99th percentile extreme value FIPs with chosen ensemble. 142
Table A.1. Calibrated parameter values for Ti64 constitutive model at room temperature (partially adapted from [91]). 171
Table A.2. Calibrated parameter values for Al7075-T6 constitutive model at room temperature (adapted from [37]). 173

List of Figures

Figure 1.1. Workflow chart. 8
Figure 2.1. Three possible microstructures attainable in two phase titanium alloys (adapted from [52]). 10
Figure 2.2. Slip systems present in the HCP unit cell of titanium, adapted from Priddy et al. [53]. 10
Figure 2.3. Generalized process-structure-property-performance map [56]. 12
Figure 2.4. UQ of elastic modulus for two phase polycrystalline alloy resulting from uncertainty propagated from processing temperature represented as a random field [21]. 22
Figure 2.5. Dakota nested model approach for mixed UQ analysis (adapted from [18]). 24
Figure 2.6. Olson's concept of materials by design [55]. 25
Figure 3.1. Ti64 process-structure-property-performance map (informed by [52]). 31
Figure 3.2. Al7075-T6 process-structure-property-performance map (adapted from [57]). 32
Figure 3.3. Statistical volume element used for constitutive model calibration. 37
Figure 3.4. Calibrated results for the initial three cycles of loading of the Ti64 beta-annealed microstructure at room temperature with strain amplitude ε_a =0.8%, strain rate of 0.001s^{-1}. 38
Figure 3.5. Calibrated results for the initial 3 cycles of loading of the Ti64 β-annealed microstructure at room temperature with fully reversed strain amplitude ε_a =1.0%, strain rate of 0.0005 s^{-1}. 38
Figure 3.6. Al7075-T6 calibration verification with 1% strain amplitude. 41
Figure 3.7. Al7075-T6 calibration verification with 1.8% strain amplitude. 42
Figure 3.8. Ti64 statistical volume element (left) and a diagram of bands and sub band from one grain (right) [114]. 45
Figure 3.9. PSPP map for Ti64 sensitivity analysis. 48
Figure 3.10. Pole figures of crystallographic textures used in Ti64 sensitivity analysis. 48
Figure 3.11. Macroscopic stress-strain response of Ti64 with varied microstructure attributes: Alpha phase volume fraction (top), texture (bottom left), average grain size (bottom right). 50
Figure 3.12. FIP response for Ti64 sensitivity analysis: primary alpha phase volume fraction (top), texture (middle), and average grain size (bottom) plotted to show fit to Gumbel (left) and Fréchet (right). 51
Figure 3.13. Grain size PSPP path for Al7075-T6 material system sensitivity analysis. 54
Figure 3.14. Sample SVEs for (top left) equiaxed, (top right) 4:2:1 rolled, and (bottom) 7:1:1 grains. 55
Figure 3.15. Homogenized stress-strain curves for Al7075-T6 with varying grain aspect ratios and random texture. 56
Figure 3.16. Texture PSPP path for Al7075-T6 material system sensitivity analysis. 57
Figure 3.17. ODFs for various textures studied in Al7075-T6 material system. 57
Figure 3.18. Sample SVE for grain size sensitivity analysis, case 1. 58
Figure 3.19. Homogenized stress-strain curves for varying intensity of Cubic texture. 60
Figure 3.20. Homogenized stress-strain curves for varying intensity of BCS texture. 60
Figure 3.21. Homogenized stress-strain curves for cubic textured Al7075-T6 with varying grain aspect ratios. 62
Figure 3.22. Homogenized stress-strain curves for BCS textured Al7075-T6 with varying grain aspect ratios. 63

Figure 3.23. Statistical distributions of microstructure attributes for Ti64 with nominal grain size of 30 μm (top left), volume fraction of primary alpha phase of 0.30 (top right), and basal-transverse texture with varied intensity (bottom). 64
Figure 3.24. Output histograms of 99.5th percentile FS FIPs for Ti64. 65
Figure 3.25. FIP_{FS} response for nominal Ti64 microstructure and the upper and lower limits of 99.5^{th} percentile FIP_{FS} values plotted on a Fréchet distribution. 66
Figure 4.1. SVE size and number convergence study; predicted 99^{th} percentile extreme value FIPs for all sub-ensembles (top) and for just those sub-ensembles having at least 20 SVEs and 100 grains per SVE (bottom). 77
Figure 4.2. Macroscopic cyclic stress-strain response of Ti64 model for baseline and adjusted model parameters. 83
Figure 4.3. Predicted 99th percentile FIPs ordered for all 81 model parameter combinations. 84
Figure 4.4. Extreme value distribution of FIPs on Fréchet plot. 86
Figure 4.5. Extreme value distributions of upper and lower bounds of model parameter uncertainty with SVE convergence uncertainty limits. 86
Figure 4.6. Extreme value distribution of FIPs for four common textures of Ti64 with upper and lower bounds of uncertainty shown for random texture. 88
Figure 4.7. Pole figures of crystallographic textures used in Ti64 sensitivity analysis. 88
Figure 5.1. PSPP map for Ti64 used in fatigue critical applications with structure-property linkages considered in this work highlighted in green. 98
Figure 5.2. Simulated material volume in ensemble versus noise of predicted 99th percentile extreme value FIP response. 102
Figure 5.3. FIP thresholding versus noise in predicted 99th percentile extreme value FIP response for four common textures seen in Ti64. 105
Figure 5.4. 2D slice of (top) prior and (bottom) posterior distributions from random texture GP model predicting 99th percentile extreme value FIPs. 109
Figure 5.5. 2D surface plots of GP model predictions of 99th percentile predicted extreme value FIPs for random textured Ti64: (a) GP trained with less noisy data and (b) GP trained with more noisy data and next 5 adaptive samples shown in green, and (c) GP trained with more noisy data including additional training data chosen with adaptive sampling; (d) adjusted scores of GP models versus number of training data for noisy data models. 112
Figure 5.6. 2D surface plots of GP model predictions of 99th percentile extreme value FIPs for transverse textured Ti64: (a) GP model trained on data with initial less noisy dataset, (b) with additional adaptive sampling, and (c) with more noisy data, and (d) with additional training data chosen using adaptive sampling; (e) adjusted scores of GP models versus number of training data for noisy data models. 114
Figure 5.7. 2D surface plots of GP model predictions of yield strength for (left) random and (b) transverse textured Ti64. 115
Figure 5.8. Normal distributions for (left) average grain size, (right) volume fraction of primary alpha phase, and (bottom) both combined for a typical Ti64 alloy. 117
Figure 5.9. Output uncertainty distributions for predicted 99th percentile extreme value FIPs and predicted yield strength for sample Ti64 materials with (left) transverse texture and (right) random texture. 119
Figure 5.10. Schematic of uncertainty propagation workflow with Gaussian process surrogate models shown by blue boxes. 120
Figure 6.1. Comparison of optimal and robust solutions [51]. 126
Figure 6.2. Inductive design exploration method [97]. 128

Figure 6.3. The various function types, feasible space boundary types, and input spaces available in pyDEM [50]. 129
Figure 6.4. Examples of (left) SVE used in simulations for this work, and (right) pole figures of four crystallographic textures considered. 134
Figure 6.5. Stress-strain curves for all four textures considered with 0.60 volume fraction primary alpha phase and 30 micron average grain size for (top) 11-direction and (bottom) 22-direction. 137
Figure 6.6. Extreme value SBA FIP distributions for all four textures considered with 0.60 volume fraction primary alpha phase and 30 □m average grain size plotted on a Fréchet plot for both (top) uniaxial loading and (bottom) biaxial loading. 139
Figure 6.7. Bar graphs showing the properties of interest for all four crystallographic textures; (a) elastic stiffness for the 11-direction, (b) elastic stiffness for the 22-direction, (c) yield strength for the 11-direction, (d) yield strength for the 22-direction, (e) 10^{th} percentile extreme value FIPs for uniaxial loading conditions, (f) 10^{th} percentile extreme value FIPs for biaxial loading conditions, (g) 99^{th} percentile extreme value FIPs for uniaxial loading conditions, and (h) 99^{th} percentile extreme value FIPs for biaxial loading conditions. 141
Figure 6.8. Gaussian process regression models for predicting 99th percentile extreme value FIPs for each crystallographic texture and loading scenario across entire microstructure attribute space considered with adjusted LOOCV scores labeled; (a) random texture uniaxial loading, (b) random texture biaxial loading, (c) transverse texture uniaxial loading, (d) transverse texture biaxial loading, (e) basal-transverse texture uniaxial loading, (f) basal-transverse texture biaxial loading, (g) beta-annealed texture uniaxial loading, and (h) beta-annealed texture biaxial loading. 145
Figure 6.9. Example of distribution of aleatory microstructure statistic uncertainty and the associated uncertainty distribution in predicted 99^{th} percentile extreme value FIP response for random texture with uniaxial loading conditions. 146
Figure 6.10. Diagram illustrating outcomes of the inductive design process; (left) microstructure space includes achievable microstructure attributes in orange, desirable microstructure attributes in red, and the overlap of the two in green, and (right) the property space with corresponding achievable properties in orange, desirable properties in red, and the overlap in green. 148
Figure 6.11. Results of inductive design exploration using no uncertainty quantification across achievable microstructure space for all four crystallographic textures with yellow corresponding to viable microstructures that satisfy design constraints and purple corresponding to non-viable microstructures; (a) random texture, (b) transverse texture, (c) basal-transverse texture, and (d) beta-annealed texture. 149
Figure 6.12. Results of uncertainty informed inductive design exploration across achievable microstructure space for all four crystallographic texture. The color scale shows the level of robustness of each microstructure with 0.0 meaning there is no chance that it will satisfy the design constraints and 1.0 meaning that there is greater than 99% likelihood that it will satisfy the design constraints; (a) random texture, (b) transverse texture, (c) basal-transverse texture, and (d) beta-annealed texture. 152
Figure 6.13. Comparison of results from inductive design exploration with and without uncertainty quantification. Color scale shows robust microstructures in yellow (corresponding to a score of 2.0) , microstructures that appear nominally viable but are not robust in teal (score of 1.0), and microstructures that are neither robust nor nominally viable in purple (score of 0.0); (a) random texture, (b) transverse texture, (c) basal-transverse texture, (d) beta-annealed texture. . 154

List of Equations

(2.3.1) 15
(2.3.2) 16
(2.3.3) 17
(2.3.4) 17
(3.4.1) 46
(5.2.1) 95
(5.3.1) 103
(5.3.2) 103
(6.2.1) 130

List of Abbreviations and Symbols

BCC	Body-centered-cubic
BCS	Brass, Copper, Sulfur texture
BOR	Burgers orientation relationship
CPFEM	Crystal plasticity finite element method
CRSS	Critical resolves shear stress
EVD	Extreme value statistical distribution
FCC	Face-centered-cubic
FIP	Fatigue indicator parameter
FIP_{99}	Predicted 99^{th} percentile extreme value fatigue indicator parameters
GP	Gaussian process
GSA	Global sensitivity analysis
HCF	High cycle fatigue
HCP	Hexagonal-close-packed
ICME	Integrated computational materials engineering
IDEM	Inductive design exploration method
LCF	Low cycle fatigue
LEFM	Linear elastic fracture mechanics
LHS	Latin hypercube sampling
LOOCV	Leave one out cross validation
MC	Monte Carlo
MFU	Model form uncertainty
ML	Machine learning
MPU	Model parameter uncertainty
MSC	Microstructurally small crack
MSU	Microstructure statistic uncertainty

OEM	Original equipment manufacturer
PCE	Polynomial chaos expansion
PDF	Probability density function
PSC	Physically small crack
PSPP	Process-structure-property-performance
pyDEM	python inductive design exploration method
QoI	Quantity of interest
RMS	Root mean squared
RVE	Representative volume element
SVE	Statistical volume element
UMAT	User material subroutine
UQ	Uncertainty quantification
UQP	Uncertainty quantification and propagation
QFD	Quality function deployment

FIP_{FS}	Fatemi-Socie fatigue indicator parameter
$F_{Y_n}(y_n)$	Probability that the maximum value of a particular data set, Y_n is less than or equal to some critical value y_n
k	Fitting parameter for Fatemi-Socie FIP
R	Strain ratio for cyclic loading
u_n	characteristic length value for the Gumbel distribution
v_n	Characteristic value in the Fréchet distribution
w_n	Characteristic largest value in Weibull distribution
α_n	Measure of dispersion for the Gumbel distribution
ΔCTD	Range of cyclic crack tip displacement
ΔJ	Range of J-integral
$\Delta\gamma^p_{max}$	Maximum cyclic plastic shear strain range

ε_a	Strain amplitude for cyclic loading
θ	Measure of dispersion in the Fréchet or Weibull distribution
$(\kappa^{\alpha}_{s})_{t=0}$	Threshold softening term for the Ti64 model
$\sigma^{p}_{\max}$	Maximum normal stress acting on the plane of maximum cyclic plastic shear strain range
σ_y	Macroscopic yield strength
$\left(\tau^{\alpha}_{cr}\right)_{basal}$	Critical resolved shear stress in the basal plane
$\left(\tau^{\alpha}_{cr}\right)_{prism}$	Critical resolved shear stress in the prismatic plane
$\left(\tau^{\alpha}_{cr}\right)_{pyr\langle a\rangle}$	Critical resolved shear stress in the first order pyramidal plane
$\left(\tau^{\alpha}_{cr}\right)_{pyr\langle a+c\rangle}$	Critical resolved shear stress in the second order pyramidal plane
ω	Upper-bound of the initial Weibull distribution

Summary

Uncertainty is intrinsically tied to decision-making in design. Process-Structure-Property (PSP) relations are central to development of new and improved materials. The multitude of PSP linkages for any performance objective can be explored using the top down, inductive design exploration method (IDEM). Each PS and SP linkage has associated uncertainty, arising both from the types of models or interpretation of experimental results used to form linkages, as well as model parameters. These uncertainties can propagate and significantly affect the decision-making process in design and development of materials for specific performance targets. Uncertainty quantification (UQ) can be a highly computationally expensive undertaking in materials design and development. In this research, computationally efficient protocols are developed to effectively incorporate UQ in the IDEM. The uncertainty associated with PS linkages is assigned based on existing literature results. Gaussian process (GP) surrogate models are developed for the various SP linkages of interest as lower order approximations of computational expensive computational materials science simulations (e.g., the crystal plasticity finite element method (CPFEM)). These GP models are used to propagate uncertainty in microstructure attributes to the quantities of interest associated with properties that are then optimized in design. These surrogate models are integrated into existing python IDEM (pyDEM) protocols in the form of mapping functions. In this work, novel protocols are developed and demonstrated for uncertainty-informed design and development of Ti-6Al-4V and Al7075-T6 microstructures for targeted performance requirements involving combinations of fatigue resistance, elastic stiffness, and yield strength.

Chapter 1: Introduction

1.1 Motivation

Integrated computational material engineering (ICME) is a bold, transformative initiative calling for a paradigm shift in the way that materials design and development are approached at a fundamental level [1]. Traditional material science practices have emphasized a sequential approach to materials development that spans discovery to deployment and commonly takes 10 to 20 years. As a result of this long process of materials development, design engineers have traditionally selected from existing materials for a design, rather than designing and developing new, application specific materials [2]. ICME aims to accelerate the materials design and development process, focusing on modeling and simulations and their integration within the context of uncertainty, robust design, and information systems [3].

The work that has been carried out and presented in this dissertation aimed to develop novel integrated computational materials engineering workflows that can be utilized for the design of application specific fatigue critical metallic alloys, with particular attention to the role of uncertainty in providing support for decision-making. This has been accomplished by combining uncertainty quantification strategies and multi-objective optimization algorithms with microstructure sensitive crystal plasticity models implemented in finite element method simulations.

1.2 Key Concepts

One of the major difficulties in successfully using existing computational modeling capabilities in this space to accelerate materials development is the communication and understanding of the underlying materials science. Complex process-structure-property-performance (PSPP) linkages of a material system must be understood to develop and deploy computational models. To this end, a standard visual tool to communicate these relationships for a given application and material system was developed in the form of PSPP maps. These maps highlight causality relationships, as well as delineating independent variables [4]. A PSPP map also highlights the important process parameters that influence each relationship to clarify what phenomena modelers/experimentalists should focus on to develop application specific materials.

Uncertainty is introduced in material behavior from processing through performance stages of engineering components. Computational modeling of materials introduces unique uncertainties that differ from those encountered in experimental research. As such, there is a large body of research that rigorously couples uncertainty quantification with ICME workflows [5-14].

To facilitate UQ in the context of ICME, both the inherent, irreducible (i.e., aleatory) uncertainty in the system and uncertainty that can be reduced by increasing the knowledge of the system (i.e., epistemic) should be considered [5, 15-19]. Ma et. al. [20] proposed a hybrid method that simultaneously considers both uncertainty sources by employing a likelihood-based approach informed by a sparse statistical distribution. However, most research suggests that aleatory and epistemic uncertainty should be quantified independently by using statistical propagation and interval methods, respectively [21-23].

Many statistical methods have been explored for aleatory uncertainty quantification and propagation (UQP). Sandia National Laboratories' Dakota toolkit largely focuses on forward propagation of uncertainty [18]. However, UQP for statistical distributions presents a large computational burden owing to dimensionality [24], so reduced order surrogate models are used instead of high fidelity computational models. The surrogate modeling methods for UQP include Gaussian process (GP) regression models [6, 25-27], and stochastic expansion methods (e.g. polynomial chaos expansion (PCE), partial differential equations) [28-30]. Owen et. al. [31] found little difference in quality of UQP resulting from these surrogate approaches. However, GP regression models are more flexible, having no experimental design restrictions, and a much wider range of demonstrable behaviors beyond polynomial functions. Additionally, GP models provide quantification of uncertainty introduced by the surrogate model. The major drawback of GP models is that they lose efficiency high dimensional spaces – namely greater than 12 variables [32].

Uncertainty informed ICME is an emerging area in design and optimization for fatigue critical applications. Fatigue failures, though infrequent in modern engineering designs, are extremely costly. In a comprehensive study of fatigue, Reed et. al. estimated that about 4% of the gross domestic product in America is spent on fatigue related failures [33]. Fatigue failure requires a multiscale approach. Early research efforts in design for fatigue critical applications focused primarily on macroscale phenomena. One of the first successful efforts to characterize fatigue performance of materials was the stress-life approach, published by Wöhler [34] and later refined by Basquin [35]. However, deterministic macroscale approaches often fail to fully characterize the intricacies of

fatigue failure. Fatigue life of materials can exhibit variance or scatter over multiple orders of magnitude, depending on loading conditions. Moreover, several stages of crack growth with competing mechanisms must be considered to fully understand the relationship between material microstructure and fatigue performance.

Advanced computational models developed over the past few decades address fatigue crack formation and microstructurally small crack growth at the scale of microstructure [36-42], e.g., grains/phases. Mixed mode fatigue cracks are difficult to predict with traditional stress and strain metrics of fatigue life. Approaches considering the critical plane on which fatigue damage occurs have had more success. Fatemi and Socie [43] developed a damage parameter pertinent to fatigue crack initiation accounting for both plastic stress and strain averaged over a damage process volume at the mesoscale; this has been labeled as a Fatigue Indicator Parameter (FIP) [38].

Variability of fatigue response in materials primarily results from extreme statistical distributions of microstructure attributes that most heavily influence crack formation and growth. The Fatemi-Socie FIP, has been shown to converge to extreme value statistical distributions (EVDs) [44]. EVDs are a class of probability distributions that deal with extreme values when they are found in multiple sets of random variables. The theory of extreme value statistics was developed by Gumbel [45] in the 1950s and later shown to converge to only three possible non-degenerate distributions; Gumbel (type I), Fréchet (Type II), or Weibull (Type III) [46]. Only types I and II are relevant in the context of extreme value FIPs as the Weibull distribution requires a priori knowledge of upper limits of possible values, which cannot be determined for FIPs.

To build uncertainty informed decision-making workflows to assist design engineers in the development of fatigue critical engineering alloys, robust design is utilized. Robust design has gained widespread attention in ICME with applications in reliable decision-making for complex engineering systems [47], seeking solutions that are relatively insensitive to small changes in uncertain quantities [23]. The Inductive Design Exploration Method (IDEM) is an attractive approach for robust design that provides a computational workflow for generating robust design decision support in the face of uncertainty [48]. However, the present work focuses on updating the existing uncertainty quantification protocols included in the pyDEM computational environment [49] to reflect various state-of-the-art UQ methodologies.

PyDEM was developed to support python-scripted workflows that provide users the ability to explore optimization of materials for specific applications with an optimization strategy of their preference [50]. In materials design and development, achieving desired performance usually requires a tradeoff between conflicting goals. There is generally no clear optimal solution when one considers the effects of uncertainty. As such, Pareto optimal solutions are recommended when dealing with complex optimization problems [51]. In this work, combined types I, II, and III robust optimization will be demonstrated using newly developed UQ protocols in an IDEM framework.

1.3 Dissertation Outline

This dissertation consists of seven chapters. The present chapter provides an introduction to the motivation, scope, and concepts explored. Chapter 2 provides detailed

background on the state-of-the-art of relevant concepts in this work; PSPP mapping, modeling fatigue, digital representation of microstructures, uncertainty quantification for ICME, and IDEM. Chapters 3 through 6 detail the key technological advances developed in this work that are outlined by a generalized workflow chart for uncertainty quantification in ICME applied to fatigue critical engineering alloys shown in Figure 1.1.

Following the workflow outlined in Figure 1.1, Chapter 3 addresses steps 1, 2, and 3a. First, a PSPP map was developed for the material system. Here, Ti-6Al-4V (Ti64) was considered for aircraft gas turbine engine applications. Next, the SP linkages of interest were modeled and calibrated. A sensitivity analysis was carried out to understand the characteristics of the relationships and rank the sensitivity of the quantities of interest (QoIs) to each microstructure attribute and model parameter.

Chapter 4 is focused on epistemic uncertainty quantification and covers steps 4a, b, c, and d from the flow chart. Epistemic uncertainty was sub-categorized into model form and model parameter uncertainty. The model form uncertainty addressed in Chapter 4 consists of the study of ensembles of statistical volume elements (SVEs), and how the size and number of SVEs in an ensemble effect the uncertainty in QoIs. Model parameter uncertainty was addressed by quantifying the uncertainty introduced in the computation of FIPs by the method of calibrating constitutive model parameters for the crystal plasticity finite element method (CPFEM) model using experimental macroscopic stress-strain results. Aleatory and epistemic uncertainty were handled concurrently as shown by steps 3 and 4, respectively.

Chapter 5 is focused on steps 3b, 4d, and 5 in the flow chart. The goal of Chapter 5 was to establish a framework for the propagation of aleatory uncertainty in the form of

distributions of microstructure statistics as well as epistemic model form uncertainty. Each form of uncertainty was initially investigated independently, then the uncertainties were aggregated. Microstructure uncertainty was quantified using statistical distributions to represent experimental findings in existing literature, and epistemic uncertainty was reduced enough to facilitate the training of machine learning (ML) surrogate models. The ML model used GP regression and was built to propagate statistical microstructure uncertainty to QoIs.

Next, Chapter 6 was focused on integrating this uncertainty quantification and propagation (UQP) framework into pyDEM, with GP models employed as surrogate forms of mapping functions (informed by detailed computational models). Finally, this novel uncertainty informed decision-making framework was demonstrated with a materials design case study for Ti64 exposed to both uniaxial and multiaxial high cycle fatigue (HCF) loading conditions.

Lastly, Chapter 7 summarizes the major advances made in this work and provides recommendations for future work.

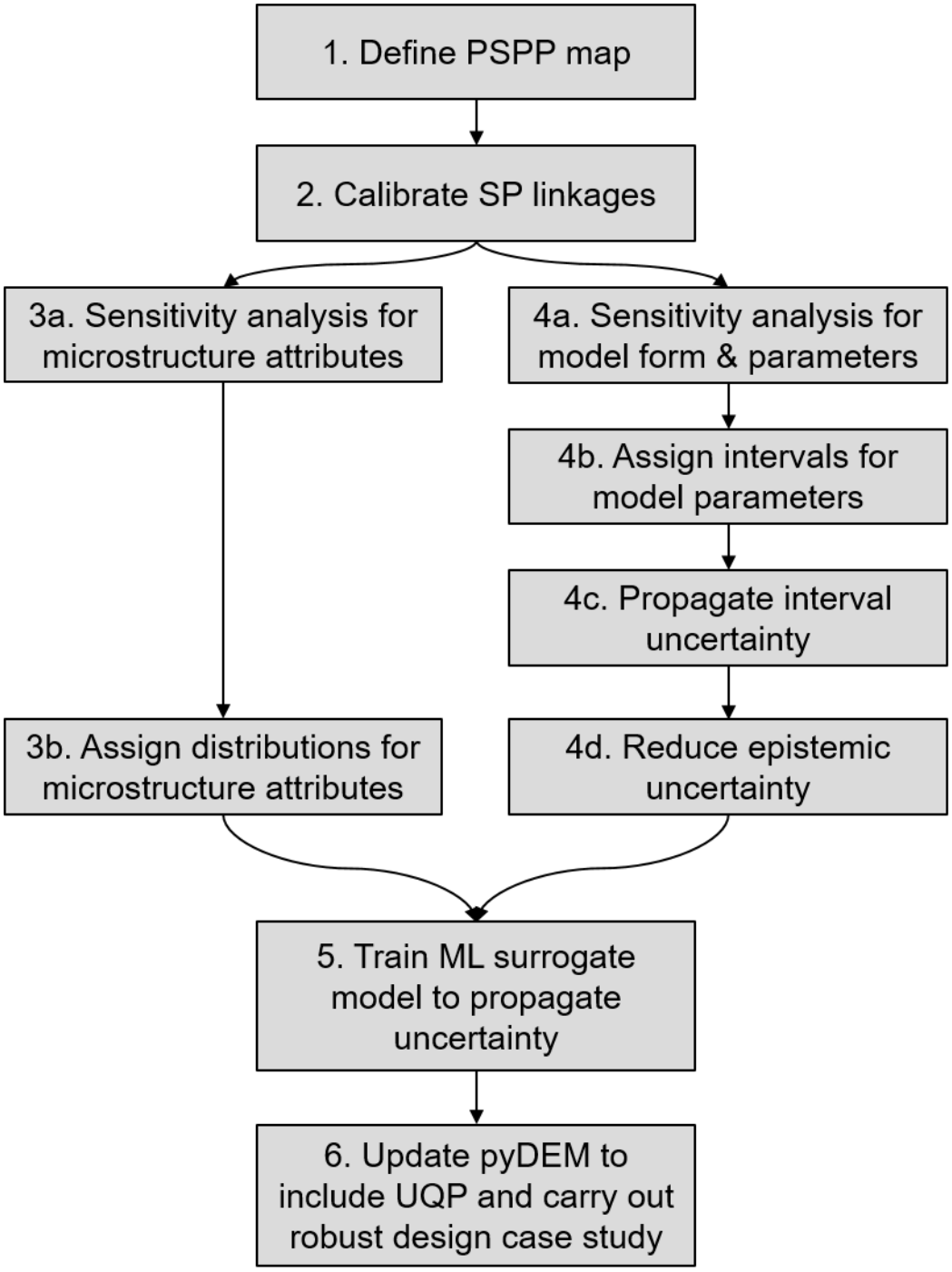

Figure 1.1. Workflow chart.

Chapter 2: Background

2.1 Alpha-Beta Titanium Alloys

Titanium alloys play an integral role in the aerospace industry for applications such as airframes and jet engine components because of their high strength-to-weight ratio, fatigue resistance, and resistance to corrosion. At 882C, pure titanium undergoes an allotropic phase transformation from hexagonal close-packed (HCP) crystal structure to body-centered cubic (BCC) crystal structure [52]. Some alloying elements (e.g. Al, O) added to pure titanium cause the transformation temperature of the resultant alloy to increase; these elements are known as α stabilizers. Other alloying elements (e.g. V, Mo) decrease the transformation temperature and they are known as β stabilizers. Ti64 is one of the most commonly used titanium alloys because of its balance of strength, ductility, fatigue, and fracture properties [52], which is mainly due to its balance of α and β stabilizers (Al and V, respectively).

Ti64 is a two phase titanium alloy where the α-phase has a hexagonal close packed crystallographic structure and the β-phase has a body centered cubic crystallographic texture. Two phase Titanium alloys can have one of three distinct microstructures attained by varying the manufacturing process: (i) Fully lamellar, (ii) bi-modal, and (iii) fully equiaxed [52]. These three microstructures are shown in Figure 2.1. All three microstructures are made up of two different types of grain; (i) lamellar α-β colony grains and (ii) primary α-phase grains. For the applications of interest, Ti64 tends to have a bi-modal microstructure with varying volume fractions of colony phase and primary alpha phase.

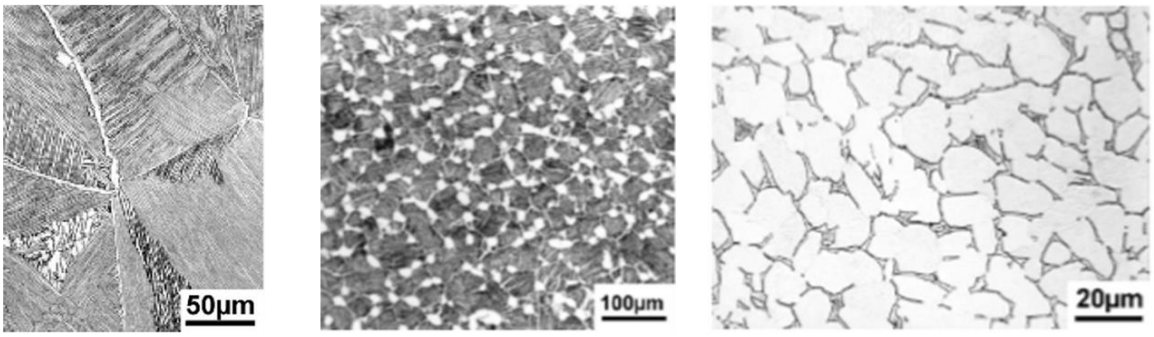

Figure 2.1. Three possible microstructures attainable in two phase titanium alloys (adapted from [52]).

Deformation in the HCP crystal structure is governed by four slip families: basal slip $\langle 11\bar{2}0\rangle(0001)$, prismatic slip $\langle 1120\rangle\{1010\}$, <a> pyramidal slip $\langle 11\bar{2}0\rangle\{10\bar{1}1\}$ and <a+c> pyramidal slip $\langle 11\bar{2}3\rangle\{10\bar{1}1\}$. These slip planes and their associated slip directions are depicted in Figure 2.2.

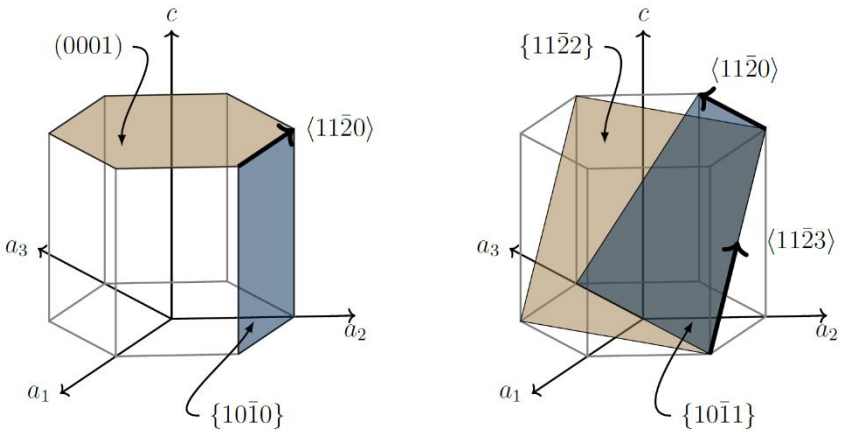

(a) Basal and Prismatic Slip **(b)** Pyramidal Slip

Figure 2.2. Slip systems present in the HCP unit cell of titanium, adapted from Priddy et al. [53].

In titanium and its alloys, prismatic slip has the smallest critical resolved shear stress (CRSS), followed by basal slip and then the pyramidal slip families [53]. Deformation

twinning can also be present in Ti alloys, but their presence is severely diminished at room temperature with an Al content above 6% [54]. In general, the BCC crystal structure has up to 48 slip systems, but it is common to only consider the twelve $\langle 111 \rangle \{110\}$ and twelve $\langle 111 \rangle \{112\}$ slip systems. BCC crystal structures also have twenty-four $\langle 111 \rangle \{123\}$ slip systems, but they can be very difficult to activate. Within the colony phase there exists a Burgers Orientation Relationship (BOR), between the colony secondary alpha and beta phase, which is defined as $(0001)_\alpha // \{101\}_\beta$ and $\langle 11\bar{2}0 \rangle_\alpha // \langle 111 \rangle_\beta$.

2.2 Process-Structure-Property-Performance Mapping

Traditional materials science and engineering practice has focused on reductionism, rather than a systems approach. With recent advances in computational tools, radical shifts can occur in the way material structure and properties are addressed in the design process. By considering how to tailor the material structure rather than selecting from a list of available materials, component level performance can be optimized and improved. One of the major impediments to this vision is the difficulty of communicating the complexities of structure of a hierarchical material system to engineers [55].

In design engineering, quality function deployment (QFD) tools are used to call attention to customer needs. These QFD tools provide a structured approach to define customer requirements and translate them to engineers in the form of engineering attributes. A PSPP map is an analogous system design chart for materials design that helps materials engineers easily identify important linkages [56]. PSPP maps identify key

microstructural subsystems, primary links of these subsystems to properties they control, and the stages of processing that govern their dynamic evolution [57]. Figure 2.3 provides a template illustrating the process of building such a map.

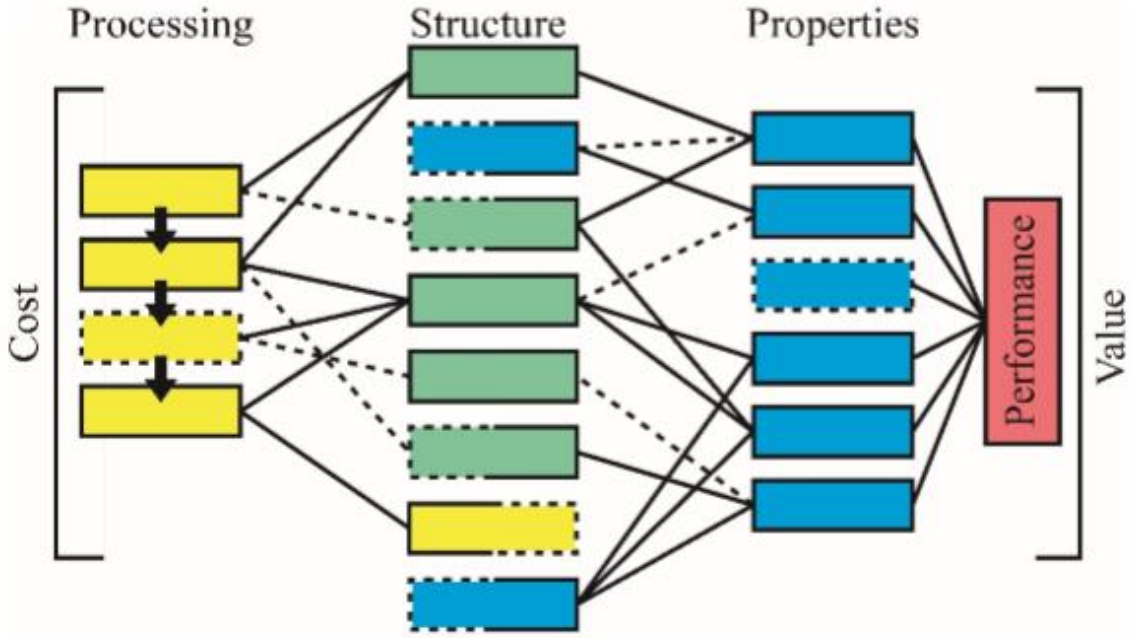

Figure 2.3. Generalized process-structure-property-performance map [56].

The first step to building a PSPP map is to identify the desired performance of the material. This performance solicits user identification of the properties of interest and their relation to structure attributes. Next, the available processing steps to produce this structure are sequentially listed in the leftmost column, along with their respective controllable parameters. The structure column is populated by listing microstructure attributes that are controlled by each processing step. If the nature of the linkage is well understood, a solid line is used. Conversely, if the nature of the linkage is not well understood, a dotted line is used to indicate that more research and development is needed to establish this linkage.

Structure attributes known to be linked to each property should be listed and linked as appropriate. Finally, the two independently built structure columns are rectified by combining boxes that exist in both lists and dashing half of the box where no links are known.

Given the multitude of physical and temporal length scales as well as vastly different properties of interest for the same material system being utilized for different applications, an important aspect to consider when building a PSPP map is the scope of the material design space that is desired. As a general guideline, maps should be large enough to capture all of the features, processing options, or properties of interest, but specific enough to be useful to the application at hand [57]. Ultimately, the structure scale and level of detail captured in the structure column sets the space for the PSPP map. In the present work the structure column considers mesoscale microstructure attributes as these have been shown to drive the properties of interest for fatigue critical applications as is described in more detail in the following two sections; Modeling Fatigue and Digital Representation of Microstructures.

2.3 Modeling Fatigue

Early research in materials design for fatigue critical components focused on phenomenological models informed by macroscale properties and loading conditions. One of the first successful characterizations of the fatigue life of materials is the stress life approach established by Wöhler [58] and built on by Basquin [35]. This approach is still used to estimate fatigue lives in many applications. However, deterministic macroscale

approaches often fail to fully characterize the intricacies of fatigue failure. Fatigue life of materials can exhibit variance or scatter over multiple orders of magnitude, depending on loading conditions. Moreover, several stages of crack growth with competing mechanisms must be considered to fully understand the relationship between material microstructure and fatigue performance. These early approaches, established prior to the development of fracture mechanics, acknowledged the eventual formation of cracks and 'failure' without addressing crack growth or failure conditions in detail [59].

Mechanically long crack growth in metals is typically well described using linear elastic fracture mechanics (LEFM) based on stress intensity factors [60]. However, for cracks that are mechanically short or small, the mechanics of fatigue crack growth may differ and are no longer well-described by LEFM [61]. Stages of fatigue cracking can be categorized as crack formation, microstructurally small crack (MSC) growth, and physically small crack (PSC) growth, finally giving way to LEFM-dominated behavior [59]. Crack formation occurs over a sub-grain size volume where the crack forms within one grain or at a cracked or debonded inclusion. MSCs are generally considered to extend from 3-10 grains, and PSCs up to about one millimeter [62], both depend on the applied stress amplitude and cyclic stress-strain behavior. Small fatigue crack formation and early growth within the first few grains is highly dependent on localized driving force, linked directly to the cyclic crystallographic slip intensity within the microstructure [63]. FIPs have been employed in both macro- and micro- scale fatigue studies to characterize driving forces for fatigue crack formation and early crack growth [64, 65].

FIPs intended to relate to transgranular fatigue crack formation are essentially local surrogate measures of driving force based on reversed slip intensity in a damage process

zone on the microscale. Brown and Miller [66] first discovered that the crack propagation process is best described by the plane on which the largest range of maximum plastic shear strain occurs. Building on this, Fatemi and Socie [43] developed a damage parameter that accounts for the cyclic maximum plastic shear strain averaged over the damage process volume at the mesoscale, with a mediating influence of the peak tensile stress normal to this plane, which we refer to as the Fatemi-Socie FIP, defined by

$$FIP_{FS} = \frac{\Delta\gamma^{p}_{\max}}{2}\left[1 + k\frac{\sigma^{p}_{\max}}{\sigma_{y}}\right] \qquad \textbf{(2.3.1)}$$

Here, $\Delta\gamma^{p}_{\max}$ is the maximum cyclic plastic shear strain range, $\sigma^{p}_{\max}$ is the maximum normal stress acting on the plane of maximum cyclic plastic shear strain range, σ_{y} is the macroscopic yield strength of the material, and k is a fitting parameter having a value between 0.5 and 1 [38].

In recent years, correlations of various FIPs with high fidelity experimental studies for transgranular small fatigue crack formation and early growth within polycrystals have been explored [65, 67], including variants of the particular FIP used throughout this work. Nicolas et al. [68] found that a variant of the Fatemi-Socie based FIP provided the sufficient information to support high confidence correlations, arguing on the basis of having introduced more variables than other candidate FIP measures considered; however, the preceding works on similarity of this FIP to mixed mode ΔJ [43] and the strong correlation with the range of cyclic crack tip displacement (ΔCTD) for small cracks at slip bands in

single crystals [69] suggest connection of these forms to mixed mode driving force (sliding and opening) for small transgranular fatigue cracks. Additional FIPs have been introduced for fatigue crack formation driven by slip impingement on grain or phase boundaries [70, 71].

When selecting a FIP, it is important to consider the deformation mechanism that leads to fatigue crack formation and early crack growth. FIPs have been shown to correlate well with both low cycle fatigue (LCF) and high cycle fatigue (HCF) lives to form a crack of a specified length for multiaxial fatigue crack initiation in various engineering alloys including Ni-based superalloy IN100 [44, 72-76], martensitic gear steels [77, 78], airframe aluminum alloys [36, 79-81], and titanium alloy Ti64 [82, 83].

Ultimately, the fatigue failure of engineering alloys is an extreme phenomenon that is initialized by local hot spots within the microstructure on the scale of the aforementioned damage process zones. Extreme value statistics [84] can be employed to describe the behavior of the maximum values of numerous sets of data and FIPs have been shown to converge to extreme value statistical distributions (EVDs) [44]. Extreme value statistics have been shown to converge to only three possible non-degenerate distributions; Gumbel (type I), Fréchet (Type II), or Weibull (Type III) [46] given by equations ***(2.3.2)***, ***(2.3.3)***, and ***(2.3.4)***, respectively. Only types I and II are relevant in the context of extreme value FIPs as the Weibull distribution requires a priori knowledge of upper limits of possible values, which cannot be determined for FIPs.

$$F_{Y_n}\left(y_n\right) = \exp\left[-e^{-\alpha_n\left(y_n-u_n\right)}\right] \qquad \textbf{(2.3.2)}$$

$$F_{Y_n}\left(y_n\right)=\exp\left[-\left(\frac{\nu_n}{y_n}\right)^{\theta}\right] \qquad \textbf{(2.3.3)}$$

$$F_{Y_n}\left(y_n\right)=\exp\left[-\left(\frac{\omega-y_n}{\omega-w_n}\right)^{\theta}\right] \qquad \textbf{(2.3.4)}$$

Here, $F_{Y_n}\left(y_n\right)$ is the probability that the maximum value of a particular data set, Y_n, is less than or equal to some critical value y_n. In the Gumbel distribution (Equation ***(2.3.2)***), α_n is a measure of dispersion and u_n is the characteristic largest value while θ is a measure of dispersion and v_n is the characteristic value in the Fréchet distribution (Equation ***(2.3.3)***). For the Weibull distribution, θ is a shape parameter or measure of dispersion and w_n is the characteristic largest value; ω is the upper-bound of the initial distribution, where $F_{\omega}=1$. The selection between the Gumbel and Fréchet extreme value model should be based on the distribution's ability to fit to the particular dataset at hand.

2.4 Digital Representation of Microstructures

Along with establishing appropriate models, it is important to digitally represent realistic microstructures having simulated volumes that are representative of those found in real material systems. In the present work, the concept of a synthetic microstructure will be used to describe volumetric instantiations described by a microstructure function and constructed from a set of target statistics, ideally quantified by direct observation of desired material systems. Due to the considerable cost of digitizing real microstructures using

methods such as serial sectioning and electron backscatter diffraction [85, 86] synthetic microstructures that have statistically equivalent attributes [87] to such materials are used in the present work.

In order to analyze the properties of interest for a range of microstructure variants and materials, ensembles of SVEs can be generated and CPFEM can be applied to crystal plasticity in ABAQUS [88]. There is an open-source tool called DREAM.3D [89] that digitally reconstructs or instantiates statistically realistic geometric representations of the grains comprising a polycrystal. This tool is widely used to generate SVEs for polycrystalline alloys such as those studied herein. A python pipeline was developed by Kern [90] that creates fully voxelated meshes and allows for user defined boundary conditions to utilize DREAM.3D microstructure instantiations in CPFEM simulations. In this implementation grain boundaries are introduced consistent with misorientation distribution targets using DREAM.3D; grain boundaries are impenetrable to slip in this particular formulation.

At each integration point, CPFEM simulations outputs include the 2^{nd} Piola-Kirchhoff stress, Green strain, and inelastic strain tensors based on cumulative shear on various slip systems, all in the intermediate isoclinic configuration of crystal plasticity [91]. Deformed configuration Cauchy stress is also obtained for each integration point. Likewise, the inelastic strain tensor is mapped into the current configuration. Common macroscopic polycrystal quantities of interest may be determined based on deformed configuration stress, elastic strain, and inelastic strain, such as elastic stiffness or yield strength. A statistically homogeneous Representative Volume Element (RVE) suitable for computing these stiffness or strength responses is relatively limited in size in terms of

number of grains/phases required for convergence (on the order of several hundred or thousands of grains). However, the concept of evaluating a RVE to compute surrogate fatigue crack formation driving forces (so-called Fatigue Indicator Parameters or FIPs) is not practical due when the property of interest is the minimum fatigue life (e.g., corresponding to maximum FIPs among a large population) [92, 93], as it would require a RVE of excessive size and high computational cost of simulations. Consequently, ensembles of SVEs are typically used to compute the statistical distribution of extreme value FIP response [38]; both the SVE size (sufficiently large to incorporate important nearest neighbor grain/phase spatial correlations) and number of SVEs in each ensemble of simulations needs to be determined to compute meaningful estimates of mean FIP responses along with their variance.

2.5 Uncertainty Quantification for ICME Workflows

Uncertainty Quantification (UQ) is concerned with providing specificity to the characterization of various forms of uncertainty, with application to both experimental and computational [94] sources. Uncertainty is manifested in all stages from materials processing through engineering component performance. Computational modeling of materials introduces unique uncertainties that differ from those encountered in experimental research. As such, there is a rapidly developing body of research that rigorously couples UQ with ICME workflows [5-7]. Recent advances in UQ for fatigue modeling [10, 11] have established the use of Bayesian and genetic algorithm techniques for crystal plasticity model parameter and model form UQ. Additionally, Bayesian inference and Taylor expansion based uncertainty propagation methods have been used to

propagate uncertainties associated with model reduction error, data sparsity error, and microstructural uncertainty using a crystal plasticity finite element modeling (CPFEM) model for dual phase alpha-beta titanium alloys [12, 14].

To facilitate UQ in the context of ICME workflows, both the inherent, irreducible (i.e., aleatory) uncertainty in the system and uncertainty that can be reduced by increasing the knowledge of the system (i.e., epistemic) should be considered [5, 15-19]. Uncertainty in ICME arises from several sources:

- Aleatory uncertainty consisting of **microstructure statistics uncertainty** (MSU) is the inherent uncertainty in the quantification of the various microstructure attributes. MSU results from natural stochasticity in microstructures that emerges from the PS linkages. Once quantified, it must be propagated through SP linkages to determine uncertainty in QoIs.

- Epistemic uncertainty consistently of **model form uncertainty** (MFU) **and model parameter uncertainty** (MPU). MFU is a combination of the uncertainty associated with the formulation of the constitutive model, the nature of the computational model (e.g., boundary conditions), numerical methods, meshing, convergence criteria, the number and size of SVEs used to compute distributions of FIPs, and model prediction uncertainty introduced when reduced order models are used as surrogates for more expensive high fidelity ICME models. MPU is the uncertainty resulting from limitation in calibrating parameters in the model based on the amount of data available. For example, if a constitutive model is only calibrated with one cyclic stress-strain dataset having a specific strain amplitude,

ratio, and rate, as well as one set of microstructure statistics, the model parameters selected may fit well to this data but perform less adequately with a different loading scenario.

Indeed many other sources of uncertainty exist. However, the forms described above are the focus of the present work.

Uncertainties are specified in terms of a probability density function (PDF) or interval bounds [23]. Intervals are an appropriate model to describe uncertainty when uncertain values range between specific known bounds with no additional information concerning variations, frequencies, preferences, etc. [95]. This is typical of MFU and MPU. Alternatively, PDFs are an appropraite model when the uncertainty of a varaible has known statistical characteristics, as is typically the case for MSU.

Cai and Mahadevan [22] used statistical methods to investigate uncertainty in the initial conditions and manufacturing process parameters on the microstructure and mechanical properties of materials. They propagate MSU to macroscopic mechanical properties of the material using computational models. This process is shown in Figure 2.4 for UQ of the elastic modulus resulting from uncertainty in temperature, which is presented as a spatially varying random field. In the study shown in Figure 2.4, this UQP framework was applied to a two phase polycrystalline alloy using a 2D computational model. Prior to the current work this methodology had not been applied for UQP related to local FIP responses in materials.

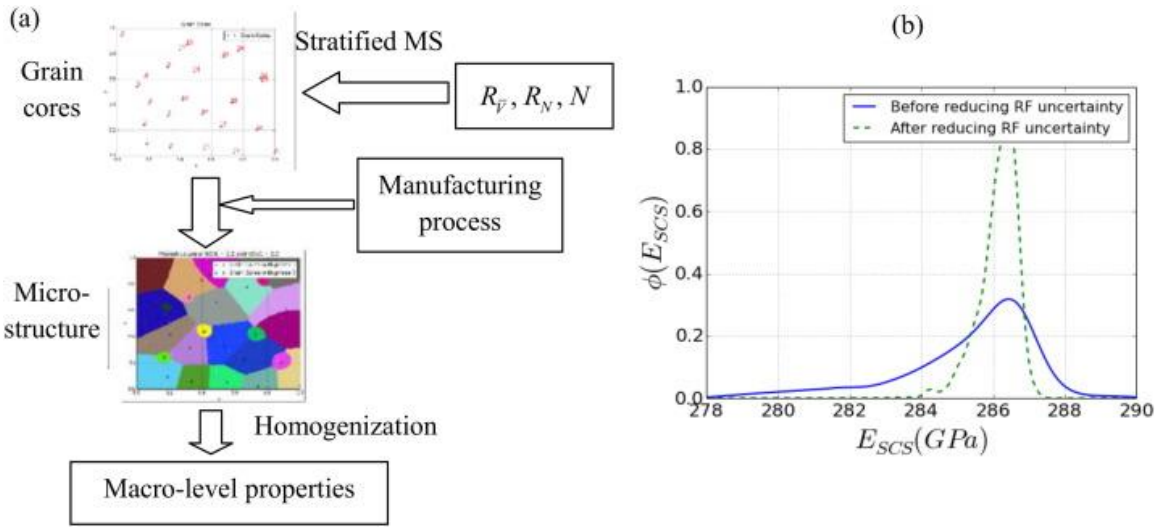

Figure 2.4. UQ of elastic modulus for two phase polycrystalline alloy resulting from uncertainty propagated from processing temperature represented as a random field [21].

The Monte Carlo (MC) method is commonly used to propagate uncertainty through computational simulations. PDFs are randomly sampled and the model is run for each of the sampled inputs to generate an output distribuiton [18]. The disadvantage of MC is that a large number of samples are required to accurately estimate the output statistics. Due to the large computational cost associated with high fidelity ICME simulations, surrogate modeling techniques are often used to propagate statistical uncertainty as a practical concession.

Surrogate modeling techniques employed for UQP consist primarily of GP regression models [6, 25-27] and stochastic expansion methods (e.g., polynomial chaos expansion (PCE), partial differential equations) [28-30]. Owen et. al. found little difference in the robustness of UQP between these two methodologies; however, GP regression

provides quantification of uncertainty introduced by the surrogate model [32], thus GP regression was in this work.

In this work, GP models can be thought of as a surrogate for the high fidelity CPFEM model that takes as inputs the microstructure statistics and, when adequately trained, renders accurate predictions of output quantities of interest. The inner workings of this surrogate model consist of a kernel object, or covariance function, that acts as a prior distribution, with hyperparameters that are optimized with training data [96].

In interval analysis, the UQ problem translates to determining bounds on the output interval given interval bounds on the inputs. Any output response that falls within the output interval is a possible output with no frequency information assigned to it [18]. This provides the limits of achievable outputs for given inputs, which can be used in an inverse problem to deduce the allowable input space that will keep the bounds of outputs within an acceptable range. Since epistemic uncertainty is generally reducable, the bounds of outputs for given inputs can be constrained at the cost of greater computational or experimental expense.

Lastly, as shown in Figure 2.5, use of Dakota [18] has demonstrated that mixed UQ approaches are best approached with nested models, with the aleatory UQ model being embedded as an iterative process within the epistemic uncertainty model. At the outer level, epistemic uncertainty is quantified using interval methods, while the inner level accounts for aleatory uncertainty. The outer level generates sets of realizations of the epistemic parameters, and each set of these epistemic parameters is used in a probabilistic analysis over the aleatory random variables.

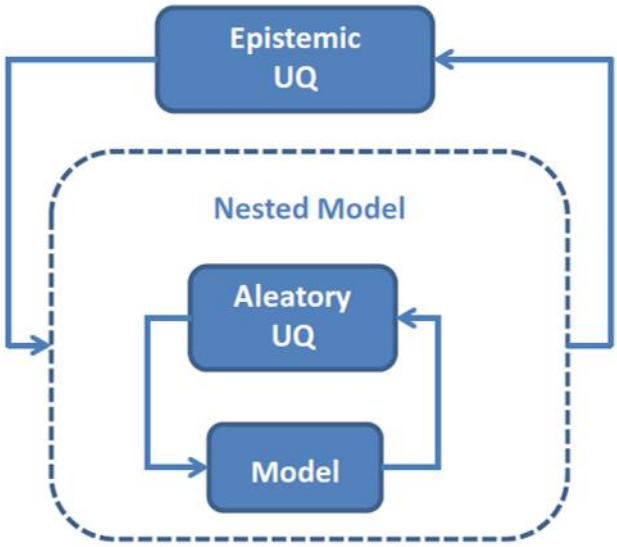

Figure 2.5. Dakota nested model approach for mixed UQ analysis (adapted from [18]).

2.6 Inductive Design Exploration Method

Historically, materials design and development has been approached with trial-and-error strategies along with empirical relationships and simple sequential design and deployment protocols. [2] This traditional framework employed limited iteration due to dependence on costly and time consuming physical experimentation. To improve this process Olson [55] proposed a methodology based on an inductive, goal/means (top-down) approach that employs selected use of models that pursue deductive, cause and effect (bottom-up) paths illustrated in Figure 2.6.

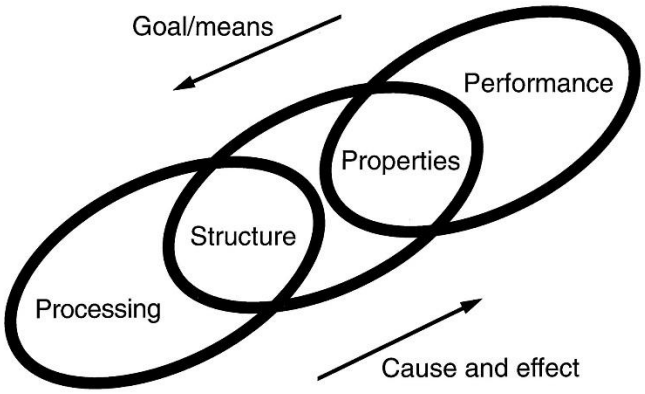

Figure 2.6. Olson's concept of materials by design [55].

The bottom-up path is important to facilitate understanding the physics associated with PSP linkages. However, the top-down approach is essential to design of materials for specific sets of performance requirements. The Inductive Design Exploration Method (IDEM) is a useful methodology that exploits Olson's concept by pursuing bottom-up mappings (either experimental or computational) to assess feasible or accessible structures and properties, followed by top-down searches to identify candidate solutions for multi-level robust design under uncertainty [97]. IDEM also allows for an application specific materials optimization strategy [50].

Achieving desired performance usually requires tradeoff between conflicting goals since there is generally no clear optimal solution when one considers the effects of aleatory and epistemic uncertainty. Therefore, a Pareto optimal solution is generally recommended when dealing with complex uncertain optimization problems [51].

There are three robust solution schemes that seek to optimize performance by minimizing variance of different elements of the solutions space: Type I robust solutions seek to minimize variation due to noise, type II robust solutions aim to minimize variation

due to control factors, and type III robust solutions aim to minimize variation due to uncertainty inherent in the model [51].

IDEM uses models or other functional relationships to link levels in design such as process to structure and structure to properties. Feasible inputs at one level are determined by sampling and propagating through linkages to see what values satisfy the response requirements of the next level. The points that do not meet the design criteria are labeled infeasible. The border between the feasible and infeasible values can be defined iteratively and this constitutes the feasible input space for design [50].

IDEM can be described in a two-step process. Step 1 is the deductive path where computational models, metamodels, or experiments are used for PS and SP mappings, establishing feasible regions of design space. A feasible region in process space is defined by the allowable ranges of process parameters (e.g. annealing time, annealing temperature, etc.) and the feasible region in structure space is established by propagating these parameters and their associated uncertainties to a multi-dimensional structure space made up of ranges of relevant microstructure parameters. Likewise, structure space and uncertainties are propagated to property space. Step 2 is the inductive path where feasible solutions are explored based on ranged sets of performance requirements that intersect with the bottom-up mappings. IDEM can determine feasible structure space and in turn the associated regions of process parameter space by propagating through these design levels [97].

IDEM is an attractive approach for robust design as it provides a computational workflow for generating robust design decision support in the face of uncertainty [48].

IDEM was implemented in an open source python computational environment called pyDEM [49].

PyDEM relies on functional relationships between levels in the inductive exploration of design space. In the current work, GP models were used as the functional relationships, to facilitate a more general approach to UQ in inductive design. Additionally, pyDEM allows for a rudimentary UQ process by which a standard error (e.g. +/- 2%) can be applied to input variables. In the current work, the aforementioned UQP protocols were applied to include state of the art UQ.

Chapter 3: Calibration, Sensitivity Analysis, and Weighted Sampling Based Uncertainty Quantification for a Microstructure Sensitive ICME workflow in Fatigue Critical Applications

3.1 Uncertainty Quantification in PSPP Framework

With the goal of exploring fatigue criticality of engineering alloys, decision-making can be better informed when uncertainty is measured and propagated through the various steps in the workflow. Robust design has gained widespread attention in ICME with applications in reliable decision making for complex engineering systems [47], seeking solutions that are relatively insensitive to small changes in uncertain quantities [98]. IDEM is an attractive approach for robust design as it provides a computational workflow for generating robust design decision support in the face of uncertainty [48]. However, the existing uncertainty quantification protocols included in the pyDEM computational environment [49] can be updated as desired to reflect various state-of-the-art UQ methodologies. Both the inherent, irreducible (i.e., aleatory) uncertainty in the system (quantified as statistical distributions) and uncertainty that can be reduced by increasing the knowledge of the system (i.e., epistemic) should be considered.

In order to conduct uncertainty quantification for a complicated system such as the material systems explored in this work, the system must be well understood, and to this end, process-structure-property-performance (PSPP) maps were constructed for two

material systems of interest; Ti64 and Al7075-T6. In addition to constructing PSPP maps, a global sensitivity analysis (GSA) was carried out to characterize the structure-property linkages. However, before a GSA could be conducted it was necessary to calibrate the computational models to ensure agreement between simulation results and experimental results. Finally, once the material systems were mapped and the models were calibrated and well understood via a GSA, a first pass at uncertainty propagation was demonstrated using an importance sampling technique to approximate the distribution of uncertainty in properties of interest in Ti64 based on distributions of uncertainty in input microstructure statistics of interest.

3.2 Fatigue PSPP Mapping

Traditional materials science and engineering practice has focused on reductionism, rather than a systems approach. With recent advances in computational tools, radical shifts can occur in the way material structure and properties are addressed in the design process. By considering how to tailor the material structure rather than selecting from a list of available materials, component level performance can be optimized and improved. One of the major impediments to this vision is the difficulty of communicating the complexities of structure of a hierarchical material system to engineers [4].

In design engineering, quality function deployment (QFD) tools are used to call attention to the customer needs. These QFD tools provide a structured approach to define customer requirements and translate them to engineers in the form of engineering attributes. A PSPP map is an analogous system design chart for materials design that helps

materials engineers easily identify important linkages [56]. PSPP maps provide key microstructural subsystems, primary links of these subsystems to properties they control, and the stages of processing that govern their dynamic evolution [57]. Figure 3.1 and Figure ***3.2*** show the PSPP maps for the two material systems under investigation in this work, Ti64 [52] and Al7075-T6 [57], respectively.

These two materials were chosen to demonstrate this the scientific framework establishing in this thesis because they are both commonly used and well characterized materials. Three properties were chosen to represent the performance requirements of interest: (i) yield strength (σ_y) (ii) elastic modulus (E), and (iii) minimum fatigue life. For a given microstructure, σ_y and E can be extracted from a macroscopic stress-strain curve based on information from the boundaries of a computational RVE in a CPFEM simulation. The RVE concept is less useful for fatigue crack formation due to its rare-event nature [93, 99]; a RVE would be untenably large for computation [100]. To quantify fatigue response, ensembles of statistical volume elements (SVEs) will be used to rank order microstructures based on extreme value distributions of Fatemi-Socie FIPs.

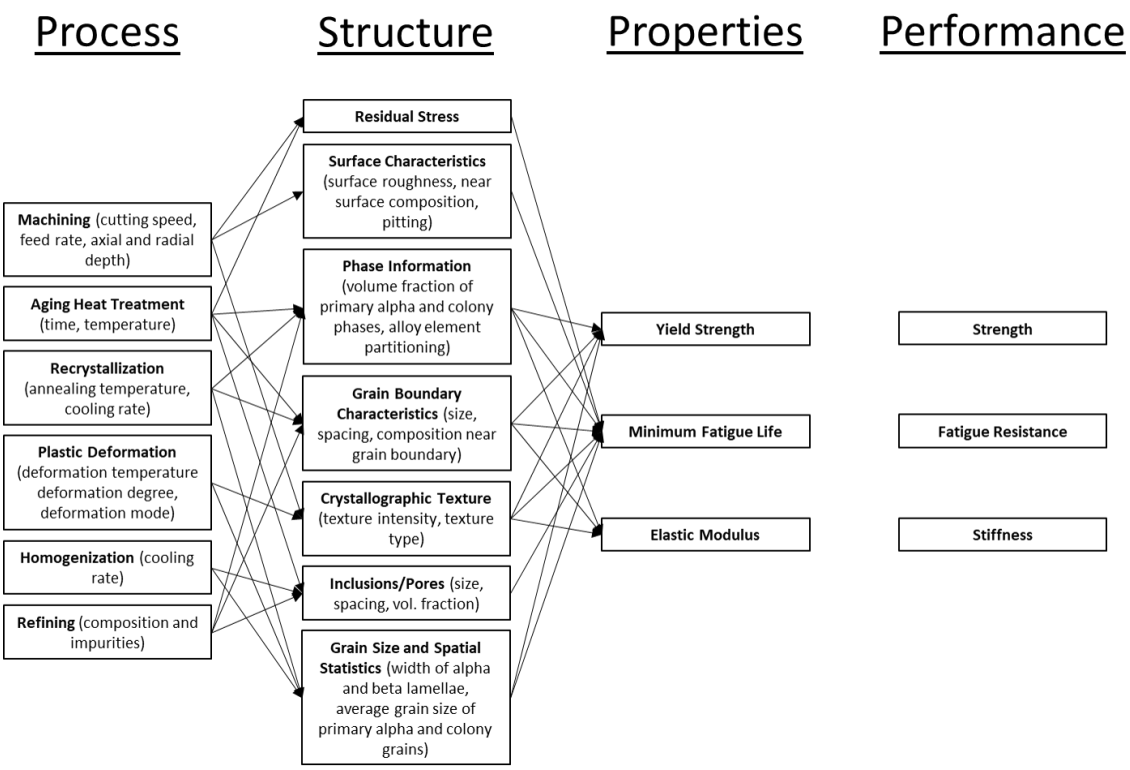

Figure 3.1. Ti64 process-structure-property-performance map (informed by [52]).

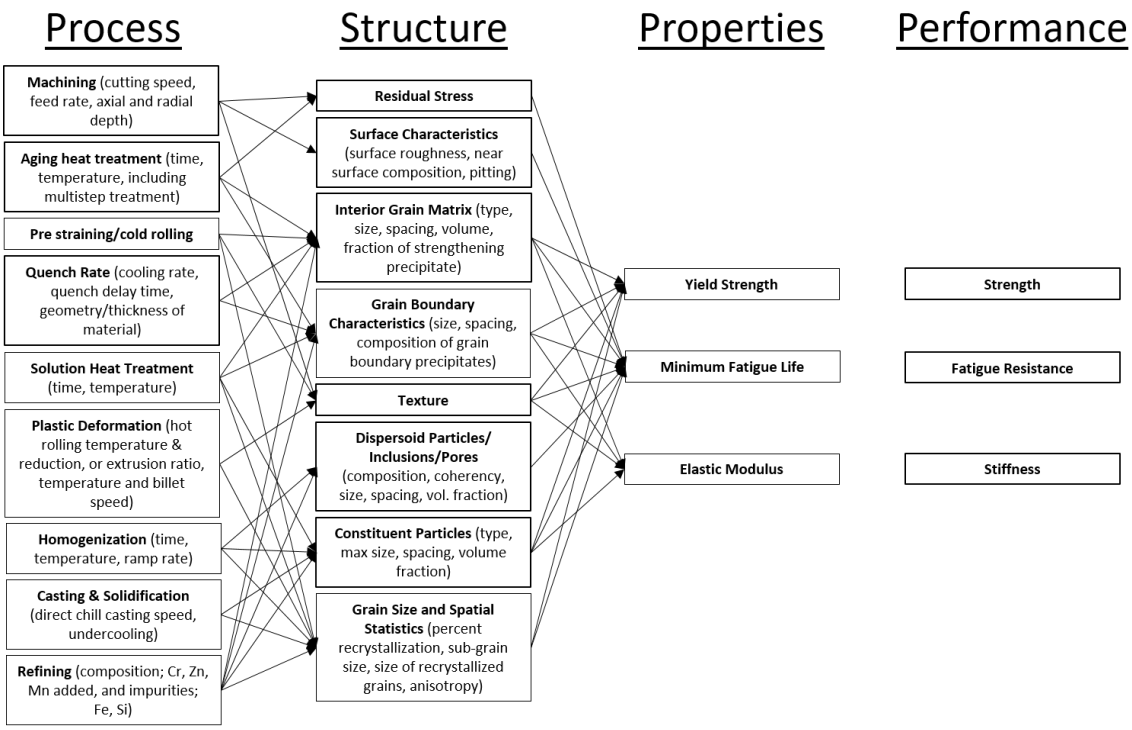

Figure 3.2. Al7075-T6 process-structure-property-performance map (adapted from [57]).

The PSPP maps shown in Figure 3.1 and Figure 3.2 show what are considered to be the relevant mesoscale microstructure attributes. However, for the sake of uncertainty quantification in this work, the microstructure attributes that were fully operable during the UQ process were limited to:

(i) Grain size and spatial statistics, for which the average grain size of primary alpha and colony grains were investigated.

(ii) Crystallographic texture, for which the intensity of four common textures in Ti64 (random, Beta-annealed, transverse, and basal-transverse) were investigated.

(iii) Interior grain matrix, for which the volume fraction of primary alpha phase was investigated.

3.3 Crystal Plasticity Finite Element Models for Ti64 and Al7075-T6

3.3.1 Ti64 Model

The microstructure-sensitive FEM model employs a multiplicative decomposition of the deformation gradient, a rate-sensitive power law flow rule for the slip system shearing rates and associated slip system hardening rules [101, 102]. The models were implemented as User MATerial (UMAT) subroutines in ABAQUS [103, 104]. The initial Ti64 crystal plasticity model was developed by Mayeur and McDowell [101] which considers the primary alpha phase separately from the alpha-beta colony phase by accounting for distinct three-dimensional slip geometry in each phase. Additionally, it accounts for dislocation structure and crystallographic texture. Zhang et al. [105] expanded the constitutive model to capture length scale effects associated with dislocation interactions between various microstructure features for both monotonic and cyclic loading. Smith et al. calibrated [91] elastic constants, CRSS values and other power law flow rule parameters. In this work the CPFEM model of Smith et. al. [91] was used with one modification; the drag stress was comprised of only the CRSS value and not the initial threshold stress.

The primary alpha phase in the CPFEM model includes 24 active slip systems: three basal $\langle 11\bar{2}0\rangle(0001)$, three prismatic $\langle 1120\rangle\{1010\}$, six < a > first-order pyramidal $\langle 11\bar{2}0\rangle\{10\bar{1}1\}$, and 12 < c + a > $\langle 11\bar{2}3\rangle\{10\bar{1}1\}$ second-order pyramidal. Alpha-beta colony phase grains consist of alternating laths of secondary alpha and beta phase, which due too computational constraints are homogenized in the model. Therefore, the colony phase grains contain 12 active slip system for each of the hcp and bcc crystal structures: three basal $\langle 11\bar{2}0\rangle(0001)$, three prismatic $\langle 1120\rangle\{1010\}$, six < a > first-order pyramidal $\langle 11\bar{2}0\rangle\{10\bar{1}1\}$, and 12 $\langle 111\rangle\{110\}$ bcc slip systems. The proper crystallographic orientation is maintained between the colony secondary alpha and beta phase with the BOR which is defined as $(0001)_\alpha // \{101\}_\beta$ and $\langle 11\bar{2}0\rangle_\alpha // \langle 111\rangle_\beta$. The critical resolved shear stress in the colony phase is strengthened by 25% relative that of the primary alpha for basal and prismatic slip systems. A Hall-Petch relation is applied to the threshold stress for slip in both the primary and secondary alpha phases. Slip transfer between grains is not explicitly considered, i.e., grain boundaries are treated as impenetrable surfaces that enforce compatibility between grains. The detailed constitutive model equations and parameter values are given in Appendix A.

3.3.2 Ti64 Model Calibration

Along the course of this work a calibration software was developed within the McDowell group and has been adapted for Ti64 to recalibrate the model after the addition of grain size effects.

An overview of the calibration procedure is given here. The software will be referred to as Autocal for the remainder of this report [106]. Autocal is a python package, which builds on other common scientific packages. The procedure implemented in Autocal for calibrating a model consists of three steps. (1) The user selects a set of calibration parameters and offers an estimate of their ranges. (2) Autocal studies the primary effects of each parameter and suggests revised parameter ranges by making comparisons to a target. (3) Autocal iteratively informs a Gaussian process model with the results of model runs across the revised parameter ranges until an acceptable calibration is reached.

Initially, the user selects parameters that they want to vary in order to calibrate the model, and ranges for these parameters. The user must also provide an input dataset to compare the model response with for calibration. The input dataset should consist of stress, strain, and time data. The time data is important because Autocal uses a time interpolation function to tag each point in the stress-strain response of the model with an associated time, and the comparison between model response and input data is compared at each time. Essentially, since these simulations are strain controlled with a constant strain rate, the "time tags" match up to strain values at which Autocal compares stresses. The parameters and ranges should be selected such that, at the low end of the range for each parameter, the stress-strain results of the model will under or overshoot the desired stress-strain results (based on the data that the input data) and on the high end of these ranges the model should do the opposite. Once the user selects calibration parameters and appropriate ranges for each parameter, a univariate sensitivity analysis is carried out as an initial test to consider linear effects of the parameters on the stress-strain response. Autocal optimizes the range for each parameter and iterates on this process as many times as the user chooses. This

initial linear effects model was built using statmodels and the optimization was performed using SciPy [107].

Once the calibration parameters and their respective ranges of interest have been optimized, a Gaussian process model is built using the Matérn kernel function and hyper-parameters are tuned to maximize the log-likelihood of the model. The hyper-parameter optimization is repeated with randomly chosen starting conditions for every iteration to avoid local maxima in the likelihood function. When the Gaussian process regression has completed, the user will have a series of sets of values for the calibration parameters and the associated sum squared error, measured at each time step, between the stress-strain response of the model for those parameters, and calibration data [32].

The model parameters were calibrated at a temperature of 300K using two different strain rates and strain amplitudes comparing to experimental data sets. The calibration was carried out using beta-annealed Ti64 having an average grain size of 169 μm with a standard deviation of 20 μm, defined in Dream.3D as the average chord length of an equiaxed grain. The simulations were carried out with ensembles of 10 cubic SVEs having side lengths of 0.95 mm, 15,625 voxels, and periodic boundary conditions. An example of the microstructure used for the simulations is shown in Figure 3.3 below.

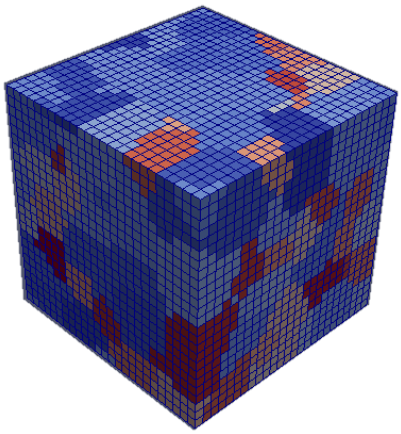

Figure 3.3. Statistical volume element used for constitutive model calibration.

The first simulation was carried out with a strain amplitude of 0.8%, strain rate of $0.001s^{-1}$, and with a fully reversed strain ratio of -1. The second simulation was carried out with a strain amplitude of 1.0%, strain rate of $0.0005s^{-1}$, and with a strain ratio of -1. The results of the calibration are shown in Figure 3.4 and Figure 3.5 below.

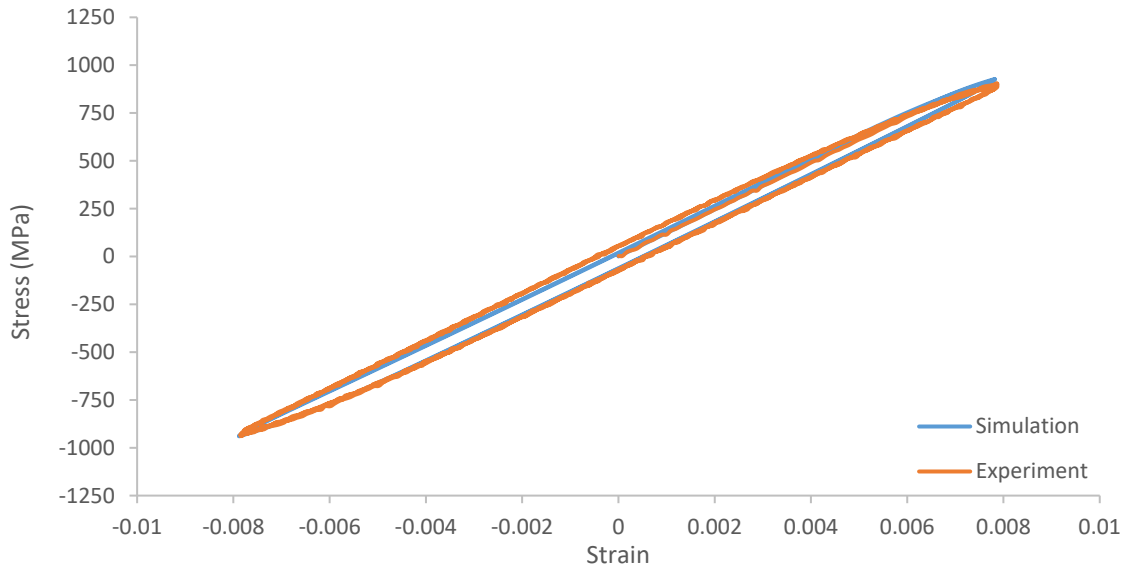

Figure 3.4. Calibrated results for the initial three cycles of loading of the Ti64 beta-annealed microstructure at room temperature with strain amplitude ε_a =0.8%, strain rate of 0.001s^{-1}.

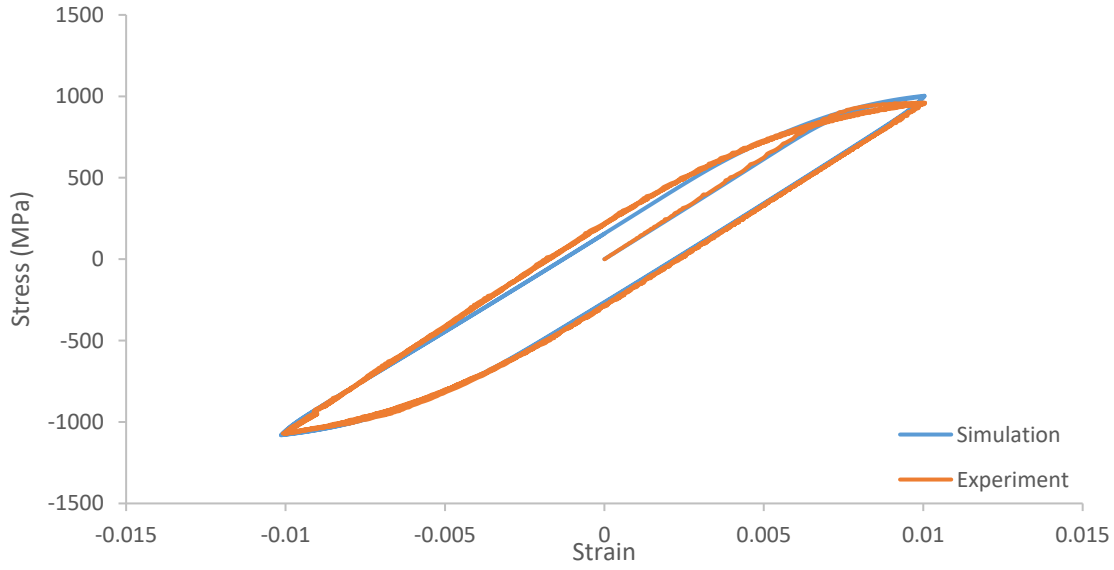

Figure 3.5. Calibrated results for the initial 3 cycles of loading of the Ti64 β-annealed microstructure at room temperature with fully reversed strain amplitude ε_a =1.0%, strain rate of 0.0005 s^{-1}.

Both curves fit the experimental data very well. The parameters that were allowed to vary for this calibration using the Autocal software were the critical resolved shear stresses in the basal, prismatic, and first and second pyramidal planes, as well as a threshold softening term, $(\kappa^{\alpha}_{s})_{t=0}$, which is a constant that, when added to the Hall-Petch strength term, defines the initial threshold stress, and α_{prism}, which acts as a unitless coefficient that adjusts the critically resolved shear stress for the prismatic plane under compression. The prior values of these parameters used in earlier iterations of the Ti64 model, which did not include grain size effects, as well as the newly calibrated values are shown in Table 3.1.

Table 3.1. Calibration parameters for the Ti64 model.

Parameter	Prior values	Calibrated
$\left(\tau_{cr}^{\alpha}\right)_{basal}$	350 MPa	339 MPa
$\left(\tau_{cr}^{\alpha}\right)_{prism}$	275 MPa	266 MPa
$\left(\tau_{cr}^{\alpha}\right)_{pyr\langle a\rangle}$	470 MPa	450 MPa
$\left(\tau_{cr}^{\alpha}\right)_{pyr\langle a+c\rangle}$	570 MPa	551 MPa
$(\kappa^{\alpha}_{s})_{t=0}$	50 MPa	42 MPa
α_{prism}	15	22

3.3.3 Al7075-T6 Model

The microstructure-sensitive FEM model employs a multiplicative decomposition of the deformation gradient, a rate-sensitive power law flow rule for the slip system shearing rates and associated slip system hardening rules [36]. The models were implemented as User MATerial (UMAT) subroutines in ABAQUS [103, 104]. Hennessey

[37] investigated three constitutive models for the mechanical modeling of Al7075-T6, specifically considering different back stress formulations for the crystal plasticity. The model considered slip system kinematic hardening with nonlinear dynamic recovery, which was essential to match experimentally measured plastic strain at low levels of applied stress. Experimental peak stress vs. plastic strain data was leveraged [108] to evaluate and initially calibrate the model. This model includes the twelve face-centered-cubic (FCC) slip systems made up of three slip directions on the four octahedral slip planes. Slip transfer between grains is not explicitly considered, i.e., grain boundaries are treated as impenetrable surfaces that enforce compatibility between grains. Both material model forms and parameters reflect a cyclically stable hysteresis response. The detailed constitutive model equations and parameter values are given in Appendix A.

3.3.4 Al7075-T6 Model Calibration

The calibration of the Al7075-T6 model performed by Hennessey [37] was verified as shown in Figure 3.6 and Figure 3.7 below. As seen in the figures, the current constitutive model agrees with experimental data for both fully reversed strain amplitudes of 1% and 1.8% [109]. As such there was no need for re-calibration, since there has not been any major changes to this constitutive model. Model parameters were calibrated to fully reversed cyclic stress–strain data at room temperature.

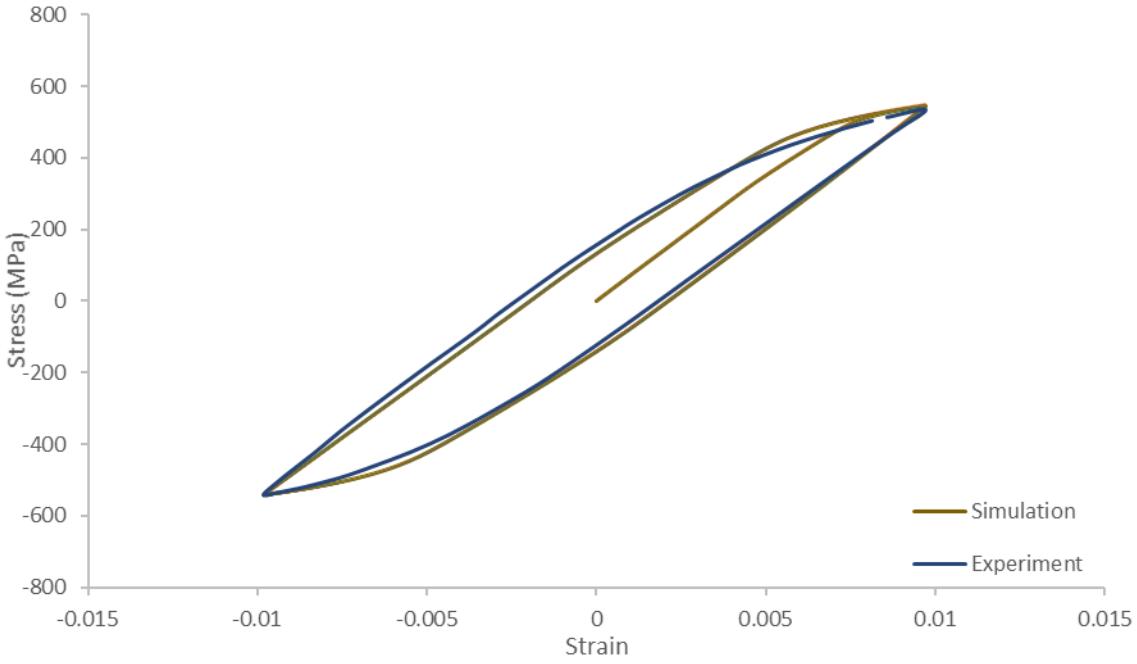

Figure 3.6. Al7075-T6 calibration verification with 1% strain amplitude.

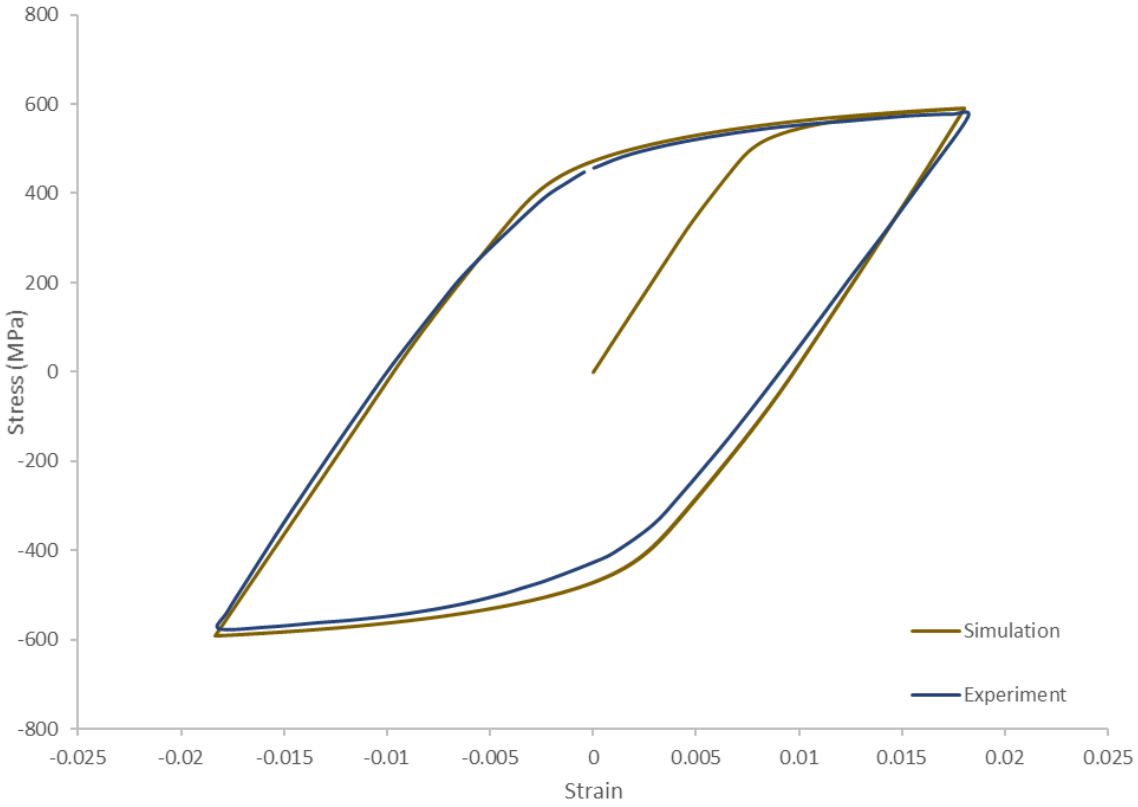

Figure 3.7. Al7075-T6 calibration verification with 1.8% strain amplitude.

3.4 Fatigue Indicator Parameters

As previously described in Section 3.3.1 the microstructure-sensitive FEM model employs a multiplicative decomposition of the deformation gradient, a rate-sensitive power law flow rule, and associated hardening rules. Individual slip system level dislocation behavior depending on the crystal structure of the alloy is determined by relating applied stress to strain rate. The models are implemented as UMAT subroutines in ABAQUS.

The use of FIPs as surrogate driving force measures for fatigue crack formation and microstructurally small transgranular growth has been well established [38, 70, 110]. Castelluccio and McDowell [69] demonstrated strong correlation between a FIP based on

Fatemi-Socie [43] and the ΔCTD for cracks along the interface of slip bands and matrix in single crystal or in homogeneous single crystals. McDowell and Berard [111] explored similar parameters for small fatigue crack growth based on analogy to the ΔJ-Integral of elastic-plastic fracture mechanics to identify the driving force. FIPs serve as a surrogate measure for the driving forces for fatigue crack formation and subsequent growth.

In recent years, correlations of various FIPs with high fidelity experimental studies for transgranular small fatigue crack formation and early growth within polycrystals have been explored [65, 67], including variants of the particular FIP considered here. Nicolas et al. [68] found that a variant of the Fatemi-Socie based FIP provided the sufficient information to support high confidence correlations, arguing on the basis of having introduced more variables than other candidate FIP measures considered; however, the preceding works on similarity of this FIP to mixed mode ΔJ [43] and the strong correlation with ΔCTD for small cracks at slip bands in single crystals [69] suggest connection of these forms to mixed mode driving force (sliding and opening) for small transgranular fatigue cracks. Additional FIPs have been introduced for fatigue crack formation driven by slip impingement on grain or phase boundaries [70, 71].

As the primary intent of the present work is to introduce a methodology for UQ for SP relations based on computed FIPs, we select the FIP based on the Fatemi-Socie parameter as the basis for its demonstration. The same methodology could be applied to other FIP definitions. This issue of FIP selection concerns model form uncertainty, which has received focus of prior studies exploring detailed experimental correlations (e.g., [67]).

FIPs are computed for each element in the discretized microstructures and volume averaged over a user-defined finite damage process zone. This alleviates mesh sensitivity

and regularizes the numerical solution, in addition to reflecting the physical damage process zone. The averaging volume is held fixed across different simulations to facilitate comparison of fatigue resistance. Castelluccio and McDowell [112, 113] introduced the concept of grain banding, in which the digital, discretized grains of SVEs are split into bands along crystallographic slip planes to be used to define domains for volume averaging. They concluded that the concept of band averaging should correlate well with polycrystals in which cracks nucleate and initially grow along crystallographic planes in the nucleant grain. The width of these bands is usually maintained at one or two element dimensions (fixed element/voxel size). This reduces the FIP averaging domain to regions within the grain, resulting in bands with a range of volumes. In this work, each grain is banded as proposed by Castelluccio and McDowell, but the bands are further divided into sub-band regions, as shown in Figure 3.8. Additionally, the first and last band of each grain is absorbed into the second and second-to-last band, respectively, to eliminate bands having too few elements. Each band is then analyzed so that unique combinations of eight elements which are closest to one another may be identified and designated as unique sub-band regions. Volume averaging then takes places over these sub-band regions, which provide a regularized averaging volume on the scale of the damage process zone.

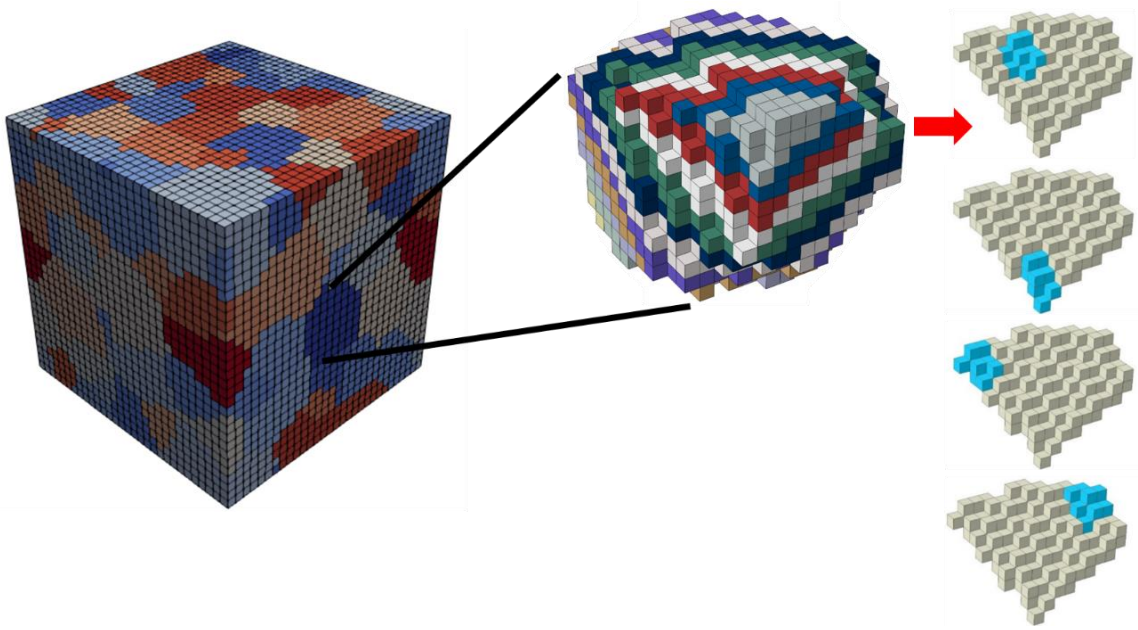

Figure 3.8. Ti64 statistical volume element (left) and a diagram of bands and sub band from one grain (right) [114].

The FIPs are calculated as a post processing operation. The stress and inelastic strain tensor for each element is reported during the maximum compressive to tensile segments of cyclic straining. Using the inelastic strain tensor, the eigenvalue problem is solved to find the maximum cyclic plastic shear strain range, on slip system α, given by $\Delta\gamma_p^{\alpha}$. The maximum stress normal to this plane is then computed as σ_n^{α} in a similar fashion. The FIP is calculated using Equation

(3.4.1), where σ_y is the macroscopic yield of the material and k is a constant which controls the influence of the normal stress; a value of $k = 1$ is assumed for this dissertation. This FIP is a slight variation of the Fatemi-Socie FIP focusing on particular slip systems and throughout the rest of this dissertation the FIP_{α} will be referred to simply as FIP.

$$FIP_{\alpha} = \frac{\Delta\gamma_p^{\alpha}}{2}\left[1 + k\frac{\sigma_n^{\alpha}}{\sigma_y}\right] \qquad \textbf{(3.4.1)}$$

3.5 Sensitivity Analysis

3.5.1 Ti64 Sensitivity Analysis

Uncertainty associated with the stochastic nature of microstructure attributes will be statistically quantified and propagated through the model. Uncertainty propagation through models usually takes the form $\mathbf{y} = \mathrm{f}(\mathbf{x}, \mathbf{d})$ where $\mathbf{x}$ is the vector of stochastic model inputs and $\mathbf{d}$ is the vector of deterministic inputs. As the number of stochastic model inputs considered in the uncertainty propagation process increases, the computational cost increases exponentially. A global sensitivity analysis (GSA) is used to study the relationship between uncertainty in the output $\mathbf{y}$ and in each of the stochastic model inputs $\mathbf{x}$. Results of the GSA are used to reduce the dimensionality of the problem by ranking each input. Inputs with negligible sensitivity can be held constant at their mean value [115].

There are a number of different advanced GSA methods existing in literature that provide different metrics for measuring the effects of each stochastic input variable [116]. Here, independent variables were varied within realistic bounds one at a time and dependent variables were co-varied when considered to be physically linked. This approach was taken to reduce computational cost compared with approaches such as a full Monte Carlo sampling to calculate the Sobol index [115] since first order relationships describe the sensitivity to microstructure attributes of interest well. For the initial

demonstration of the uncertainty quantification and propagation (UQP) framework in this work, the number of stochastic input variables is limited to those mentioned in Section 3.2.

Figure 3.9 shows the PSPP map for Ti64 highlighting the three microstructure attributes of interest for this sensitivity analysis. Two separate sensitivity analysis studies were conducted to investigate the macroscopic yield behavior (for σ_y and E) and the local FIP response, respectively. In both cases volume fraction of primary alpha phase was varied from 0 to 0.6 (baseline 0.3), average grain size was varied from 10 microns to 60 microns (baseline 30 microns), and texture was varied amongst four textures commonly seen in Ti64; random, beta-annealed, basal-transverse, and transverse (baseline random). The <0001> pole figures are shown in Figure 3.10. Uniaxial straining was in the x-direction, representative of the left-right directions on the pole figures.

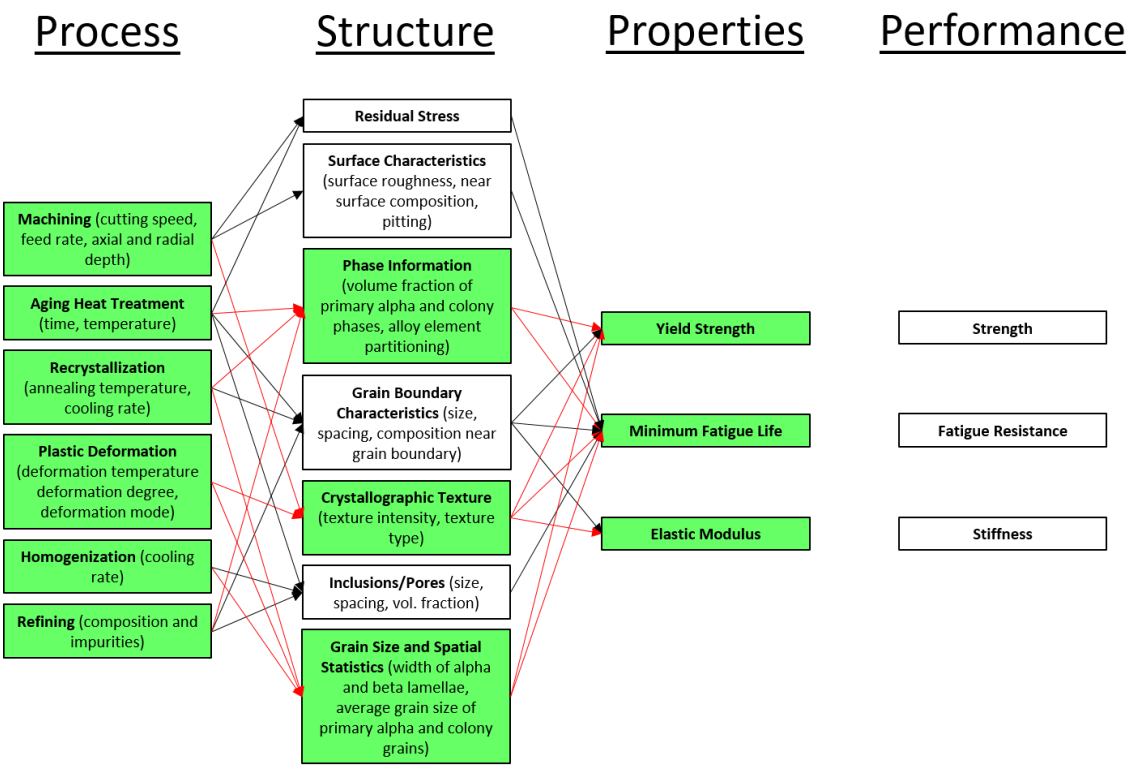

Figure 3.9. PSPP map for Ti64 sensitivity analysis.

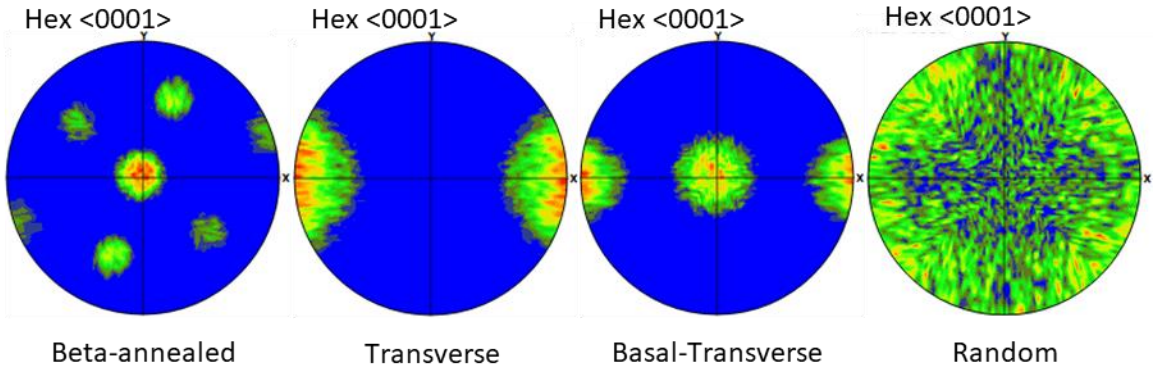

Figure 3.10. Pole figures of crystallographic textures used in Ti64 sensitivity analysis.

For the macroscopic yielding study, ensembles of five SVEs for each set of microstructure statistics were subjected to cyclic straining at 1% and macroscopic stress-strain curves were extracted based on information from the boundaries of each SVE and averaged over each ensemble. In the study of FIP response, ensembles of 30 SVEs were generated for each microstructure and CPFEM simulations were executed in which three fully reversed computational strain cycles with a strain amplitude of 0.6% were applied to achieve elastic-plastic shakedown. To properly represent statistic distributions of potential sites for fatigue crack formation, FIPs were computed at every element within the digital microstructures, after which volumetric averaging was performed. The 5 highest FIPs from distinct grains were extracted from each SVE. These were fit to Fréchet and Gumbel distributions so that trends of FIPs from SVE ensembles of different microstructures could be compared to one another. Additional test parameters for each sensitivity analysis are given in Table 3.2. Figure 3.11 and Figure 3.12 show the results of the yield strength and elastic stiffness sensitivity analysis and the FIP sensitivity analysis, respectively.

Table 3.2. Constant parameters for Ti64 sensitivity analysis.

Parameter	Stress-Strain	FS -FIPs
Strain amplitude	0.01	0.006
Strain rate	0.0005 s^{-1}	0.001 s^{-1}
# of applied cycles	2	3
Strain ratio	-1	-1
Temperature	300K	300K
Number of Grains	Approx. 300 per SVE	Approx. 100 per SVE
Elements	$(25 \text{ elements})^3$	$(30 \text{ elements})^3$
Ensemble size	5 SVEs	30 SVEs
Boundary conditions	Periodic	Periodic

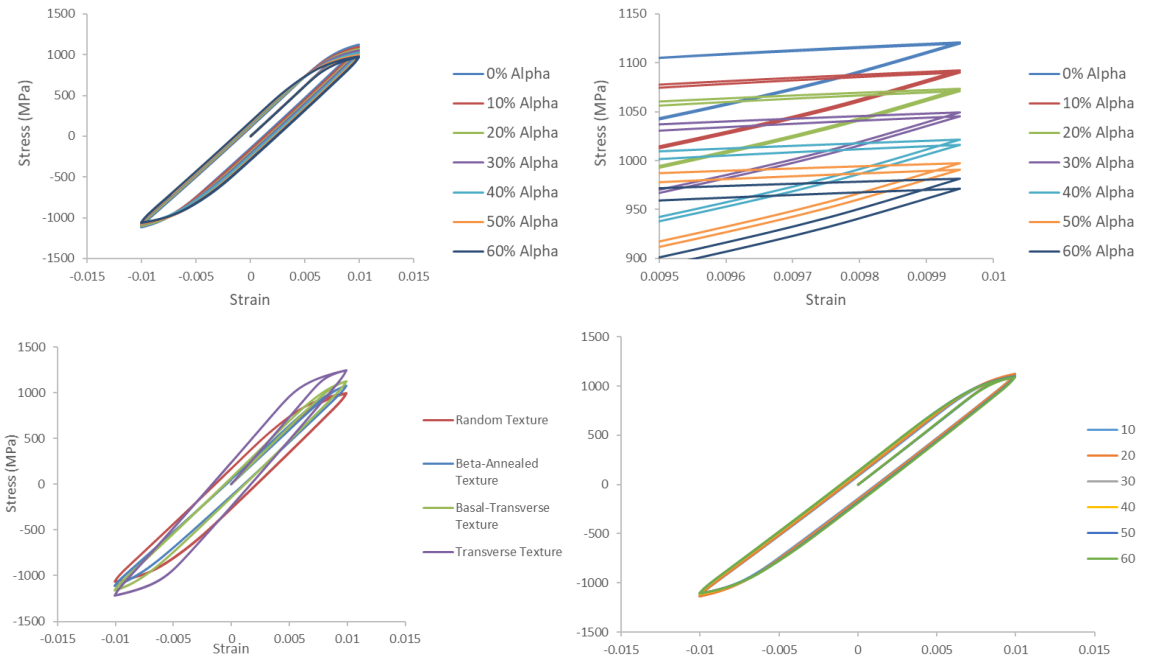

Figure 3.11. Macroscopic stress-strain response of Ti64 with varied microstructure attributes: Alpha phase volume fraction (top), texture (bottom left), average grain size (bottom right).

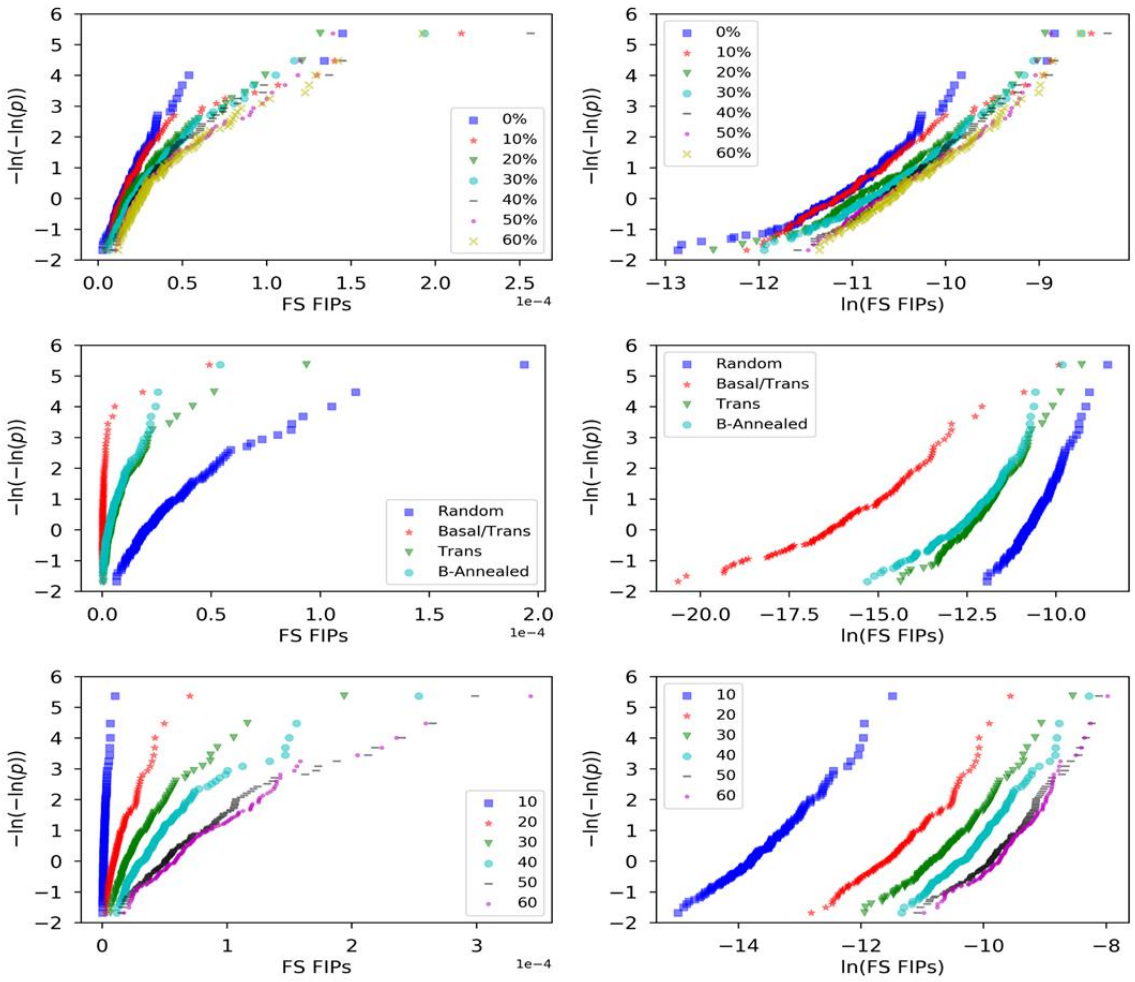

Figure 3.12. FIP response for Ti64 sensitivity analysis: primary alpha phase volume fraction (top), texture (middle), and average grain size (bottom) plotted to show fit to Gumbel (left) and Fréchet (right).

The σ_y and E sensitivity analyses showed that only texture affects elastic stiffness at the macroscopic scale, and that average grain size does not have a sufficiently influential effect on yield strength to warrant including it in the initial UQP process. Thus, the input space for microstructure attributes has been limited to primary alpha phase volume fraction and texture. The FIP sensitivity analysis results are shown in Figure 3.12, plotted to fit to

both Gumbel and Fréchet distributions. FIPs fit better to a Fréchet distribution in all cases. There are two quantities of interest to characterize a Fréchet distribution: slope and y-intercept. The primary alpha phase volume fraction and average grain size did not have significant effect on the slope, however they did affect the y-intercept. Texture affected both the slope and y-intercept. In the interest of characterize the top values in the extreme value FIP distributions both slope and intercept are relevant in calculating a predicted FIP response above some user defined threshold, e.g. predicted 99^{th} percentile extreme value FIPs (FIP_{99}).

3.5.2 Al7075-T6 Sensitivity Analysis

A sensitivity analysis for the Al7075-T6 material system was conducted to investigate the sensitivity of yield strength and elastic stiffness to microstructure attributes of interest. The homogenized stress-strain response of the simulated model was used to determine yield strength and elastic stiffness.

This sensitivity analysis was conducted to determine the high impact microstructure attributes for the Al7075-T6 material system in terms of fatigue properties, and to identify the optimal ranges of these attributes that will be needed to conduct a comprehensive uncertainty quantification. It is of interest to quantify the uncertainty of fatigue properties introduced by the typical variance in microstructure attributes resulting from the processing steps taken for the materials of interest. As such, the sensitivity analysis has been explicitly broken down into process-structure-property linkages of interest as highlighted in PSPP map in this section.

The sensitivity analysis was focused on the effects of two microstructure attributes best accounted for by the CPFEM model: grain aspect ratio (i.e. effects of rolling), and texture. For this macroscopic yielding study, ensembles of five SVEs for each set of microstructure statistics were subjected to cyclic straining at 1% and macroscopic stress-strain curves were extracted based on information from the boundaries of each SVE and averaged over each ensemble. Additional test parameters for each sensitivity analysis are given in Table 3.3.

Table 3.3. Constant parameters for Al7075-T6 sensitivity analysis.

Parameter	**Value**
Strain amplitude	0.01
Strain rate	$0.0005s^{-1}$
# of applied cycles	3
Strain ratio	-1
Temperature	300K
Grain size (log normal)	$14\mu m \pm 3.5\mu m$
SVE dimensions	$(0.100mm)^3$
Number of Grains	Approx. 300 per SVE
Elements	$(40 \text{ elements})^3$
Ensemble size	5 SVEs
SVE boundaries	Periodic

Initially, considering the grain aspect ratio in rolled Al7075-T6, Figure 3.13 shows the paths in the PSPP map that are being investigated. Three different grain dimensional ratios were tested using the same SVE sizes to study the effect of grain boundary interactions on elastic stiffness and yield strength of Al7075-T6. Simulations were carried out with a random texture. Three different aspect ratios were tested as outlined in Table

3.4, and the aspect ratios describe the dimensional ratios of the grains in the rolling direction, transverse direction, and normal direction, with "1" corresponding to the smallest dimension. Average grain volume is kept constant.

Table 3.4. Relative dimensions for rolled Al7075-T6.

Test case	Rolling direction	Transverse direction	Normal direction
1	1	1	1
2	4	2	1
3	7	1	1

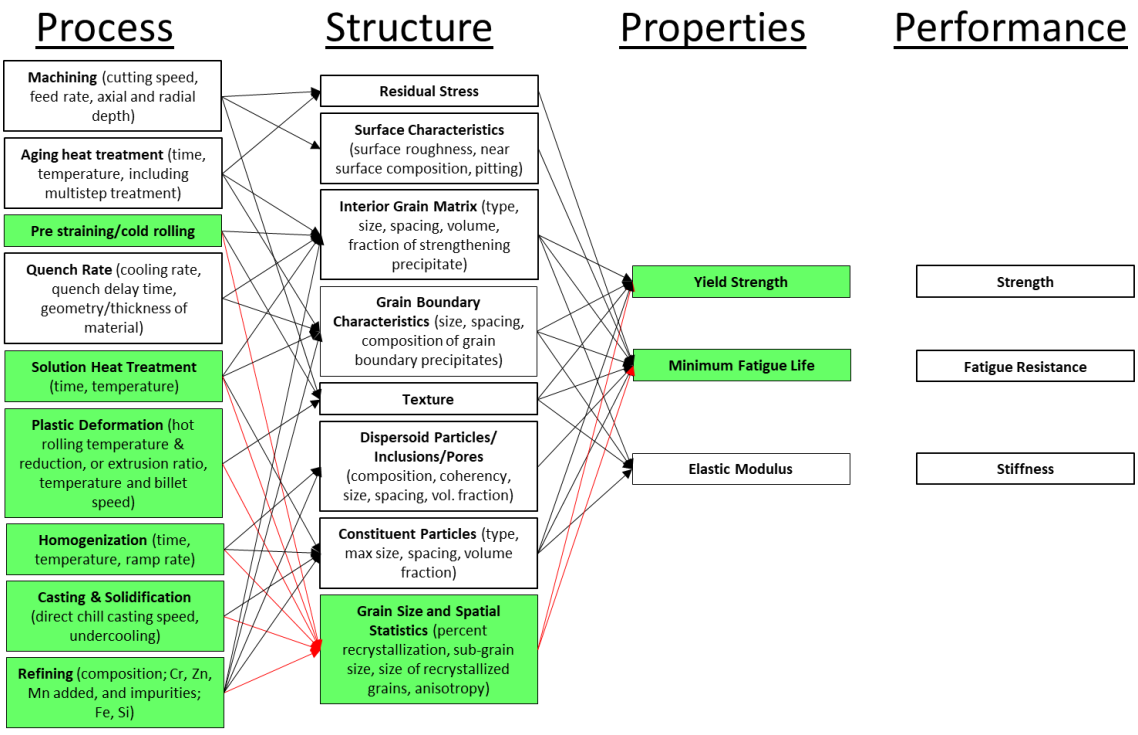

Figure 3.13. Grain size PSPP path for Al7075-T6 material system sensitivity analysis.

Simulations were carried out with equiaxed grains as a baseline case, rolled grains having a 4:2:1 ratio in the rolling, transverse, and normal directions respectively, based on the work of Turkmen [117], and rolled grains having a 7:1:1 ratio in the rolling, transverse, and normal directions (RD:TD:ND) respectively, based on the work of Zhao and Jiang [118]. Figure 3.14 below show sample SVEs for all three cases.

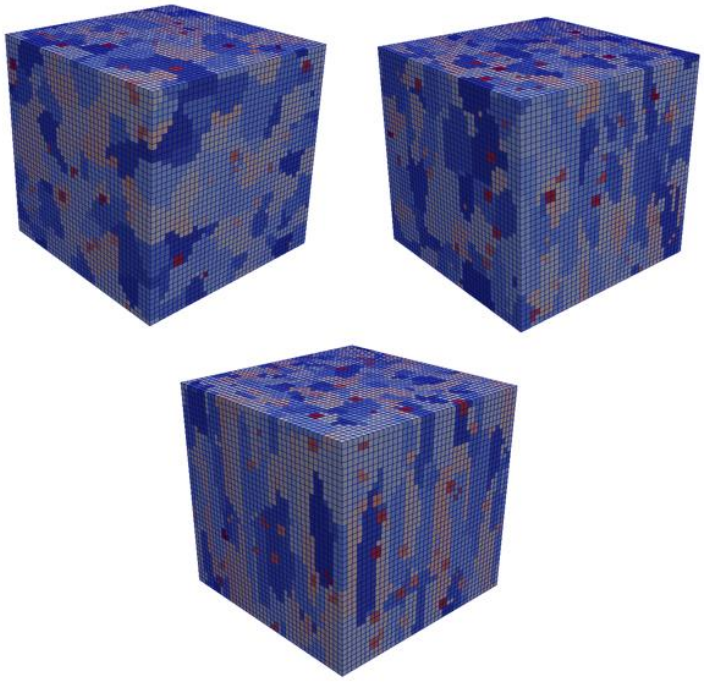

Figure 3.14. Sample SVEs for (top left) equiaxed, (top right) 4:2:1 rolled, and (bottom) 7:1:1 grains.

As outlined in Figure 3.13 the output properties of interest are modulus of elasticity, yield strength, and minimum fatigue life. Here we are just looking at elastic stiffness and yield strength in the loading direction. To quantify these, homogenized stress-strain curves

were plotted from each test case. Figure 3.15 shows the full homogenized stress-strain response, showing no sensitivity to grain aspect ratio in randomly textured grains.

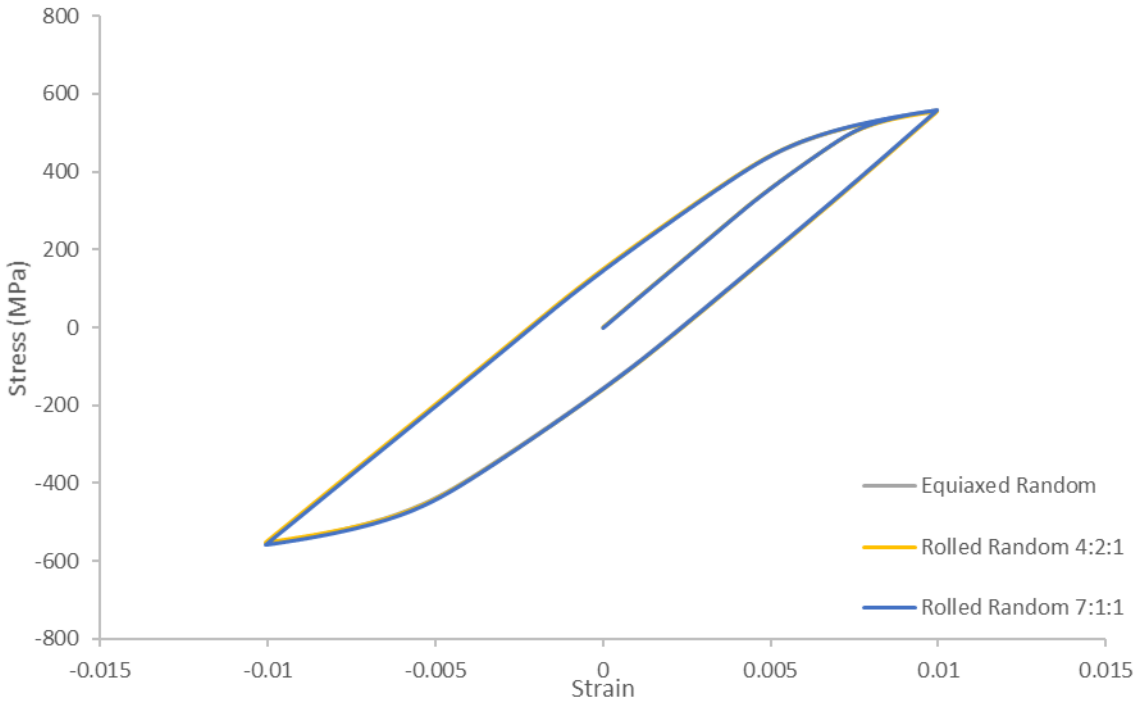

Figure 3.15. Homogenized stress-strain curves for Al7075-T6 with varying grain aspect ratios and random texture.

Next, the sensitivity of mechanical properties of Al7075-T6 to texture were analyzed in a similar fashion. Figure 3.16 outlines the PSPP path for this sensitivity analysis. Eighteen different textures were tested based on a literature review of common textures observed in rolled Al7075-T6 given the processing route of interest, and the effects on fatigue properties were analyzed. Five SVEs were instantiated for each unique set of microstructure statistics, and three fully reserved computational strain cycles were applied.

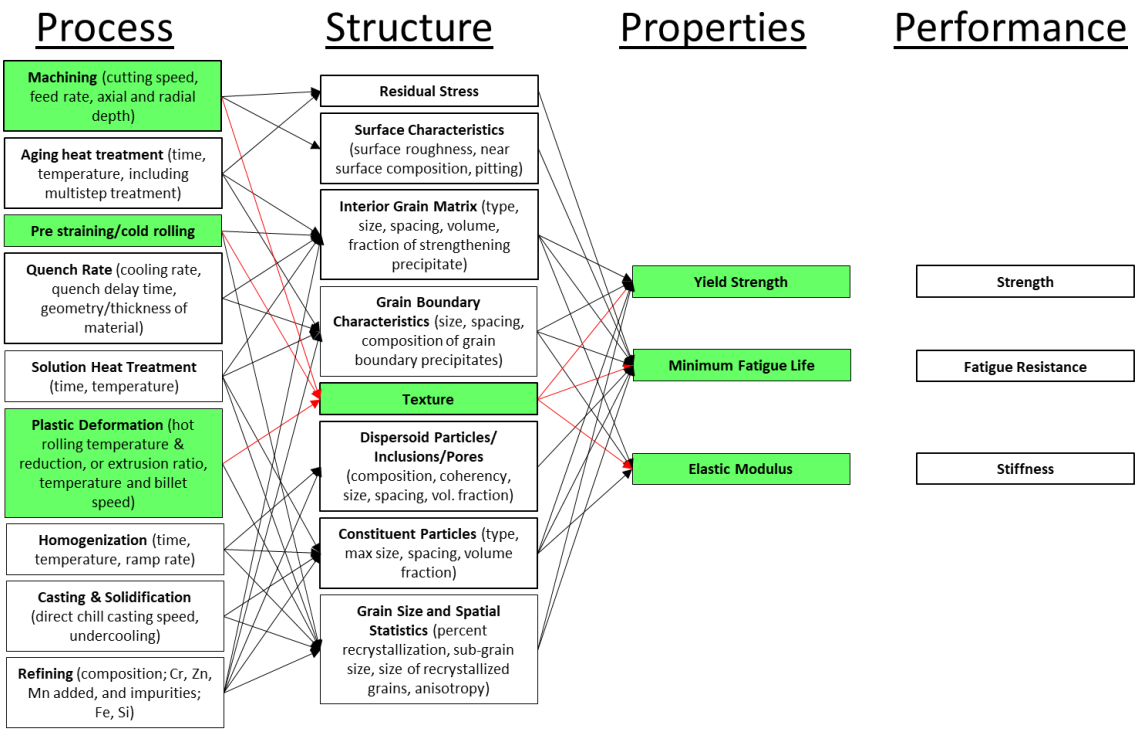

Figure 3.16. Texture PSPP path for Al7075-T6 material system sensitivity analysis.

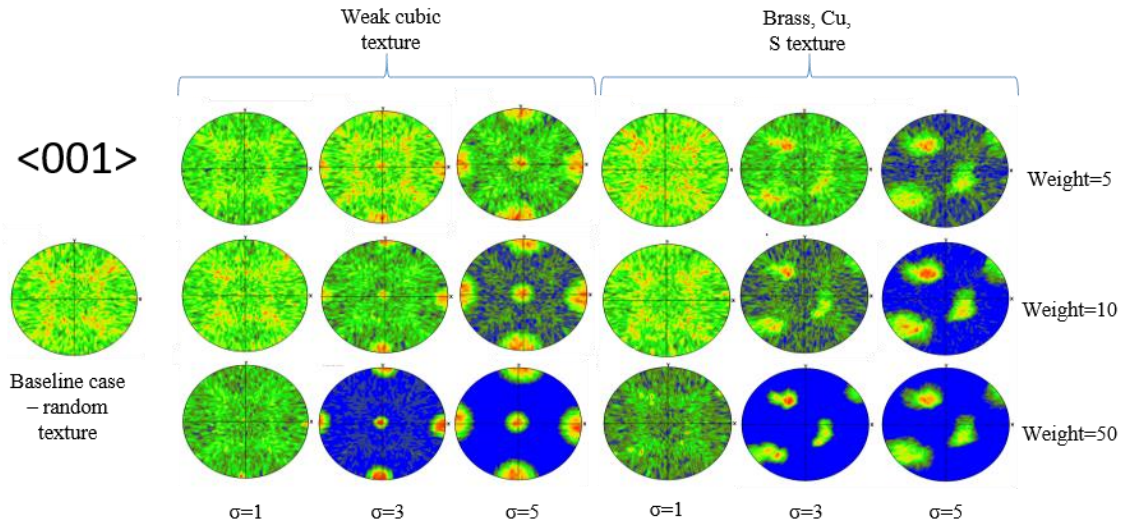

Figure 3.17. ODFs for various textures studied in Al7075-T6 material system.

Simulations were carried out with randomly textured grains as a baseline case, as well as various degrees of cubic texture based on the work of Turkmen [117] and various degrees of combined Brass, Cu, and S (BCS) textures based on the work of Cepeda-Jimenez [119]. Figure 3.17 shows the 19 <001> pole figures of textured microstructures. Figure 3.18 shows a sample SVE for simulation case 1, and Table 3.5 describes the textures for all 19 simulations.

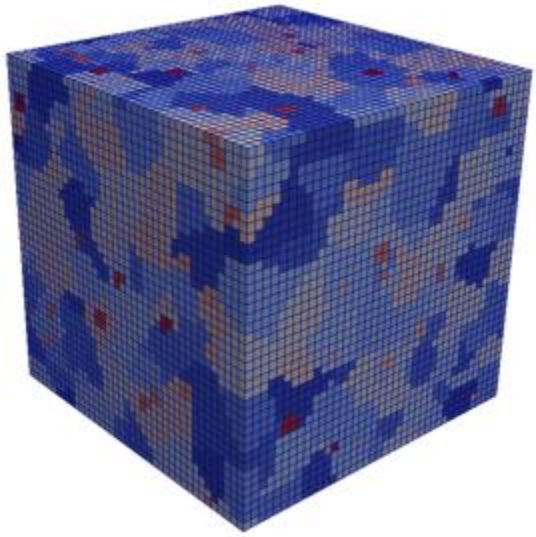

Figure 3.18. Sample SVE for grain size sensitivity analysis, case 1.

Table 3.5. Texture sensitivity analysis parameters for Al7075-T6.

TEST#	TEXTURE	WEIGHTING	SIGMA
1	Random	0	0
2,3,4	Cubic	5	1,3,5
5,6,7	Cubic	10	1,3,5
8,9,10	Cubic	50	1,3,5
11,12,13	Brass, Cu, S	5	1,3,5
14,15,16	Brass, Cu, S	10	1,3,5
17,18,19	Brass, Cu, S	50	1,3,5

Here, the quantities of interest are the elastic stiffness and yield strength in the loading direction. To quantify these; a homogenized stress-strain curve was plotted from each test case. Figure 3.19 and Figure 3.20 show the homogenized stress-strain curves demonstrating the effect of increasing the intensity of cubic texture and Brass, Copper, Sulfur (BCS) texture, respectively from random texture to highly textured.

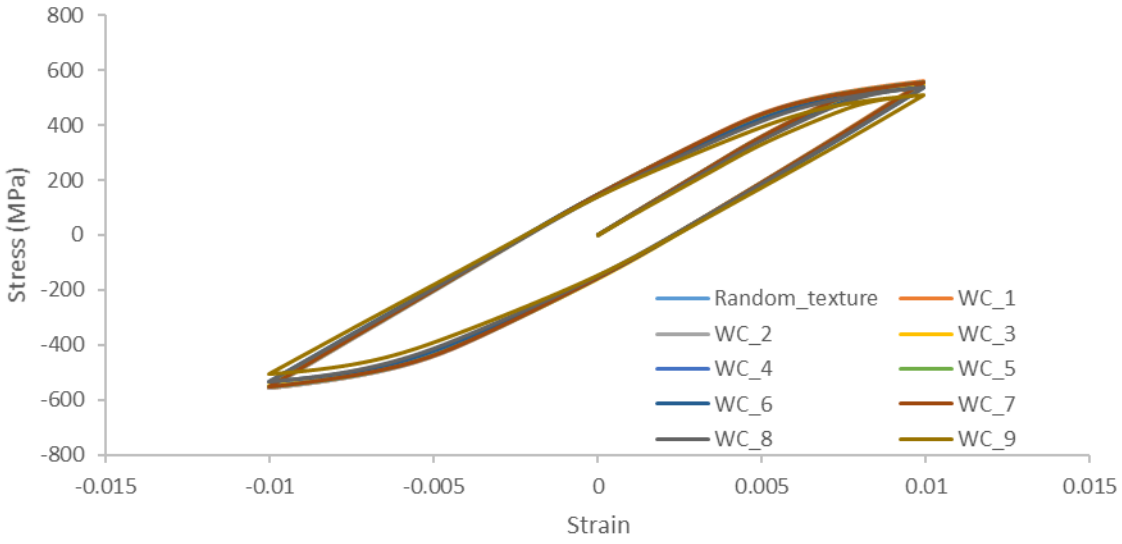

Figure 3.19. Homogenized stress-strain curves for varying intensity of Cubic texture.

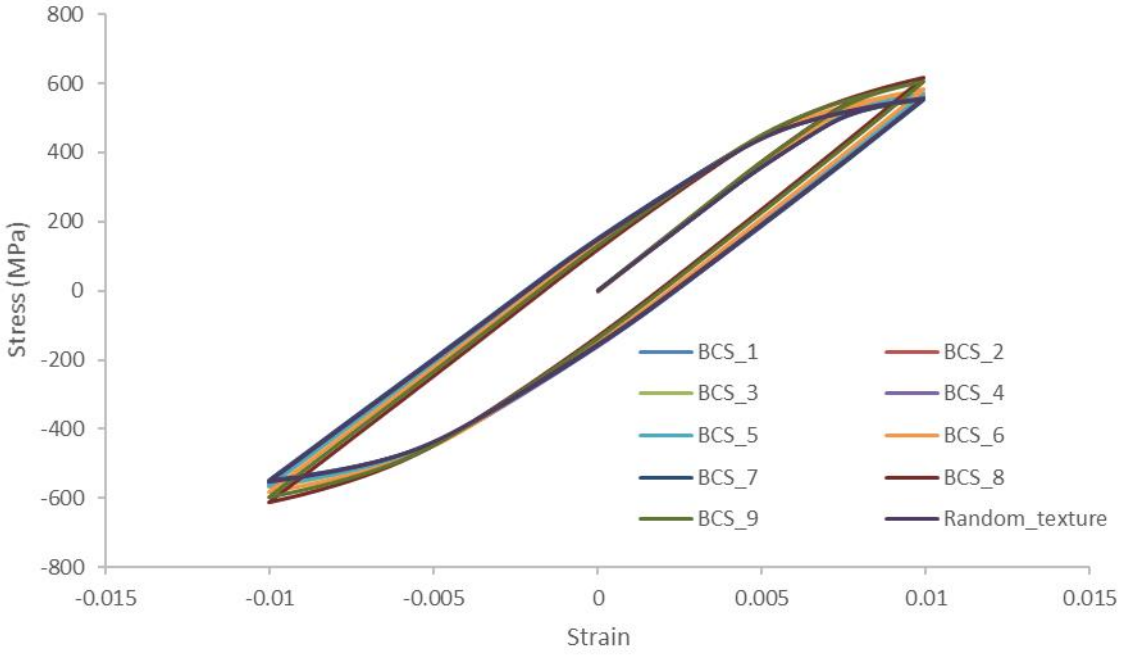

Figure 3.20. Homogenized stress-strain curves for varying intensity of BCS texture.

Increasing the intensity of cubic texture decreases the elastic stiffness and yield strength while increasing the intensity of BCS texture increases elastic stiffness and yield strength. However, it appears that in the case of BCS the greatest increase in yield strength and stiffness actually occurs in BCS_8, whereas the most pronounced effect of cubic texture occurred in WC_9. The reasoning for this is that sigma is the value that controls the spread of a given texture, by setting the number of bins in orientation space that it takes until the multiple random distribution value (the input for "weight") reduces to 0. As such it makes sense that generally as sigma increases, the texture smears making it less intense. However, in the case of weak cubic texture (i.e. WC_7 and WC_8), the remaining orientations in the microstructure tend to take over when sigma is low, thus we see a reduced effect of cubic texture and increased effect of random texture.

Conversely, in microstructures having BCS texture almost all of the crystallographic orientations are already dominated by brass, copper, or sulfur orientations, even at slightly lower weighting (i.e. BCS_8) since there are three coinciding texture profiles instead of just one in the case of the cubic texture. As a result of this, the most intense BCS texture occurs at BCS_8, which can be observed with visual inspection of Figure 3.17 as well as the result seen in Figure 3.20. This sensitivity analysis demonstrates that it is important to consider texture when investigating uncertainty in the properties of interest for Al7075-T6.

Next, the combined effects of texture and rolling were considered. To test this the most intense textures from each were applied to equiaxed, rolled 4:2:1, and rolled 7:1:1 microstructures. Figure 3.21 and Figure 3.22 show the results for rolled 4:2:1 and rolled 7:1:1 respectively. Random texture was shown earlier in Figure 3.15. Similar to the

randomly textured microstructure results for rolling, the yield strength and elastic stiffness were not sensitive to rolling in the textured microstructures, thus grain size and spatial statistics can be eliminated as a source of uncertainty propagation for yield strength and elastic stiffness with this CPFEM model going forward with the Al7075-T6 material system.

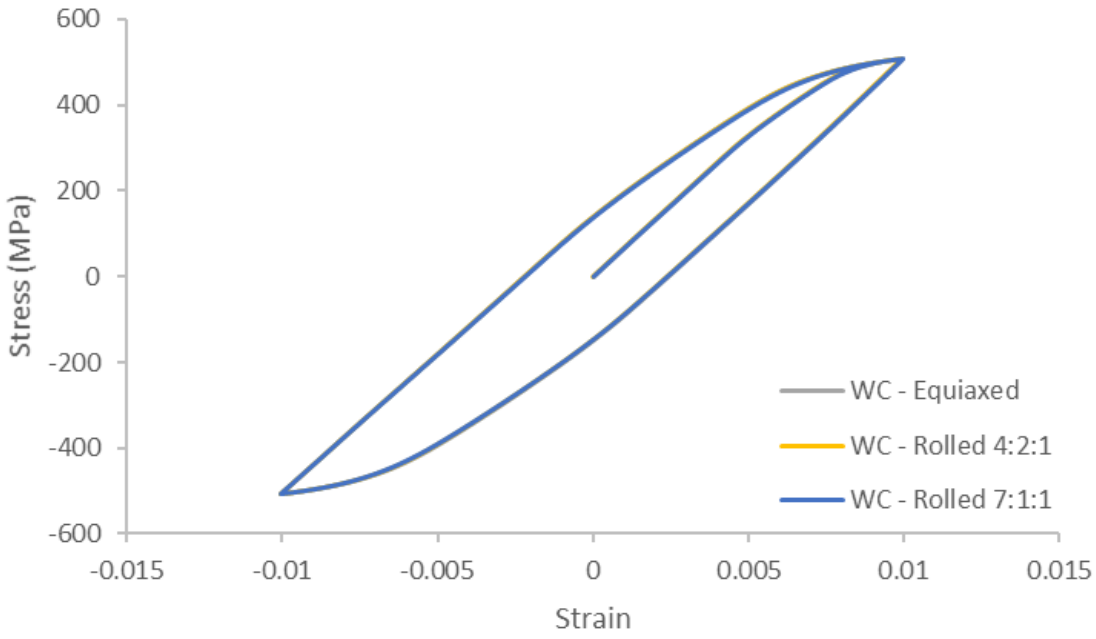

Figure 3.21. Homogenized stress-strain curves for cubic textured Al7075-T6 with varying grain aspect ratios.

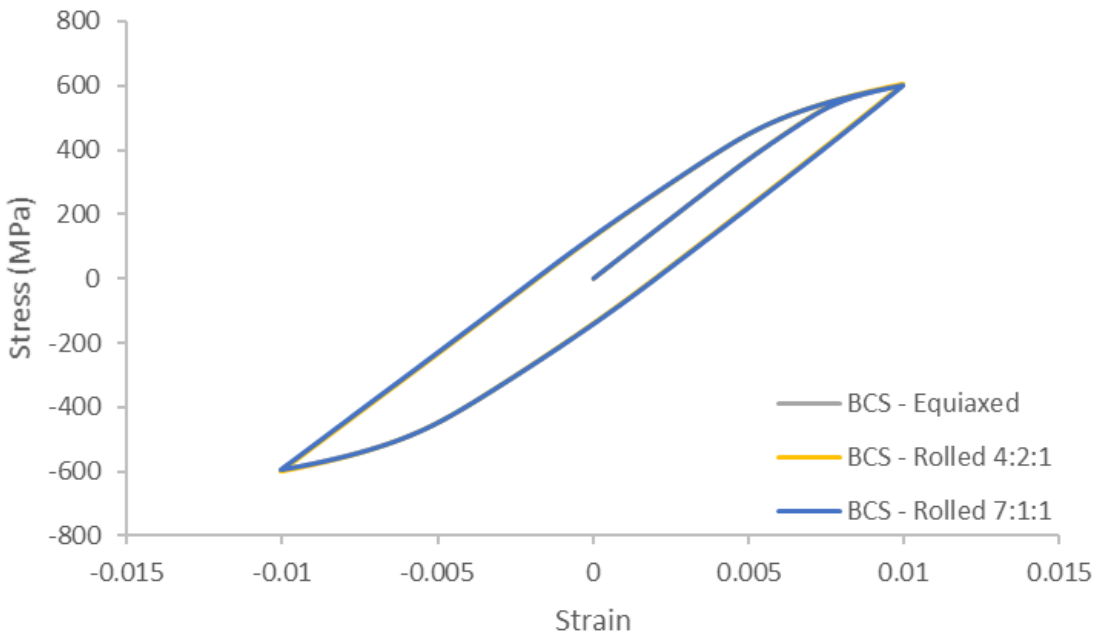

Figure 3.22. Homogenized stress-strain curves for BCS textured Al7075-T6 with varying grain aspect ratios.

3.6 Weighted Sampling Based Uncertainty Quantification

To demonstrate the effect of MSU on the QoIs in Ti64, nominal feasible values were assigned to the volume fraction of primary alpha phase (0.3), average grain size (30 μm), and crystallographic texture (basal-transverse) as the microstructure attributes of interest. The uncertainty in each microstructure attribute was estimated by examining existing literature for ranges of realized microstructure statistics for given nominal microstructures, and then Gaussian distributions were assigned to each, with average values assigned to desired nominal values. Figure 3.23 shows the PDFs for average grain size (top left) [120] and volume fraction of primary alpha phase (top right) [121], as well as the <0001> pole figures for the nominal basal-transverse texture with one standard

deviation variation in intensity [122]. The CPFEM simulations conducted to propagate uncertainty in the microstructure statistics to the FIP_{FS} response contained 20 SVEs and were cycled to a peak strain of 0.6 % at a strain ratio (min/max) of -1 and a strain rate of 0.001 s^{-1}. Three uniaxial, fully reversed cycles were applied in x-direction with periodic boundary conditions. A lognormal grain size distribution of 30 μm ± 7.5 μm resulted in approximately 100 grains per SVE.

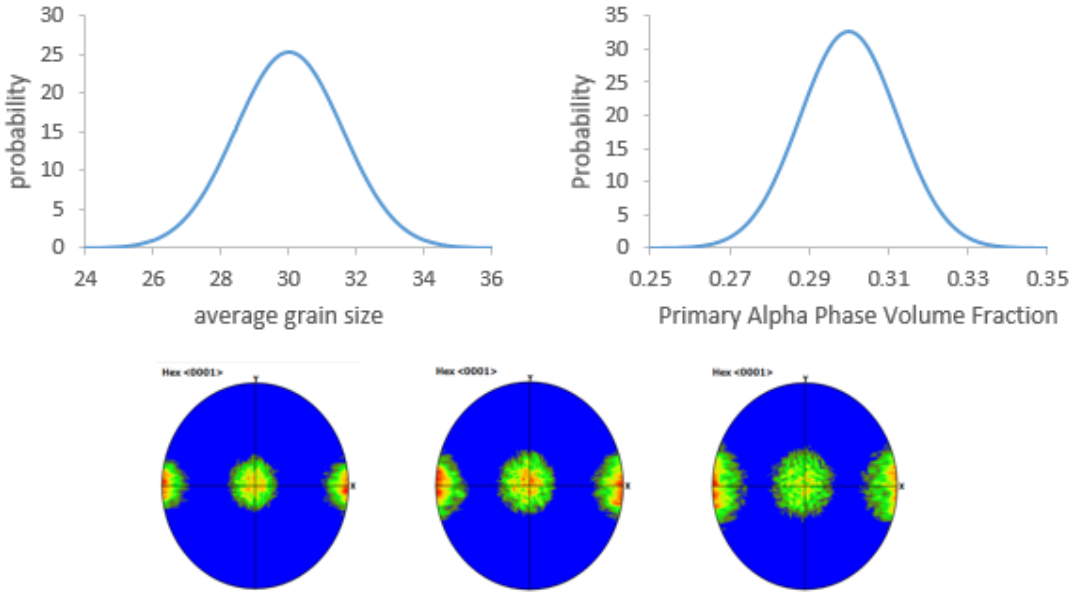

Figure 3.23. Statistical distributions of microstructure attributes for Ti64 with nominal grain size of 30 μm (top left), volume fraction of primary alpha phase of 0.30 (top right), and basal-transverse texture with varied intensity (bottom).

To reduce the computational time required to propagate the full input distribution through the CPFEM model to characterize an output distribution of extreme value FIPS, a weighted sampling technique was employed. Samples were drawn from a factorial of all

combinations of the mean value and the mean ± 1 and ± 2 standard deviations for average grain size and volume fraction of primary alpha phase as well as the mean value for texture and the mean ± 1 standard deviation (i.e. five values for average grain size, five values for volume fraction of primary alpha phase, and three values for texture, resulting in 75 total samples for the full factorial). Each of these 75 samples carried a probability from the combined three dimensional probability density function for the input space and this input probability was carried through to the output extreme value FIPs. The results are shown in Figure 3.24 and Figure 3.25.

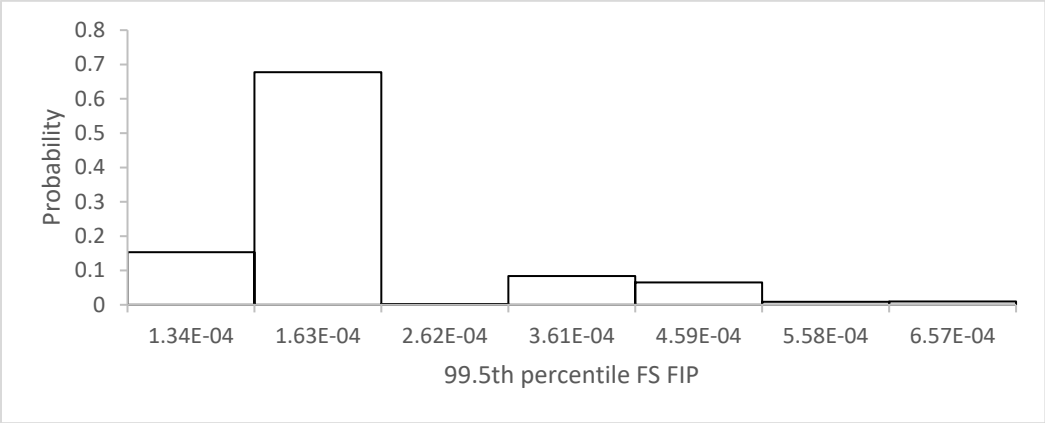

Figure 3.24. Output histograms of 99.5th percentile FS FIPs for Ti64.

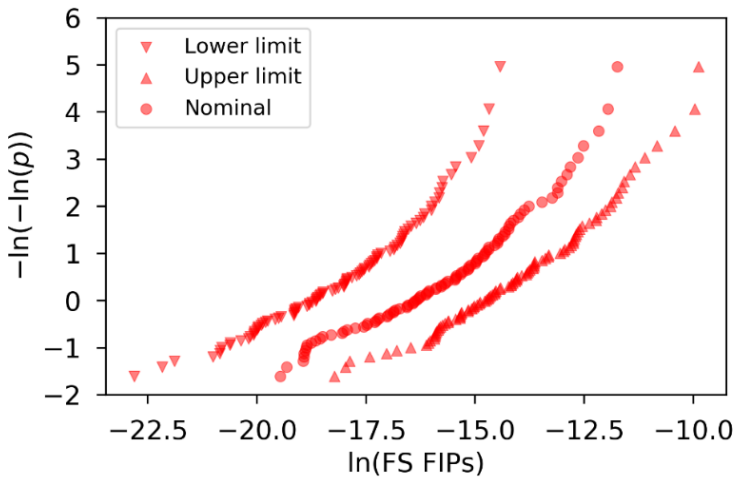

Figure 3.25. FIP_{FS} response for nominal Ti64 microstructure and the upper and lower limits of 99.5th percentile FIP_{FS} values plotted on a Fréchet distribution.

Figure 3.24 shows the histogram of the resulting distribution of predicted 99.5th percentile extreme value FIPs for this microstructure amongst the full ensemble of SVEs. Figure 3.25 shows the nominal FIP plotted using coordinates corresponding to a Fréchet distribution, as well as the maximum and minimum FIP response occurring within two standard deviations of the nominal microstructure statistics. The "lower limit" corresponds to the FIP response from the sample microstructure dataset that had the lowest 99.5th percentile FIP. This occurred when primary alpha phase volume fraction, average grain size, and texture intensity are two, two, and one standard deviations below average, respectively. The probability of a microstructure occurring with these statistics is approximately 0.01 %. Similarly, the "upper limit" is the FIP response from the sample microstructures having two, two, and one standard deviation above average.

These results demonstrate that the uncertainty in considering just these three microstructure attributes has a significant impact on the predicted FIP response, with a

range in FIP values of approximately half an order of magnitude for the same nominal microstructure. Additionally, the shape of the histogram demonstrates that the resulting uncertainty can have a non-trivial distribution that would be difficult to predict without propagating uncertainty through the CPFEM model or an adequate surrogate model. Due to the significant computational cost of these simulations, the surrogate modeling approach would be necessary to explore the design space.

The relative sensitivity was much lower for primary alpha phase volume fraction and average grain size compared with texture. This implies that for robust design, a materials manufacturer should focus more resources on uncertainty reduction for the crystallographic texture than on other microstructure attributes for Ti64. Similarly, surrogate models used to explore design space should be trained more thoroughly in these higher sensitivity regions. Additionally, the results imply that a nominal microstructure that achieves the performance of interest without relying on a basal-transverse texture would be more robust, as the basal-transverse texture results in the lowest FIP response of all common Ti64 textures. For example, if other microstructure attributes having a lower degree of uncertainty associated with them could be tuned to achieve the necessary FIP response whilst the crystallographic texture is kept random, then the upper limit of FIP response from a nominal basal-transverse texture would provide a robust design. Lastly, the statistical representation of this uncertainty, as opposed to simple error bounds, allows for precise understanding of the degree of reliability of a given design and decisions can be made accordingly.

3.7 Chapter Summary

The complicated interactions of each material system were mapped out and analyzed, the CPFEM models for each material system were described and calibrated, a global sensitivity analysis was conducted for each material system, and importance sampling was used to propagate distributions of uncertainty in microstructure attributes to quantify uncertainty in output properties of interest. Ultimately, importance sampling provided a coarse approximation of uncertainty in output properties, but remains relatively computationally expensive and may miss information for more complicated distributions, so moving forward, it is preferable to use surrogate modeling techniques in place of importance sampling for a more effective and efficient uncertainty quantification and propagation workflow. Later chapters in this work employ Gaussian process regression to create surrogate models to this end.

Chapter 4: Epistemic Model Form and Model Parameter Uncertainty Quantification in ICME Workflows for Fatigue Critical Computational Modeling

4.1 Digital Twin for Material Systems

The concept of a digital twin seeks to achieve a comprehensive functional description of a component, product, or system, including all pertinent information to the lifecycle [123]. The United States Air Force [124] has identified ICME as a key enabler for digital twins as a part of the need for an end-to-end system model, stating that the "Key to the application of ICME and the Digital Twin to airframe structures is location specific property representation, residual stress predictions at key locations, digital data management of actual histories at critical locations, and the ability to use microstructure material analysis as a basis for prognosis of crack propagation, etc."

Reliable prognosis of crack formation and propagation in naval aviation components requires understanding of physical mechanisms that drive fatigue behavior. Ti64 is a commonly used engineering alloy in fatigue critical naval aviation applications. The mechanisms of fatigue crack formation and growth in high cycle fatigue for Ti64 depend on microstructure attributes [63]. ICME workflows can be leveraged to model these fatigue responses. In this regard, there is a need to develop uncertainty quantification protocols within these ICME workflows to assure robust estimates of lifetime or relative fatigue resistance of various candidate microstructure forms for a given material system.

Aleatory uncertainty in the current context largely stems from the stochasticity of microstructure attributes that drive material properties and in turn performance [114]. In this chapter, epistemic uncertainty stemming from model form and model parameters is addressed.

Hennessey et al. [36] demonstrated the importance of considering epistemic uncertainty in computational modeling of fatigue crack formation and propagation, comparing two different crystal plasticity constitutive models for slip system nonlinear kinematic hardening of the cyclically stable stress-strain response of Al7075-T6. Although each model was calibrated to the same completely reversed, uniaxial cyclic stress-strain data at the level of polycrystal (i.e., many grain) response, there were substantial and important differences in the local, individual grain level responses of the models at small applied strain amplitudes associated with HCF. In this chapter, model form and model parameter uncertainty are investigated for ICME workflows used to model fatigue response in Ti64.

This investigation is carried out in a three step process corresponding to sections 4.4.1, 4.4.2, and 4.4.3 below. First, a convergence study is carried out to determine the number of SVEs and the size of each SVE needed to reduce uncertainty below an acceptable threshold. Next, the sensitivity of the model to seven model parameters is studied to determine the most sensitive parameters associated with a calibration of the model to experimental macroscale stress-strain data. Lastly, the local FIP response of the model to the four most sensitive model parameters is studied to determine the uncertainty in predicated FIP response of the material stemming from calibration with macroscale stress-strain data.

4.2 Digital Representation of Microstructures

Ensembles of SVEs are generated for a range of microstructure variants of Ti64 for analysis via CPFEM in ABAQUS [88]. These are generated using an open-source tool called DREAM.3D [89] that digitally reconstructs or develops statistically realistic geometric representations of the grains comprising a polycrystal. In this work synthetic microstructures are developed using realistic statistics. The model is fully voxelated and grain boundaries are handled implicitly through misorientation by DREAM.3D as well as explicitly in the CPFEM model, where slip is not allowed across a grain boundary. Previous work by Kern [90] has studied mesh sensitivity for the model used in this work.

Simulation outputs from the CPFEM model include stress, strain, and inelastic strain, from which common macroscopic polycrystal quantities of interest may be determined, such as elastic stiffness or yield strength. A RVE suitable for computing these quantities is relatively small in terms of number of grains/phases required for convergence (on the order of several hundred or thousands of grains). However, the concept of evaluating a RVE to compute surrogate fatigue crack formation driving forces (so-called FIPs) is not as useful due to their rare-event nature [92, 93], as it would require an RVE of excessive size and computational cost. Consequently, ensembles of SVEs are used to compute the statistical distribution of extreme value FIP response, for which both the size of the SVE (to incorporate important nearest neighbor effects) and number of SVEs needs to be determined to assess useful estimates of mean responses along with variance.

4.3 Epistemic Uncertainty Quantification Methodology

Epistemic uncertainty is addressed using interval analysis. Here the UQ problem translates to determining bounds on the output interval given interval bounds on the inputs. Any output response that falls within the output interval is a possible output, with no frequency information assigned to it [18]. This provides the limits of acheivable outputs for given inputs, which can be used in an inverse problem to deduce the allowable input space that will keep the bounds of outputs within an acceptable range. Since epistemic uncertainty is generally reducable by simulated a greater volume in the SVE ensemble, the bounds of outputs for given inputs can be constrained at the cost of greater computational expense.

In this work, a three-part study is carried out to quantify the uncertainty in extreme value FIP response due to model form and the calibration of model parameters to the macroscopic stress-strain response of the material. When calibrating a CPFEM model, it is typical to tune model parameters until the macroscopic stress-strain response of the model closely matches experimental data [91, 101]. These models are then used to investigate the relative fatigue criticality of various microstructures rank ordered using the FIP responses. Due to the large number of model parameters, it is possible to find different sets of model parameters or different model formulations that result in similarly adequate calibrations based only on the macroscopic stress-strain response; however, this may result in different local stress-strain responses and thus different FIP response. Clearly, more local experimental calibration data are desirable to address this issue. In general, it is useful to understand the sensitivity of response to model form and parameter uncertainties.

First, a convergence study for the extreme value FIP response is conducted with respect to the size and number of SVEs to quantify the dependence of uncertainty in quantities of interest on the model form. In this case "model form" relates to the compiled statistics of FIP responses based on a given SVE size and number of SVEs used to compile these statistics. In future work, we can also consider forms of deterministic constitutive models in the CPFEM pipeline to evaluate uncertainty in this regard. For our purposes, the approach taken here is useful in representing common methodology in applying a given CPFEM model framework, given aleatory uncertainty of microstructure combined with the epistemic uncertainty of the SVE sampling strategy. Accordingly, this model form issue is explored in this work, where we seek to find a minimum number and size for SVEs to reduce epistemic uncertainty below a manageable threshold.

Next, a parametric sensitivity analysis of the CPFEM constitutive model is carried out. Model parameters are varied one at a time to find local sensitivity of the model. The quality of the calibration with each parameter set is measured using the root-mean-squared (RMS) error of stress-strain data by comparing the simulated stress at strain response with a benchmark model having nominal parameter values. Stress is compared at strain increments of 0.0001 (corresponding to increments of 0.1 s of simulated time at a strain rate of $0.001\,\mathrm{s}^{-1}$). Parameter intervals are designated by varying each parameter such that the RMS error in stress-strain response is ~2% of the macroscopic yield strength of the benchmark Ti64 model, indicating that they represent an approximately equivalent calibration of the macro stress-strain response of the model. With each different parameter set demonstrating equivalent macroscopic response, the difference in extreme value FIP response is analyzed under ostensibly HCF loading conditions.

Finally, the parameter set is truncated to the four parameters exhibiting the greatest influence on extreme value FIP sensitivity. Four parameters are chosen because this is the largest number of parameters that can be feasibly simulated for a full factorial design to quantify the uncertainty in the extreme value FIP response by studying the resulting output interval. The boundaries of this output interval represent the uncertainty in the extreme value FIP response resulting from a calibration of these four model parameters using experimental macroscopic stress-strain dataset.

4.4 Results and Discussion

In this section the results of the three-part study are discussed in detail. First the SVE convergence study is described and the results are given in Section 4.4.1. Building on the results from Section 4.4.1, sections 4.4.2, and 4.4.3 provide a discussion of the results of a model parameter uncertainty quantification study. The fatigue model used for this chapter was described in Section 2.3 of this dissertation with further detail of model equations and parameters in Appendix A. FIPs were quantified as described in Section 3.4.

4.4.1 SVE Convergence Study

To quantify uncertainty in extreme value FIP response of Ti64 due to the number and size of SVEs in an ensemble, synthetic microstructures were instantiated. These microstructures had fully random crystallographic texture, 30% primary alpha phase by volume, and equiaxed grain with an average equivalent spherical diameter grain size of 30 μm and a log-normal distribution. The standard deviation was set to 7.5 μm and max and

min cutoffs for grain size were +/- 2 standard deviations from the mean. These particular statistics were used to represent a somewhat arbitrary but common Ti64 microstructure on which the uncertainty quantification workflow could be demonstrated. They were used to instantiate 18 separate ensembles of 50 SVEs with DREAM.3D. This provided three distinct ensembles of SVEs for each of the following SVE sizes: 50, 100, 150, 200, 250, and 300 grains per SVE on average. The number of elements per SVE was held constant at 27,000 and the number of elements in grains ranged from ~45 for small grain in the 300 grain SVEs to ~800 large grains in the 50 grain SVEs. FEM simulations were executed in which three fully reversed, strain-controlled uniaxial computational strain cycles with periodic boundary conditions were applied at a strain amplitude of 0.6% to promote elastic-plastic shakedown and FIPs are calculated after the third cycle. To represent statistical distributions of potential sites for fatigue crack formation, FIPs were computed at every element within the digital microstructures, after which volumetric averaging was performed. No more than one FIP was taken from each grain to prevent localized characterization and the top five highest FIPs from distinct grains in each SVE were used as a FIP thresholding strategy to ensure that only the extreme values at the tail end of the statistical distribution are characterized. These were fit to a Fréchet extreme value distribution to enable comparison of trends in the extreme value distribution of FIPs among various SVE ensembles. Additional test parameters for all testing in Section 4.4.1, 4.4.2, and 4.4.3 are given in Table 4.1.

.

Table 4.1. Computational test parameters.

Parameter	Value
Strain rate	0.001 s^{-1}
# of applied cycles	3
Strain ratio	-1
Temperature	300K
Elements	30^3 elements
Boundary conditions	Periodic

Figure 4.1 shows the 99th percentile of predicted extreme value FIPs versus total number of grains in an ensemble. Results were plotted using sub-ensembles from each of the 18 ensembles to demonstrate convergence as a function of SVE size and number of SVEs per ensemble. Sub-ensembles were made by looking at the Fréchet distribution of extreme value FIPs taken from smaller sub-groups of SVEs taken from the existing 50 SVE ensembles. For example a predicted 99th percentile extreme value FIP response corresponding to 4000 grain on the x-axis in Figure 4.1 could be generated by characterizing the FIP response of a sub-ensemble made up of the first 20 SVEs in a 50 SVE ensemble with 200 grains per SVE. These sub-ensembles were made up of 5, 10, 15, 20, 25, 30, 35, 40, 45, and 50 SVEs, respectively.

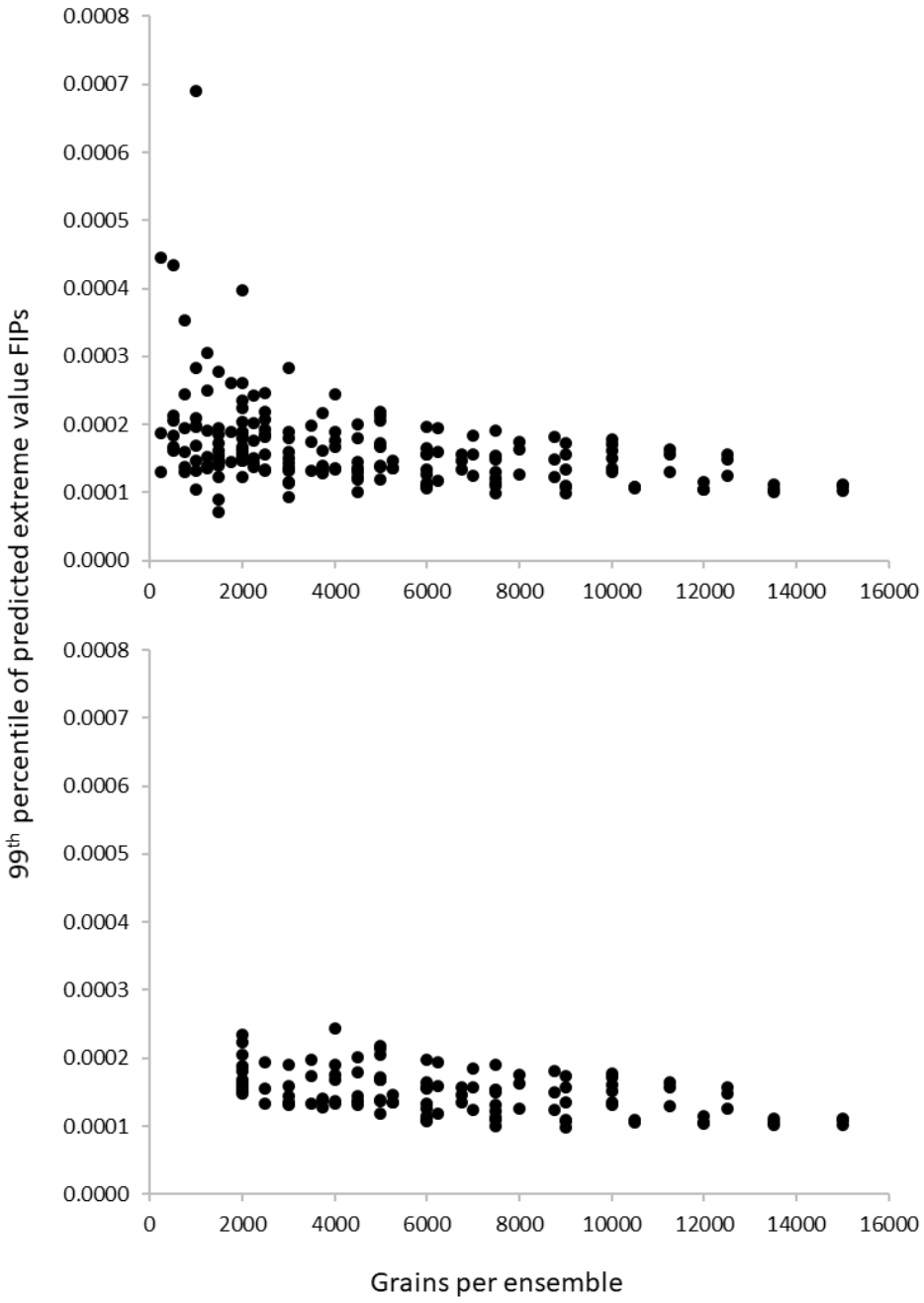

Figure 4.1. SVE size and number convergence study; predicted 99th percentile extreme value FIPs for all sub-ensembles (top) and for just those sub-ensembles having at least 20 SVEs and 100 grains per SVE (bottom).

The results show that there is a continuous reduction in variability as the simulated volume increases. This is expected; however, there is a tradeoff between computational fidelity and cost. The plot at the bottom of Figure 4.1 shows the results for only those sub-ensembles having at least 20 SVEs and 100 grains per SVE. A lower degree of variability/uncertainty is achieved with this combination than for ensembles with comparable total volume, demonstrating that both SVE size and number of SVEs should be optimized to reduce uncertainty and achieve convergence in an efficient manner. Increasing simulated volume can further reduce uncertainty, but ensembles of 20 SVEs and 100 grains per SVE achieve an acceptable degree of convergence for this study. Amongst 10 distinct ensembles with 20 SVEs and 100 grains per SVE, the 99th percentile of simulated extreme value FIPs range from 1.476×10^{-4} to 2.353×10^{-4}.

4.4.2 Model Parameter Sensitivity

FEM models are typically calibrated by comparing the macroscopic stress-strain response of the model with experimental data or a benchmark model, and tuning model parameters to reduce the error in the model response. These models are then used to investigate local stress-strain response to understand the fatigue response of a specific microstructure. To determine which model parameters contribute to the highest degree to uncertainty in local FIP response, a parametric sensitivity analysis was conducted of seven model parameters shown in Table 4.2. The same microstructure statistics were used as described in Section 4.4.1. A baseline calibration of model parameters was adapted from Smith [91] and updated to RMS error of stress-strain data by comparing the experimental and simulated stress at strain increments of 0.0001 (corresponding to increments of 0.1

seconds of experimental time at a strain rate of $0.001s^{-1}$). Thus at each data point along the stress-strain curve the stress of the new model was compared with that of the baseline model for a given strain value, and the RMS error was taken using the set of values generated by taking the difference between each of these pairs of stress values. Each parameter was varied one at a time to iteratively find intervals that result in RMS error in stress of 10-20 MPa, corresponding to ~1-2% of yield strength determined from the baseline model. A centered parameter study was used because the parameter values had all been previously calibrated, thus varying each parameter one at a time allowed the local sensitivity of the model within close proximity of the baseline model. This represents slight variations that could have been made in a different calibration.

Table 4.2. Ti64 model parameters investigated in sensitivity study.

Parameter		**Baseline**	**Minimum**	**Maximum**
$CRSS_{basal}$	Critical resolved shear stress in basal plane	339 MPa	333 MPa	345 MPa
$CRSS_{prism}$	Critical resolved shear stress in prismatic plane	266 MPa	253 MPa	279 MPa
α_{ps}	Correction factor for colony phase CRSS value	1.25	0.9	1.35
A_{dyn}	Dynamic recovery factor	8000	6650	9350
A_{factor}	Direct hardening coefficient over dynamic recovery coefficient	1	0.83	1.17
μ_{th}	Softening rate coefficient for threshold stress softening term	2.00	1.83	2.17
t_{soft}	Threshold stress softening term	42.0	37.5	46.5

For the macroscopic stress-strain sensitivity study, an ensemble of five SVEs with 300 grains per SVE was instantiated. This relatively smaller ensemble can be used because

the macroscopic stress-strain response converges much faster than local FIP response explored in Section 4.4.1. CPFEM simulations were carried out with each set of model parameters by subjecting SVEs to three fully reversed computational strain cycles. In this case a strain amplitude of 1% was used to induce macroscopic yielding for comparison with macroscopic stress-strain response of the baseline model.

More relevant to the issue of comparing microstructures in terms of fatigue resistance, the sensitivity of the extreme value FIP response to each model parameter was investigated next. Once again, CPFEM simulations were carried out with 20 SVEs and 100 grains per SVE in which three fully reversed computational strain cycles with a strain amplitude of 0.6% and the five highest FIPs from distinct grains were extracted from each SVE and fit to a Fréchet distribution to compare 99^{th} percentile predicted extreme value FIPs. The change in 99^{th} percentile FIPs compared with the baseline model parameter set is shown in

Table 4.3. It can be seen that the extreme value FIP response is highly sensitive to some model parameters within the acceptable macroscopic calibration intervals as the absolute error in 99^{th} percentile FIPs relative to the baseline model are as high 43% while the RMS error in the macroscopic stress-strain response is below 2% of the yield strength of the baseline model in all cases. The four most sensitive model parameters are connoted in the table by an asterisks next to the parameter names. These four model parameters were considered for UQ.

Table 4.3. FIP sensitivity analysis for model parameter intervals.

Parameter	Value	Macro stress-strain calibration error	Frechet FIP distribution		99th Percentile FIP	
			Slope	Intercept	Value	Absolute Error
$CRSS_{basal}$*	345	1.05%	1.65	18.5	$2.153x10^{-4}$	43%
$CRSS_{prism}$*	279	1.22%	1.83	20.2	$1.960x10^{-4}$	30%
α_{ps}	1.35	0.46%	1.97	22.1	$1.425x10^{-4}$	5%
A_{dyn}	9350	1.82%	2.42	26.2	$1.297x10^{-4}$	14%
A_{factor}	1.17	1.71%	2.14	23.4	$1.487x10^{-4}$	1%
μ_{th}*	2.17	1.60%	1.85	20.4	$1.991x10^{-4}$	32%
t_{soft}*	46.5	1.58%	2.07	23.3	$1.216x10^{-4}$	19%

To check the combined effects of varying these model parameters simultaneously, the macroscopic stress-strain response was simulated with all four of the selected model parameters varied to their max and min values in every possible combination, thus 2^4, or 16 RVEs were simulated and the RMS error of the resulting macroscopic stress-strain was calculated by comparing with the baseline model. Figure 4.2 shows the combination that resulted in the greatest calibration error; 2.75% of the baseline yield strength. This occurred when all four parameters were at their minimum values given in Table 4.2. This is near the limit of what would be considered an acceptable calibration, but still realistic, so the intervals of $CRSS_{basal}$, $CRSS_{prism}$, μ_{th}, and t_{soft} shown in Table 4.2 are employed in Section 4.4.3 to quantify uncertainty in local FIP response based on model calibration that considers error by comparing the model's simulated macroscopic stress-strain response with experimental data or a benchmark model.

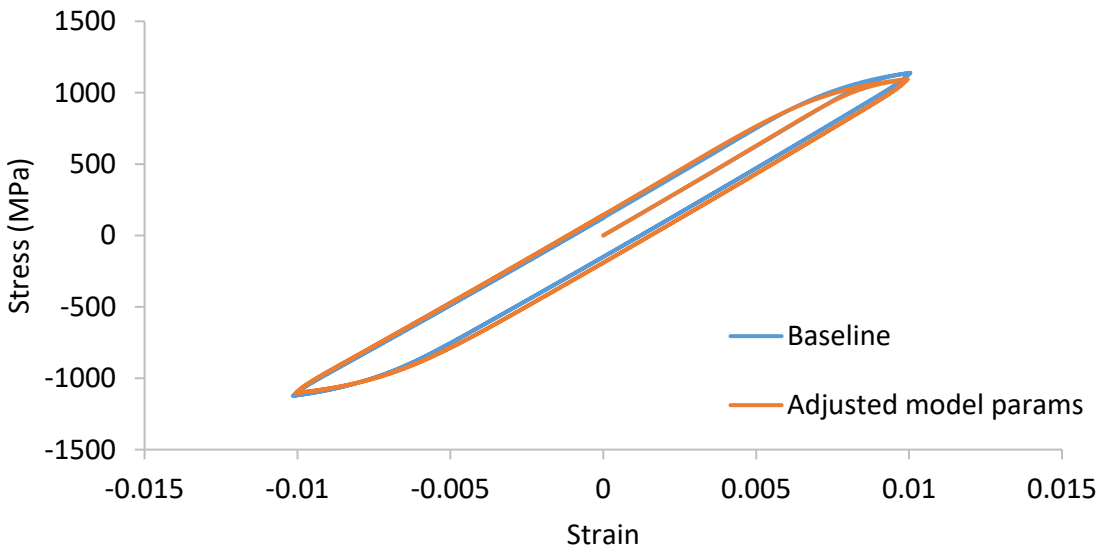

Figure 4.2. Macroscopic cyclic stress-strain response of Ti64 model for baseline and adjusted model parameters.

4.4.3 Uncertainty in Localized Response Resulting from Macroscale Informed Model Parameters

Having established intervals of uncertainty for input model parameters; $CRSS_{basal}$, $CRSS_{prism}$, μ_{th}, and t_{soft} in Section 4.4.2, uncertainty is propagated through the model using a full factorial experiment to quantify uncertainty in extreme value FIP response. Using the same ensemble of microstructure instantiations as in the study of sensitivity of FIPs described in Section 4.4.2, 20 SVEs with 100 grains per SVE were subjected to three fully reversed computational strain-controlled uniaxial cycles with a strain amplitude of 0.6%. The five highest FIPs from distinct grains were extracted from each SVE and fit to a Fréchet distribution to compare predicted 99^{th} percentile extreme value FIPs.

The factorial study of model parameters was made up of three discrete values per parameter, those being the minimum, mean, and maximum values for each model

parameter interval. The parameters were combined in all possible combinations giving a total of 81 test points. The predicted 99th percentile extreme value FIPs are shown in Figure 4.3 for all 81 model parameter sets. The resulting output interval ranges from 7.737×10^{-5} to 4.087×10^{-4}.

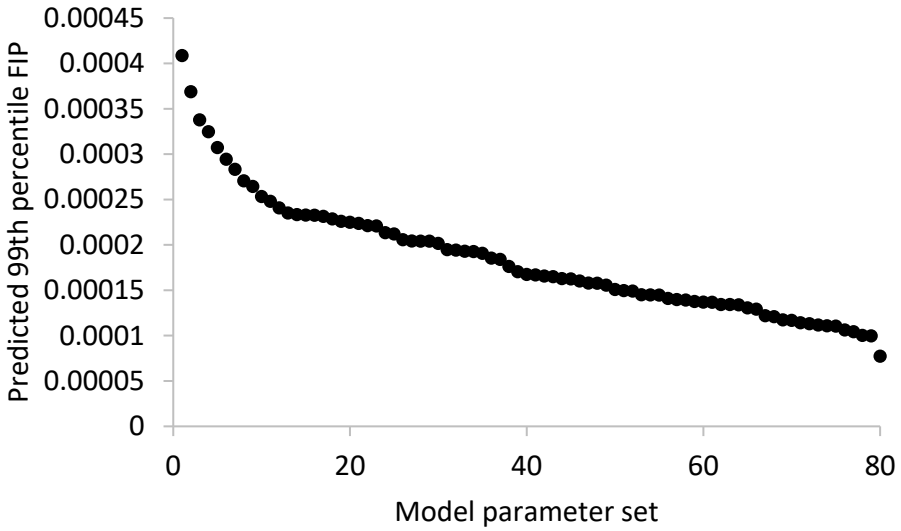

Figure 4.3. Predicted 99th percentile FIPs ordered for all 81 model parameter combinations.

The max and min FIP responses correspond to extreme combinations of model parameters with the exception of μ_{th} which does not appear to have as great an effect on the extreme value FIP response as the other parameters investigated.

Table **4.4** shows the model parameters combinations resulting in the max and min values of the output interval as well as the associated predicted 99th percentile extreme

value FIPs for these parameter combinations. The full extreme value distribution of FIPs using all four of these model parameter sets, as well as the baseline model, are shown in Figure 4.4. Figure 4.5 shows a Fréchet distribution corresponding to the model parameter sets resulting in the max and min extreme value FIP responses, as well as the uncertainty bounds associated with the ensemble size discussed in Section 4.4.1. The dotted lines are the Fréchet distribution fit to the data, and the solid lines represent the bounds of uncertainty due to model form (SVE size and number in ensemble).

Table 4.4. Parameter combinations giving output interval bounds for predicted 99th percentile extreme value FIPs.

Parameters	Interval limits	
	Parameters for min FIP response	Parameters for max FIP response
$CRSS_{basal}$	345 MPa	333 MPa
$CRSS_{prism}$	253 MPa	279 MPa
μ_{th}	2	1.83
t_{soft}	46.5	37.5
99th percentile FIPs	7.737×10^{-5}	4.087×10^{-4}

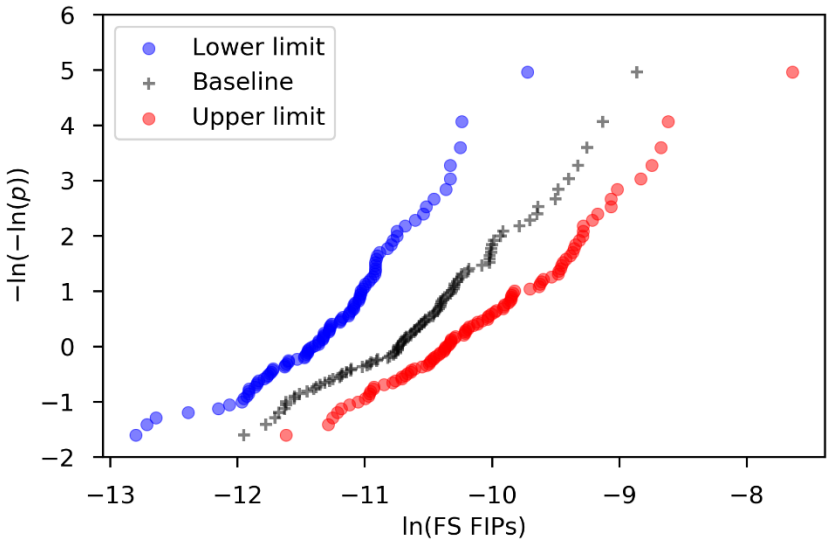

Figure 4.4. Extreme value distribution of FIPs on Fréchet plot.

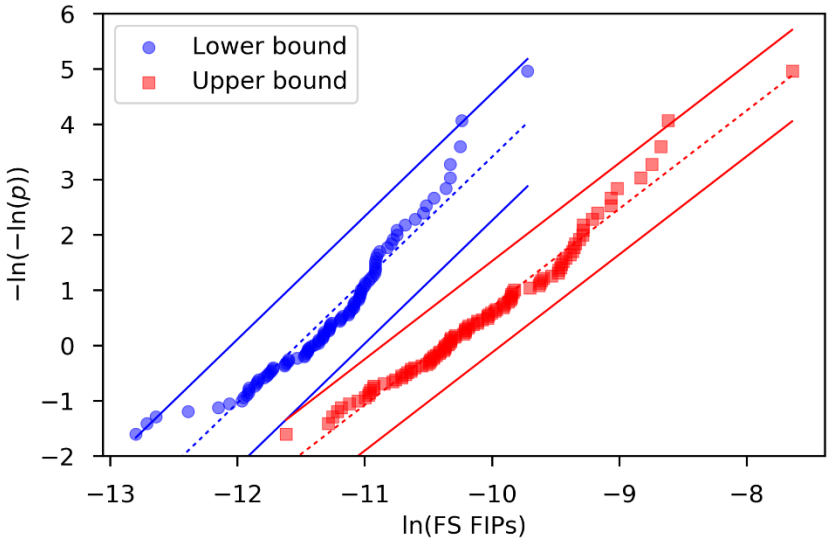

Figure 4.5. Extreme value distributions of upper and lower bounds of model parameter uncertainty with SVE convergence uncertainty limits.

In Figure 4.5, the outer solid lines (furthest right red line and furthest left blue line) represent the bounds of the uncertainty interval for extreme value FIP response resulting from combined model form and model parameter uncertainty. There is a substantial difference between the two extreme ends of the interval. Figure 4.6 shows the extreme value FIP response of four different microstructures having varied crystallographic textures typical of Ti64 that are known to exhibit different fatigue lives [100]. Simulations were carried out as described previously in Section 4.4.1 using ensembles of 20 SVEs with 100 grains per SVE; however, in this case four different microstructures were instantiated, having random, basal-transverse, transverse, and beta-annealed crystallographic textures, respectively. The <0001> pole figures are shown in Figure 4.7. Uniaxial straining was in the x-direction, representative of the left-right directions on the pole figures. For the random texture, the upper and lower bounds of the predicted FIPs resulting from model form and model parameter uncertainty are shown by the blue and red lines respectively. It can be seen that the total epistemic uncertainty in extreme value FIP response of the randomly textured microstructure is of a similar magnitude as the difference between the random and transverse textures. This demonstrates the importance of quantifying this uncertainty since the difference in extreme value FIP response between randomly textured and transverse textured Ti64 is generally considered to be significant in the context of rank-ordering microstructures for their fatigue performance.

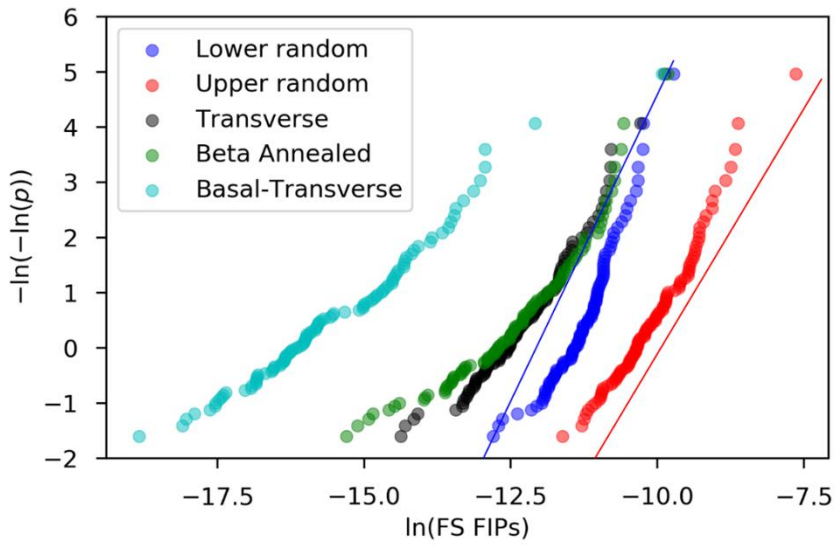

Figure 4.6. Extreme value distribution of FIPs for four common textures of Ti64 with upper and lower bounds of uncertainty shown for random texture.

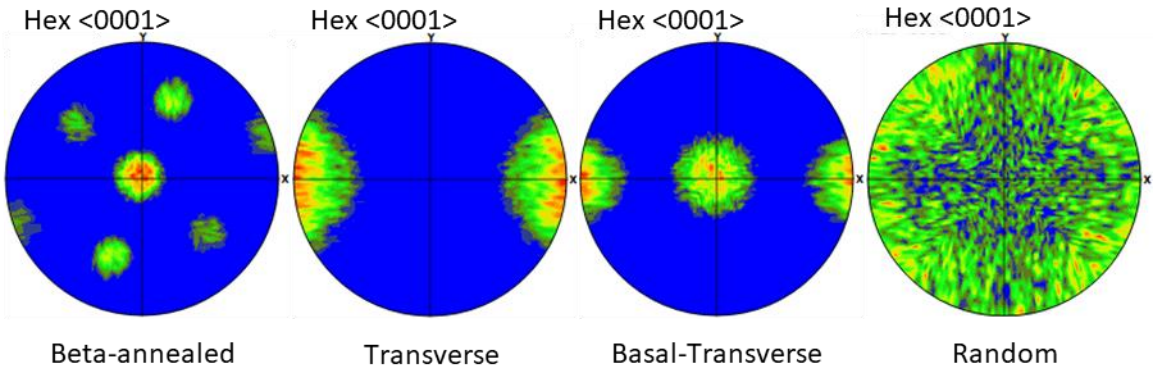

Figure 4.7. Pole figures of crystallographic textures used in Ti64 sensitivity analysis.

4.5 Chapter Summary

This chapter demonstrates the importance of considering model form and model parameter uncertainty when using ICME workflows, emphasizing the use of UQ to construct a reliable digital twin of a material system with the objective of monitoring and predicting fatigue crack formation. It is acknowledged that while the concept of a digital twin motivates this work, the current state of the art fatigue modeling and uncertainty quantification is not yet at the point where it can be applied directly to a digital twin at the individual component level. This work simply demonstrates the value of considering model form and model parameter uncertainty in the present framework.

The model form uncertainty was explored by studying the effects of number and size of SVEs in an ensemble on the resulting predicted extreme value FIPs in Ti64 with equiaxed grains and log normal grain size distribution. It was shown that at least 20 SVEs with at least 100 grains per SVE should be simulated to achieve an acceptable level of convergence, reducing variation in FIPs from an order of magnitude to approximately a multiple of two. Clearly, uncertainty remains and should be quantified in order to make reliable predictions using the associated model form. Additionally, model parameter uncertainty was considered by comparing different parameter calibrations. Simulated macroscopic stress-strain response of the model was compared with a baseline model that was previously calibrated by Smith et al. [91].

It was shown that of the seven parameters investigated, local fatigue responses (i.e., sub-grain level FIPs) were most sensitive to $CRSS_{basal}$, $CRSS_{prism}$, μ_{th}, and t_{soft}. Extreme value distribution of FIPs varied significantly with model parameters, while the

macroscopic calibration remained within 2.75% RMS error of the baseline model. These results indicate that uncertainty associated with the calibration of model parameters can have significant impact on prediction of fatigue performance and should be quantified in order to make reliable predictions. This ultimately requires validation of constitutive models and parameters for data collected from experiments that measure local (e.g., grain level) responses [36]. There is less impact on rank ordering microstructures for their fatigue resistance than on predicting fatigue life as that would require a higher degree of certainty.

Chapter 5: Machine Learning-Enabled Aleatory Uncertainty Quantification for Modeling Structure-Property Linkages for Fatigue Critical Engineering Alloys Using an ICME Workflow

5.1 Uncertainty Quantification in Materials Design

Uncertainty is manifested in all stages from materials processing through engineering component performance. Computational modeling of materials introduces unique uncertainties that differ from those encountered in experimental research. As such, there is a large body of research that rigorously couples UQ with ICME workflows [5-7]. Recent advances in UQ for fatigue modeling [10, 11] have established the use of Bayesian and genetic algorithm techniques for crystal plasticity model parameter and model form UQ. Additionally, Bayesian inference and Taylor expansion based uncertainty propagation methods have been used to propagate uncertainties associated with model reduction error, data sparsity error, and microstructural uncertainty using a crystal plasticity finite element modeling (CPFEM) model for dual phase alpha-beta titanium alloys [12, 14].

In particular, this chapter focuses on UQ as it pertains to structure-property linkages relevant to the design of engineering alloys for fatigue critical applications, specifically Ti64. Reliable prognosis and inspection of such components requires understanding of physical mechanisms that drive fatigue behavior. The mechanisms of fatigue crack formation and growth in high cycle fatigue for Ti64 depend on microstructure attributes

[51]. ICME workflows can be constructed to model these fatigue responses. In this regard, there is a need to develop UQ protocols within these ICME workflows to assure robust estimates of lifetime or relative fatigue resistance of various candidate microstructure forms for a given material system.

To build uncertainty informed workflows to provide decision support for development of fatigue critical engineering alloys, robust design concepts can be utilized. Robust design has gained widespread attention in ICME with applications in reliable decision-making for complex engineering systems [47], seeking solutions that are relatively insensitive to small changes in uncertain quantities [23]. This work demonstrates UQP protocols that can be utilized to integrate UQ methodology with state-of-the-art robust design methods such as IDEM [51, 97].

UQ in ICME should consider both the inherent, irreducible (i.e., aleatory) uncertainty in the system and uncertainty that can be reduced by increasing the knowledge of the system (i.e., epistemic) [5, 11-14]. Aleatory uncertainty in this space stems from the stochasticity of microstructure attributes that most closely correlate with material properties and in turn performance [114]. This chapter focuses primarily on the treatment of aleatory uncertainty. Epistemic UQ has been addressed in previous work [125], and its effects will also be included here.

Statistical methods have been explored for aleatory UQP. Sandia National Laboratories' Dakota toolkit largely focuses on forward propagation of uncertainty [18]. However, UQP for statistical distributions presents a large computational burden owing to dimensionality [24], so reduced order surrogate models are often used instead of high fidelity computational models. The surrogate modeling methods for UQP include GP

regression models [6, 25-27], and stochastic expansion methods (e.g. Polynomial Chaos Expansion, partial differential equations) [28-30]. Owen et. al. found little difference in quality of UQP resulting from these surrogate approaches. However, GP regression models are more flexible, having no experimental design restrictions, and offer a much wider range of behavior descriptions beyond polynomial functions [31]. Additionally, GP models provide quantification of uncertainty introduced by the surrogate model itself. The major drawback of GP models is that they lose efficiency in high dimensional spaces – particularly with greater than 12 variables [32]. However, the number of variables considered in this work does not exceed these limitations.

5.2 Aleatory Uncertainty Quantification and Propagation Methodology

As previously described in Section 2.5 uncertainty in ICME workflows arises from several sources. The focus of this chapter is the quantification and propagation of MSU resulting from natural stochasticity in microstructures that emerges from the PS linkages. Once quantified, it must be propagated through SP linkages to determine uncertainty in output properties of interest. In order to facilitate this aleatory uncertainty quantification and propagation process, model uncertainty must be reduced. In this context, model form uncertainty refers to noise resulting from the selection number and size of SVEs used to compute distributions of FIPs, as well as uncertainty introduced when reduced order models are used as surrogates for more expensive high fidelity ICME models.

Cai and Mahadevan [22] used statistical methods to investigate uncertainty in the initial conditions and manufacturing process parameters on the microstructure and

mechanical properties of materials. They propagate MSU to an uncertainty of macroscopic mechanical properties of the material using computational models.

One major difficultly that arises with this sort of uncertainty propagation is establishing precise cause and effect linkages between processing, structure and properties, across which uncertainty should be propagated. In design engineering QFD tools are used to call attention to the customer needs. These QFD tools provide a structured approach to define customer requirements and translate them to engineers in the form of engineering attributes. A PSPP map is an analogous system design chart for materials design that helps materials engineers easily identify important linkages [4]. PSPP maps provide key microstructural subsystems, primary links of these subsystems to properties they control, and the stages of processing that govern their dynamic evolution [4].

In this work, uncertainty in microstructure attributes was propagated from the "structure" column of a PSPP map to the "property" column, to establish workflows allowing design engineers to robustly quantify uncertainty in material properties of interest.

Another challenge that complicates the uncertainty propagation process is the immense computational cost of brute force PDF propagation using high fidelity computational simulations, including the ones needed to investigate fatigue performance of a polycrystalline material based on crystal plasticity. The MC method is commonly used to propagate uncertainty through computational simulations. PDFs are randomly sampled and the model is run for each of the sampled inputs to generate an output distribution [18]. The disadvantage of MC is that a large number of samples are required to accurately estimate the output statistics. Therefore, as a practical concession, surrogate modeling techniques are often used to propagate statistical uncertainty.

The GP model can be thought of as a surrogate for the high fidelity CPFEM model that takes as inputs the microstructure statistics and, when adequately trained, renders accurate predictions of output quantities of interest. The inner workings of this surrogate model consist of a kernel object, or covariance function, that acts as a prior distribution, with hyperparameters that are optimized with training data [96]. In this work, a Matérn kernel function was used to approximate the SP linkages.

A Matérn kernel is a stationary kernel that is a generalization of the infinitely differentiable radial basis function kernel. The generalization allows for the user to determine the differentiability of the kernel function with a parameter ν. This controls the smoothness of the resulting function. Additionally, the Matérn kernel is parameterized by a length-scale parameter $l > 0$, which can be a scalar for isotropic variation or a vector with the same length as the input vector $\mathbf{x}$ for anisotropic variation. The Matérn kernel [32] is given by

$$k(x_i, x_j) = \sigma^2 \frac{1}{\Gamma(v)2^{v-1}} \left[\gamma\sqrt{2v}d\left(\frac{x_i}{l}, \frac{x_j}{l}\right)\right]^v K_v \left[\gamma\sqrt{2v}d\left(\frac{x_i}{l}, \frac{x_j}{l}\right)\right] \qquad \textbf{(5.2.1)}$$

The use of a GP surrogate model implicitly assumes a normal distribution in uncertainty of surrogate model predictions, which may not necessarily always be a good assumption, depending on the data at hand. For this reason, it is vitally important to validate the predictions of a GP regression model before it is used a surrogate model.

These GP surrogate models were trained with an initial ten point training set sampled from the microstructure space using Latin hypercube sampling (LHS) and validated using the leave one out cross validation (LOOCV) method. The LOOCV method was used to

compare the quality of predictions from the surrogate model with predictions from the high fidelity ICME model, and an uncertainty driven adaptive sampling method was employed, wherein new samples were chosen based on locations in the design space having the highest predicted GP uncertainty.

5.3 Results and Discussion

In this Section, the results of the research undertaken for this chapter are discussed in detail. First, in Section 5.3.1, a PSPP map is presented for Ti64, and the structure-property linkages being modeled are highlighted. Second, in Section 5.3.2, the epistemic uncertainty, or noise, in the predicted modulus of elasticity, yield strength, and distribution of extreme value FIPs was quantified and reduced to a level that allowed for a reasonable tradeoff between computational cost per simulation, and reliability of prediction results. Next, in Section 5.3.3, GP models were trained as surrogates for the CPFEM model, and the results of models trained with reduced levels of epistemic uncertainty were compared with GP models trained with data with greater uncertainty to demonstrate the value of uncertainty reduction. Finally, in Section 5.3.4, aleatory uncertainty in the form of probability distributions of microstructure statistics was propagated from structure to responses/properties using the GP surrogate models, and resulting uncertainty in properties of interest are presented.

All CPFEM simulations used to compute FIPs in this work were based on the third full cycle of three fully reversed, strain-controlled uniaxial computational strain cycles with periodic boundary conditions at a strain amplitude of 0.6%. Room temperature and

quasistatic strain rate conditions were employed. To represent statistical distributions of potential sites for fatigue crack formation, local quantities were computed at every integration point/element within the digital microstructures, after which volume averaging was performed to compute FIPs. No more than one FIP was taken from each grain to prevent localized characterization. The top five highest FIPs from distinct grains in each SVE were used as a FIP thresholding strategy to ensure that only the extreme values at the tail end of the statistical distribution were characterized. These were fit to a Fréchet extreme value distribution to enable comparison of trends in the extreme value distribution of FIPs among various SVE ensembles. Additional test parameters for all simulations in Section 5.3.2, 5.3.3, and 5.3.4 are given in Table 5.1.

Table 5.1. Computational simulation parameters.

Parameter	Value
Strain rate	$0.001s^{-1}$
# of applied cycles	3
Strain ratio	-1
Temperature	300K
Elements per SVE	30^3 elements
Boundary conditions	Periodic

The fatigue model used for this chapter was described in Section 2.3 of this dissertation with further detail of model equations and parameters in Appendix A. FIPs were quantified as described in Section 3.4 and simulated microstructures were digitally represented in accordance with the description given in Section 4.2.

5.3.1 Ti64 PSPP Map

The first step toward robust propagation of MSU to quantify uncertainty in properties of interest was to define the PSPP map for the material system of interest, in this case Ti64. Next, the structure-property linkages that are to be modeled must be identified and the associated microstructural features must be understood. To this end the PSPP map for Ti64 for fatigue critical applications is shown in Figure 5.1. The microstructure attributes that were modeled by the CPFEM model used in this work are highlighted in green along with the process steps and properties linked to these microstructure attributes.

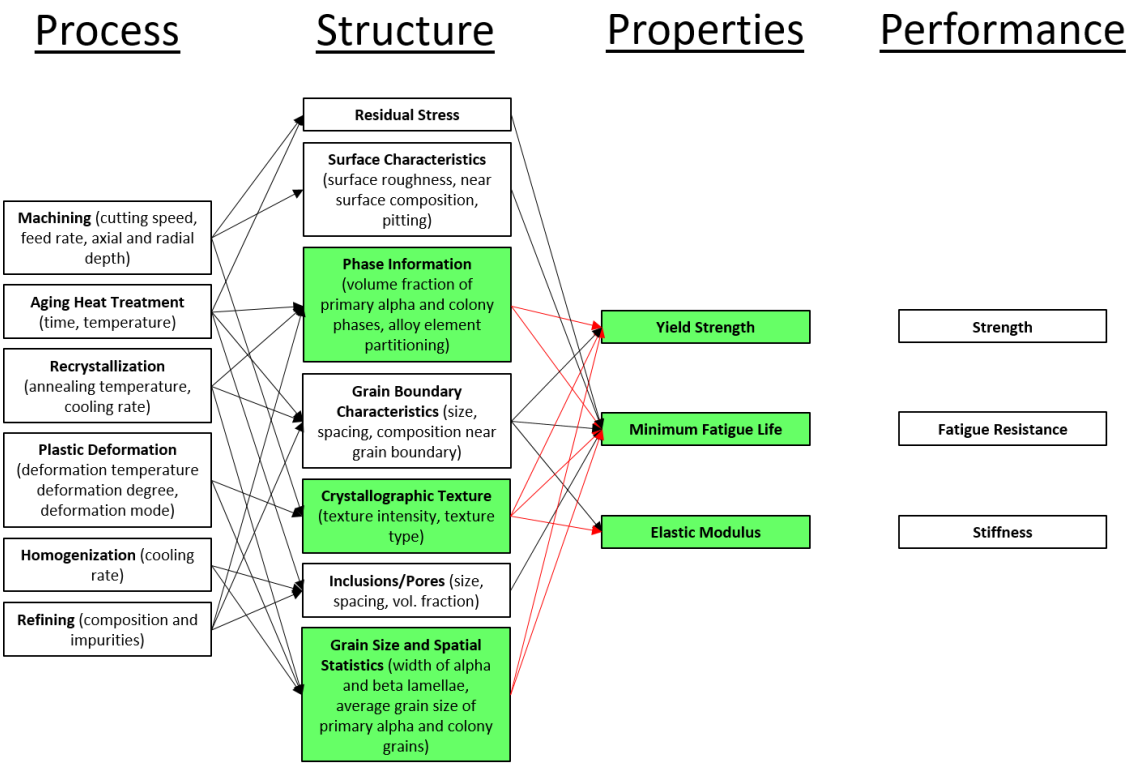

Figure 5.1. PSPP map for Ti64 used in fatigue critical applications with structure-property linkages considered in this work highlighted in green.

The PSPP map is rather complicated and contains seven important microstructural features. For this work, only three were considered; Grain size and spatial statistics, crystallographic texture, and phase information, which were quantified as average grain size, a categorical texture type (such as random texture, or transverse texture), and the volume fractions of primary alpha phase in the alpha-beta material. These three microstructure attributes were the focus of this thesis because there had been extensive previous work within the McDowell group to model these SP linkages with the Ti64 CPFEM model used for this work. Similar methodology to that demonstrated in this work could be applied to the additional four microstructure attributes in white boxes in the structure column in Figure 5.1 to further improve the UQ for properties of interest in the design of Ti64 for fatigue critical applications. These additional attributes are expected to be of great importance for metals additive manufacturing, for example.

5.3.2 Uncertainty Quantification and Reduction for CPFEM Simulations

The stochastic nature of polycrystalline microstructures leads to noise or variability in the output responses/properties from CPFEM simulations for a limited set of SVE ensembles. The design of the SVE size and number of SVEs in each ensemble provides an opportunity to reduce epistemic uncertainty associated with the extreme value distribution of FIPs [125]. In order to train GP surrogate models, it is important to understand the level of noise in the training set, and to reduce the noise enough for data trends to be discernable. Due to the significant computational expense of high fidelity CPFEM simulations, a tradeoff must be made between reducing this source of noise along with limiting the

volume of material simulated. Rather than focusing on the uncertainty associated with realistic representation of microstructure, which concerns process-structure relations or materials characterization and microstructure reconstruction, this chapter was instead focused on the methodology for projecting uncertainty of assigned distributions of key microstructure attributes during the instantiation process of building SVEs.

To find a reasonable tradeoff between these conflicting goals, a study of the volume of simulated material (e.g., number of SVEs of a given size comprising the ensemble) versus noise in output responses/properties of interest was conducted. For this study, four different crystallographic textures commonly seen in Ti64 were considered; random (no distinct texture), transverse, beta-annealed, and basal-transverse.

Of the four crystallographic textures studied, Ti64 having basal-transverse texture resulted in the largest degree of noise in resultant extreme value distributions of FIPs. Specifically, if two different ensembles of SVEs are instantiated from the exact same microstructure statistics, (e.g. basal transverse texture, 30% primary alpha volume fraction, and 30 μm average grain size) and each ensemble is subjected to the exact same loading conditions, the predicted 99^{th} percentile FIP from the resulting extreme value distribution of FIPs will be slightly different from one ensemble of SVE instantiations to another. This difference in output given the same target input is what we refer to as noise. According to this definition of noise, BT texture creates the noisiest results of any of the four textures studied herein. For this reason, and to limit the computational burden of this study, the study of the tradeoff between noise and volume of simulated material was carried out for only the BT texture. Once a final volume of simulated material was chosen, the other three textures were simulated to confirm that they resulted in less noise.

To quantify noise in extreme value FIP response of Ti64 due to the number and size of SVEs in an ensemble, synthetic microstructures were instantiated. These microstructures had basal-transverse crystallographic texture, 30% primary alpha phase by volume, and equiaxed grains with an average equivalent spherical diameter grain size of 30 μm and a log-normal distribution. The standard deviation was set to 7.5 μm and max and min cutoffs for grain size were +/- 2 standard deviations from the mean. This choice of statistics for volume fraction of primary alpha phase and average grain size were chosen to represent a common Ti64 on which the uncertainty quantification and reduction (UQR) workflow could be demonstrated. These microstructure statistics were used to instantiate 60 different ensembles of SVEs. The ensembles were made up of all 12 combinations of three different SVE sizes; 100, 200, and 300 grains per SVE, and five different numbers of SVEs per ensemble; 10, 15, 20, 25, 30, having at least 200 grains per SVE or 20 SVEs per ensemble (i.e. combinations like 10 SVEs and 100 grains per SVE were not included). Each ensemble size was instantiated five times to compute the noise in predicted 99^{th} percentile extreme value FIP response. Figure 5.2 presents the results of this study.

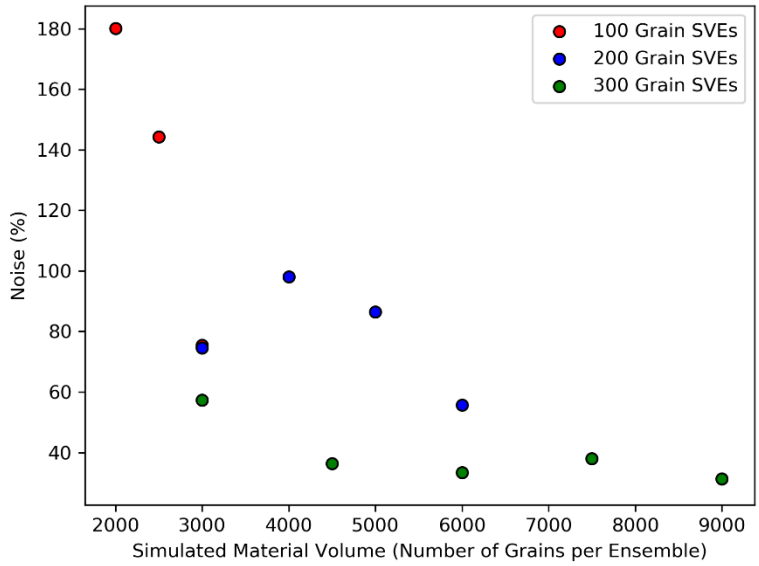

Figure 5.2. Simulated material volume in ensemble versus noise of predicted 99th percentile extreme value FIP response.

The noise in predicted 99th percentile extreme value FIP response (FIP_{99}) for all 12 ensemble sizes is shown in Figure 5.2. The x-axis shows the total number of grains in an ensemble (e.g. for an ensemble having 30 SVEs and 200 grains per SVE the total simulated material volume is 6000 grains). The y-axis shows the noise in predicted FIPs across the five instantiations of each ensemble size. This noise value was calculated using a LOOCV-like approach, wherein the difference between each instantiation of a given ensemble size and the average of the other four instantiations of that size was calculated, and then the average of this metric for all five instantiations was plotted. Equation (***5.3.1)*** and (***5.3.2)*** below were used to calculate this noise value, where n is the number of instantiations of a given ensemble size (in this case n=5), and $FIP_{99,i}$ is the predicted 99th percentile extreme value FIP for a given ensemble instantiation.

$$Noise = \frac{\sum_{i=1}^{n}\left[\frac{\left|FIP_{99,i} - \overline{FIP}_{LOO}\right|}{\overline{FIP}_{LOO}}\right]}{n} \qquad \textbf{(5.3.1)}$$

Here

$$\overline{FIP}_{LOO} = \frac{\left(\sum_{j=1}^{n} FIP_{99,j}\right) - FIP_{99,i}}{n-1} \qquad \textbf{(5.3.2)}$$

The results of the noise study for the basal-transverse textured Ti64 show that, as expected, noise decreases as the simulated material volume (and thus computational expense) increase. As shown in previous work [125] the balance of grains per SVE and number of SVEs per ensemble also influences uncertainty, as can be seen when comparing the results of ensembles with the same simulated material volume. For example, the ensembles having 20 SVEs and 300 grains per SVE produced less noisy responses than the ensembles having 30 SVEs and 200 grains per SVE, despite comprising the same cumulative simulated volume of material. This illustrates the importance of optimizing both number of SVEs and grains per SVE before committing significant computational resources to studying FIP response of a material. For the purposes of this work, the noise remained quite high even with the least noisy dataset, at 31.37% for ensembles having 300 grains per SVE and 30 SVEs per ensemble. To avoid excessive computational cost to run training simulations for a GP model, the ensemble size of SVEs was limited to 9000 grains;

however, it is likely that noise could be reduced further by increasing ensemble size. Additional steps were taken to reduce this noise more efficiently.

To further reduce noise in FIP_{99}, a FIP thresholding study was carried out. First, ensembles of 300 grains per SVE and 30 SVEs per ensemble were instantiated for all four textures of interest; random, transverse, beta-annealed, and basal-transverse. Then, using the same method of calculating noise as previously shown in Equation (***5.3.1)*** and (***5.3.2)***, the noise in FIP_{99} across five instantiations generated from ostensibly identical microstructure statistics was calculated. Figure 5.3 shows the results for all four textures. The left-most points show the noise in FIP_{99} when using just the top 100 FIPs to characterize the EVD. As shown previously, the noise in results from the basal-transverse textured material is 31.7% and, as expected, the noise is lower for the other three textures. For a given ensemble, with 30 SVEs and 27,000 voxels per SVE (each SVE is a cube having dimensions of 30x30x30 voxels) there are 810,000 unique FIPs generated from which approximately 4,500,000 unique sub-band averaged (SBA) FIPs are produced. The top SBA FIP from each grain in the ensemble makes up a sub-group of 9000 FIPs from which we can sample to generate EVDs. As seen in Figure 5.3, the EVD is characterized using the top 1-10% of these extreme value FIPs. It is preferable to limit the number of FIPs used to avoid over-influencing the resultant FIP distributions with lower FIPs that are not of as much interest when characterizing a material's resistance to fatigue failure. Figure 5.3 shows that, for the given loading parameters, including 400 top FIPs in the EVD used to compute FIP_{99} appears to provide the best compromise of reducing noise while still focusing on the highest extreme values of FIPs.

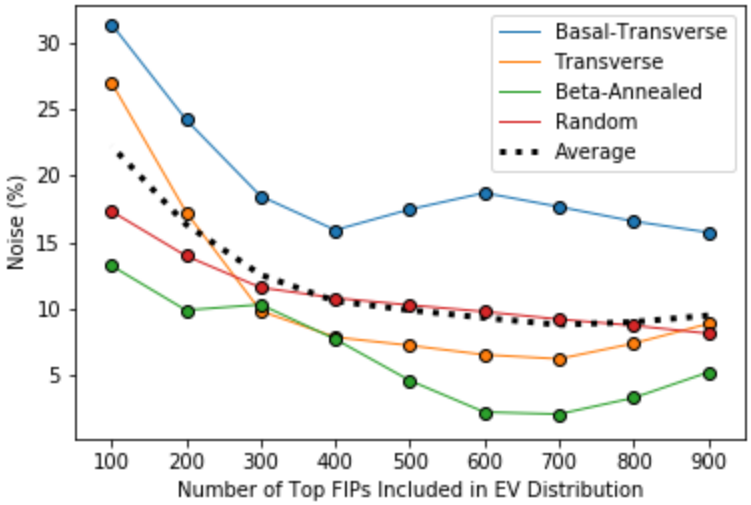

Figure 5.3. FIP thresholding versus noise in predicted 99th percentile extreme value FIP response for four common textures seen in Ti64.

The results of this UQR study show that the noise in FIP_{99} for Ti64 with 30% primary alpha phase by volume, and equiaxed grains with an average equivalent spherical diameter grain size of 30 μm and a log-normal distribution with a standard deviation of 7.5 μm, can be reduced to 7.72%, 7.87%, 10.81%, and 15.91% for beta-annealed, transverse, random, and basal-transverse textures, respectively. Compared with an initial noise value of 180.06% for the basal-transverse texture without optimization of ensemble size and FIP threshold, this represents an order of magnitude reduction in uncertainty. Having reduced noise to such an extent, the next step is to train GP surrogate models to predict FIP_{99} more effectively.

5.3.3 Training and Validation of Gaussian Process Surrogate Models

High fidelity CPFEM simulations used to predict fatigue performance of materials by quantifying predicted extreme value FIP response are quite expensive. To propagate uncertainty associated with microstructure statistics for a material such as Ti64 from known distributions of microstructure attributes to output properties of interest like FIP_{99} and yield strength, it is necessary to reduce the computational cost of making such predictions. For example, to reasonably characterize an output distribution of FIP_{99} response given input distributions of average grain size and volume fraction of primary alpha phase, a Monte Carlo approach might use 10,000 samples (100 bins across each input distribution). However, to generate one sample using and ensemble of 30 SVEs and 300 grains per SVE requires about 200 hours of CPU time to complete three fully reversed loading cycles for a strain amplitude of 0.6% with a high fidelity CPFEM simulation as defined previously in Section 3. This means that to propagate uncertainty in one material with a two dimensional input uncertainty space would require 2,000,000 CPU hours, or ~230 years of CPU time. Clearly, this is prohibitively expensive, which is why a surrogate model was used to replace the high fidelity CPFEM model to propagate uncertainty.

In the present work, GP regression models were trained using the results of CPFEM simulations for FIP_{99} and yield strength values generated across an input space of average grain size and volume fraction of primary alpha phase ranging from 10μm to 60μm, and 0.3 to 0.6, respectively. Texture was included as a third, categorical, input and two textures were used; random and transverse. These two textures were used to demonstrate multiple texture inputs while the other two textures studied in Section 3.2 were not included to reduce computational cost of training sets, and avoid redundant demonstration of the

uncertainty propagation process, however, the same process would equally apply for beta-annealed and basal-transverse textures.

A LHS strategy was used to sample from the two continuous inputs; average grain size, and volume fraction of primary alpha phase. For the initial training set 10 samples were taken from the input space for each texture. To generate training data for the GP surrogate models predicting 99^{th} percentile extreme value FIPs, the same HCF loading conditions as described previously in Section 5.3 were used and the ensembles for each training point consisted of 30 SVEs and 300 grains per SVE. The extreme value distributions of SBA FIPs were characterized using the top 400 FIPs from the sub group of extreme value FIPs as described in Section 5.3.2.

The GP surrogate model was trained using a linear combination of a Matérn kernel and a white noise kernel, the latter of which was included to capture the noise in the training data. The resulting GP models for each texture consist of two input dimensions (average grain size, and volume fraction of primary alpha phase) and two outputs (predicted 99^{th} percentile extreme value FIPs, and standard deviation in the predicted values). In the present work, the two outputs were treated as independent, meaning the covariance of the outputs was not accounted for when training the GP surrogate models. This is a simplifying assumption, used here because GP regression models with multiple outputs including covariance predictions are highly non-trivial and are currently an active field or research in machine learning [126, 127]. It is worth noting that there is likely some degree of covariance between yield strength and EV FIPs that is not being captured in the present implementation. That does not mean that the present framework is invalid, as a validation study in Section 5.3.3 will demonstrate that the GP surrogate models can still be quite

predictive without including the covariance between outputs. However, by not including the covariance between outputs it is possible that we lose some information that could be used to help improve the GP surrogate model performance, so it may be valuable for future work to explore an approach that accounts for covariance in yield strength and EV FIPs to potentially improve on the surrogate modeling framework.

Figure 5.4 shows a cross section of the GP surrogate model's prior and posterior distributions and training data for FIP_{99} from Ti64 having a random texture. It is important to note that each point along the x-axis in this plot has a different volume fraction of primary alpha phase, which can be regarded as a third dimension out of the page. This plot is shown this way simply to allow the reader to see clearly how a GP surrogate model addresses UQ for the additional uncertainty associated with its fit per se. This uncertainty is shown by the gray shading surrounding the black curve which represents the mean prediction of the GP model. Not surprisingly, uncertainty in GP predictions is higher further away from training points. The multi-colored oscillating curves represent ten of the theoretically infinite instantiations of the curve, where the black prediction curve represents the mean value of all instantiations, and the gray shaded area represents one standard deviation from the mean in either direction.

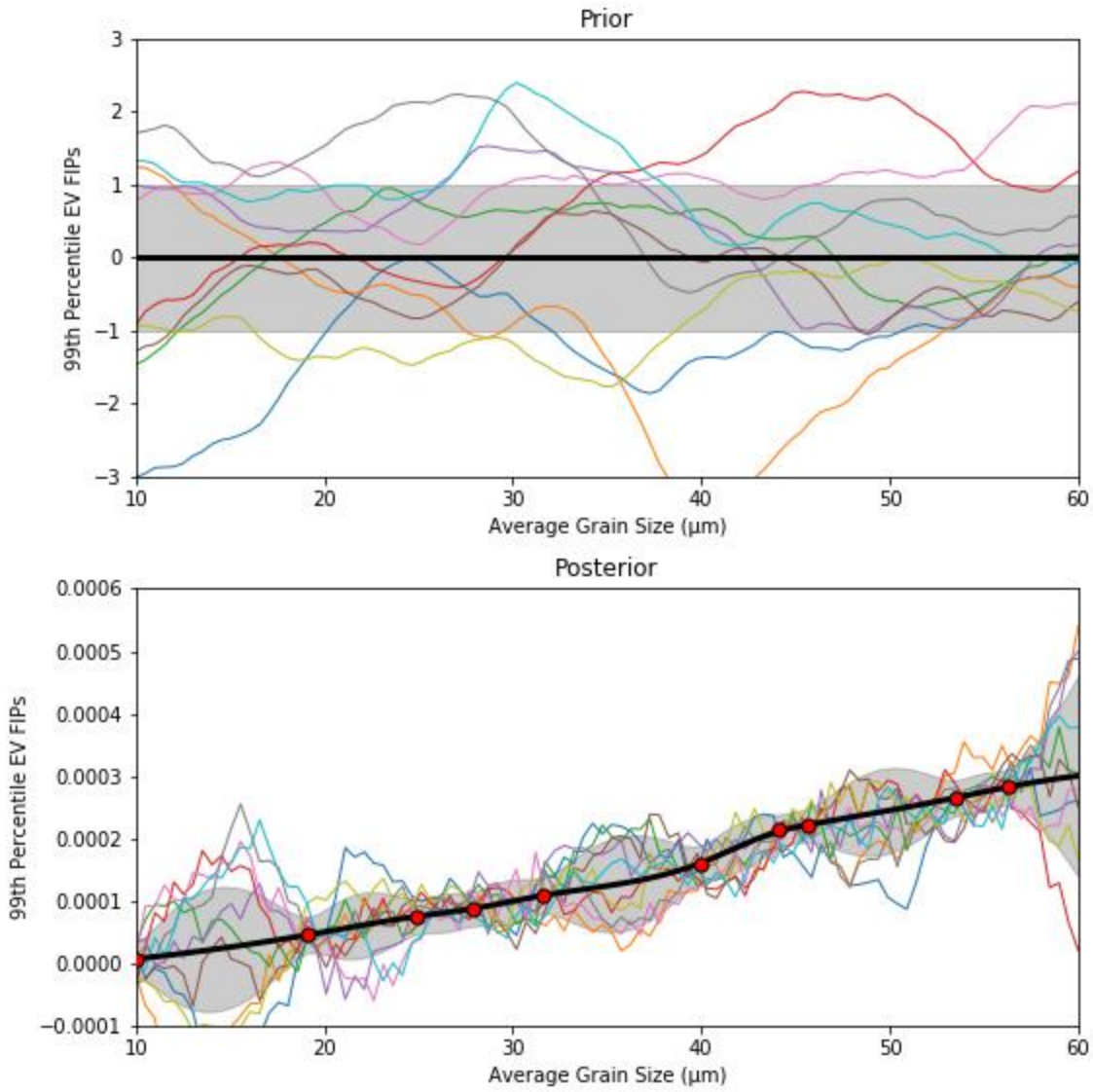

Figure 5.4. 2D slice of (top) prior and (bottom) posterior distributions from random texture GP model predicting 99th percentile extreme value FIPs.

The trained surrogate model for random textured Ti64 is shown with both input dimensions in Figure 5.5. The ten training data sampled using LHS are shown in red in Figure 5.5a and b. Figure 5.5a shows the GP model trained using data with noise reduction techniques as described in Section 3.2. The adjusted performance metric shown on each plot is a measure of how well the surrogate model predicts the output property of interest,

relative to the performance of the high fidelity CPFEM model simulations with noise reduced. This was calculated using a LOOCV technique, wherein one training sample was removed and the model was trained with the remaining training samples, then the resulting model was used to predict the value of the output of interest given input dimensions of the training sample that was withheld. The difference between the prediction and the actual training sample was calculated as a fraction of the actual training sample value, and this process was repeated for every training point in the training set. The final score was calculated by subtracting the average error of all samples from 1.000, thus a perfect score would be 1.000. The adjusted score is the GP prediction score divided by the score of the training data itself (i.e., if the training data has 10% noise the score of the training data is 0.9, and the adjusted score of the GP model is the original score divided by 0.9). As such, an adjusted score of 1.000 represents a GP model that perfectly reproduces the CPFEM model. In this work, an adjusted score of 0.95 was set as the threshold for a "good" surrogate model.

Figure 5.5b shows a GP model trained with the same 10 training samples from the input space, using noisy data produced from ensembles of 20 SVEs and 100 grains per SVE, and only the top 100 FIPs utilized when FIP thresholding. Figure 5.5c is a GP model trained with five additional training points, selected adaptively based on the points in the GP model with the highest standard deviation in predictions. With these additional five training data we see that the score improved to 0.7147, however, it remained substantially worse performing than the model trained on less noisy data, which had a score of 0.9673. Additionally, with 15 noisy training points compared with just 10 less noisy training data

for the better performing model, the computational time of producing each training set was comparable, as the less noisy data was more expensive to produce per sample point.

Finally, Figure 5.5d shows the score of the GP model versus the number of training points for the noisy training data. We can see that it is not clear that simply using more data would result in comparable performance. In fact, it is unlikely that the performance of a GP model trained on noisy data would ever approach the performance of the model trained on less noisy data, since the model can only make predictions with at best, the same amount of uncertainty as was present in its training data. Thus, the slightly more computationally expensive simulations needed to produce less noisy data were necessary to achieve strong surrogate model performance such that uncertainty distributions could be reliably propagated using the surrogate models.

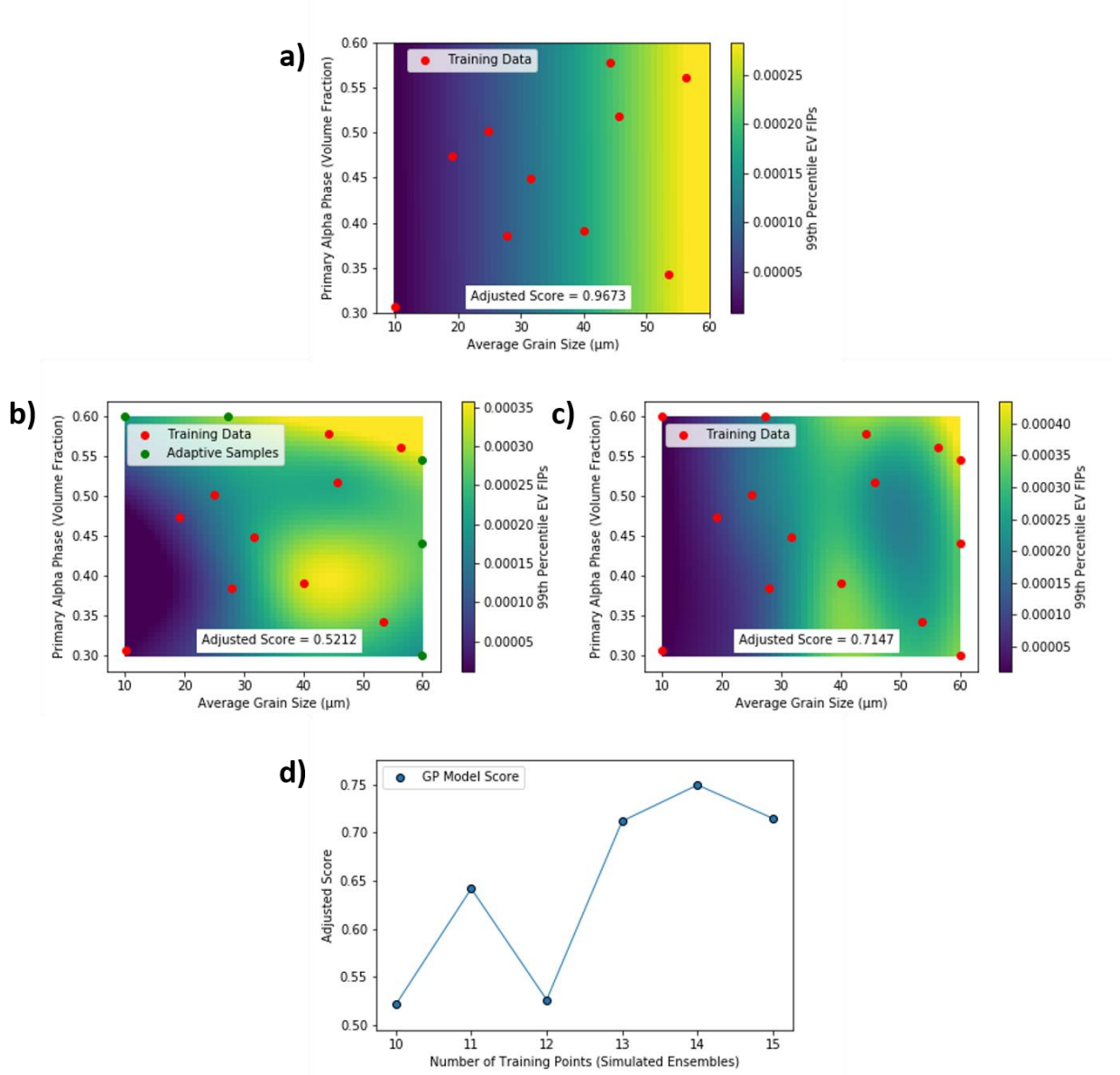

Figure 5.5. 2D surface plots of GP model predictions of 99th percentile predicted extreme value FIPs for random textured Ti64: (a) GP trained with less noisy data and (b) GP trained with more noisy data and next 5 adaptive samples shown in green, and (c) GP trained with more noisy data including additional training data chosen with adaptive sampling; (d) adjusted scores of GP models versus number of training data for noisy data models.

Next, the same process was carried out to train a GP model to predict FIP_{99} for al Ti64 having transverse textures. Figure 5.6 shows these results. Figure 5.6a and b show GP models trained using data with reduced noise. In this case the initial 10 training samples

shown in Figure 5.6a resulted in an adjusted score of 0.9369, slightly below the target performance of 0.95, thus adaptive sampling was used to train the model further, choosing three subsequent training samples based on points where GP uncertainty was the highest. Figure 5.6b shows the resulting GP model after the three adaptively sampled training data were added, and the final adjusted score was 0.9814.

Similar to the process shown above for random texture, a GP model was trained on noisy data to compare as a baseline and Figure 5.6c shows the model trained with 13 noisy training sample inputs resulted in a score of 0.7018. To provide a fair baseline comparison having comparable computational time to the well performing, less noisy data, five more training samples were added to the training set for the noisy training data using adaptive sampling. As expected, the performance improved marginally, but as shown in Figure 5.6d, with an adjusted score of 0.7644 the performance did not reach the target adjusted score of at least 0.95. Figure 5.6e shows the performance of the GP model trained on noisy data, versus the number of training samples used. We see that the performance again appears to have hit a ceiling well below the performance of the model trained using less noisy data.

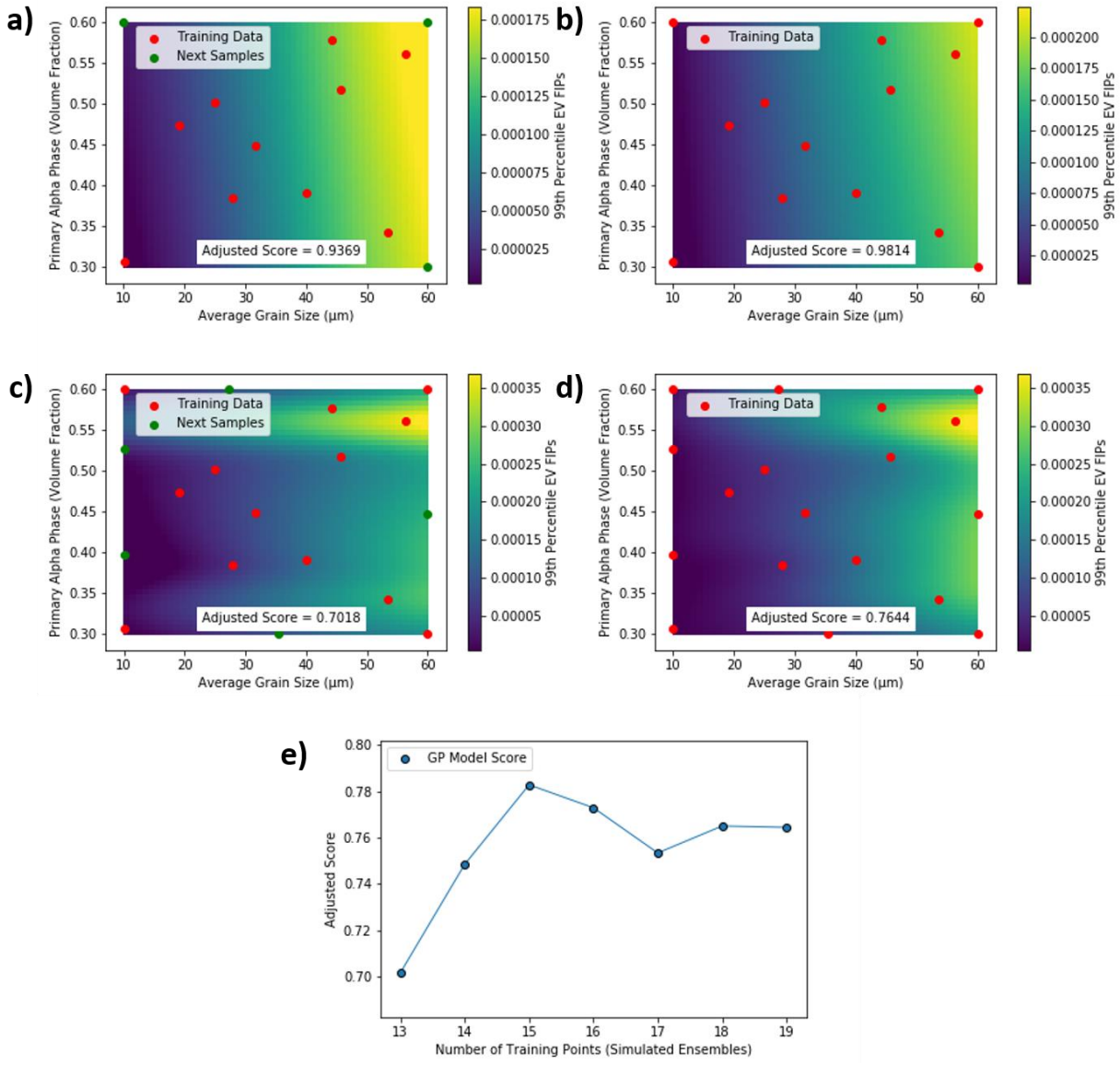

Figure 5.6. 2D surface plots of GP model predictions of 99th percentile extreme value FIPs for transverse textured Ti64: (a) GP model trained on data with initial less noisy dataset, (b) with additional adaptive sampling, and (c) with more noisy data, and (d) with additional training data chosen using adaptive sampling; (e) adjusted scores of GP models versus number of training data for noisy data models.

Lastly, GP models predicting yield strength were trained using the same input training samples. These training data were produced using CPFEM simulations. To attain yield strength a simple uniaxial tensile test was simulated to 1.2% strain and the 0.2% offset

yield strength was attained from the resulting macroscopic polycrystalline stress-strain data. Polycrystalline stress-strain data are far less noisy than extreme value FIP data; a SVE comprising 500 grains was sufficient to generate reproducible data for yield strength with noise of less than 0.1%, effectively serving as a RVE. Additional parameters for these simulations are shown in Table 5.1 The resulting trained GP models for each texture are shown in Figure 5.7 and both models performed well with the initial ten training samples, thus no further training data was needed. Additionally, modulus of elasticity was calculated from the macro stress-strain data for each sample. However, modulus of elasticity was insensitive to change in average grain size and volume fraction of primary alpha phase across the design space explored, thus it was unnecessary to train a surrogate model. The elastic stiffness for random and transverse textured Ti64 in this work were 124.4 GPa and 146.2 GPa, respectively.

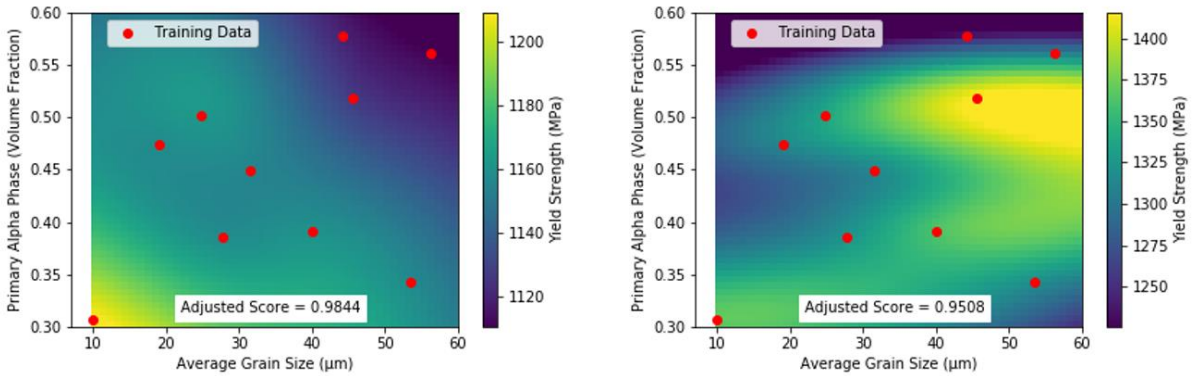

Figure 5.7. 2D surface plots of GP model predictions of yield strength for (left) random and (b) transverse textured Ti64.

5.3.4 Propagation of Aleatory Microstructure Statistic Uncertainty

Having sufficiently trained surrogate models to stand in for high fidelity CPFEM simulations, aleatory uncertainty in microstructure statistics can now be propagated through structure-property linkages in a robust manner. In this work, uncertainty in average grain size and volume fraction of primary alpha phase are characterized as normal distributions and uncertainty in these microstructure attributes is propagated to quantify statistical distributions showing uncertainty in FIP_{99} and yield strength of an Ti64 having nominal microstructure statistics as follows; 0.45 nominal volume fraction of primary alpha phase with a standard deviation of 0.0075, and 35μm nominal average grain size with a standard deviation in average grain size of 0.3μm. It is worth clarifying that the grain size from grain to grain in a given material still varies with a log normal distribution as described previously in Section 3.2. However, we are also imparting an uncertainty in the average value of all of the grains across a given batch of material. That is to say, if a material manufacturer produces a nominal Ti64 with an average grain size of 35μm, one batch of material from the manufacturer may still have a slightly different average grain size value than another. In this work the uncertainty associated with this difference from batch to batch of produced material was characterized using normally distributed data, and the standard deviations for average grain size [128, 129] and volume fraction of primary alpha phase [121, 130-132] are chosen to be realistic values based on literature. We note that the grain size distribution is still log-normal, however, here we added a normal distribution to the average value of the log normal distribution of grain sizes. Alternative distribution types could be used with no difficulty. However, the purpose of this work is simply to establish and demonstrate a workflow by which this aleatory uncertainty can be

robustly and reliably integrated using ICME. An original equipment manufacturer (OEM) could produce histograms of actual microstructure statistics measured from batch to batch of their produced material and replace the normal distributions used in this work with a different distribution type that is based on their particular data.

Figure 5.8 shows histograms of 10,000 samples taken from the normal distributions of each microstructure attribute, and a combined three dimensional histogram showing the entire distribution of microstructures associated with a nominal microstructure having the attributes described above. For the combined histogram 100,000 samples were drawn from the two dimensional uncertainty distribution of the input space.

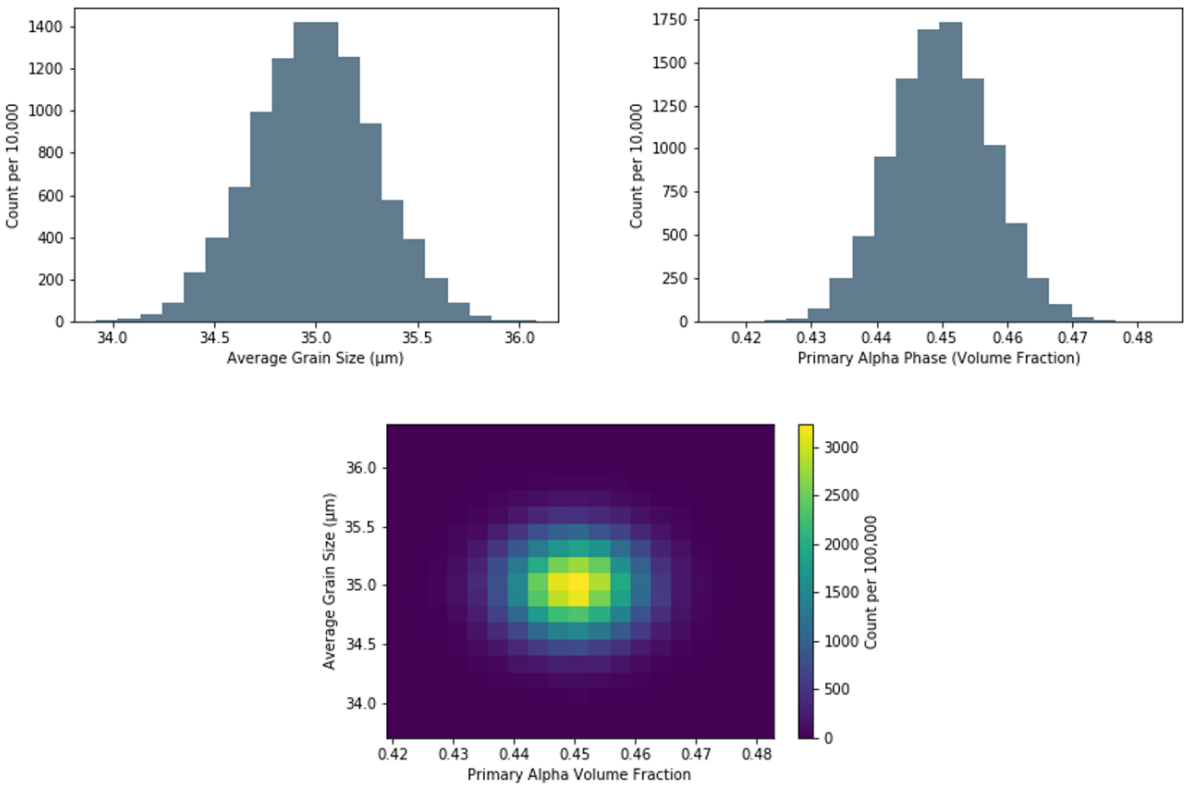

Figure 5.8. Normal distributions for (left) average grain size, (right) volume fraction of primary alpha phase, and (bottom) both combined for a typical Ti64 alloy.

This input uncertainty distribution of microstructure statistics was then propagated through SP linkages using the associated GP surrogate models to produce output distributions of predicted yield strength and FIP_{99} for Ti64 with both random texture and transverse texture subjected to the loading conditions described in Section 3.2. The resulting distributions of uncertainty in output properties are shown in Figure 5.9 and include both aleatory uncertainty resulting from microstructure statistics, and epistemic uncertainty resulting from GP model uncertainty, as calculated from the standard deviation of GP predictions. To incorporate both input dimensions as well as GP model uncertainty, the input space was sampled 10,000 times (a multiple of 100 for each input parameter to ensure a reasonable normal distribution) and at each of those 10,000 sample points, the GP model was sampled 100 times to get a distribution associated with the uncertainty in the GP predictions. This resulted in 1,000,000 samples per texture, for a total count of 2,000,000 samples shown in Figure 5.9.

It is clear from Figure 5.9 that the output distributions have different shapes. The transverse textured material has a much wider distribution of yield strength, which can be interpreted as a higher degree of uncertainty in yield strength. The transverse texture has a standard deviation of 10.56 MPa, compared with a standard deviation of 2.42 MPa from the random textured material. Conversely, the random textured material has a slightly higher uncertainty in predicted FIPs having a standard deviation of 5.82×10^{-6} compared with a standard deviation of 4.82×10^{-6} for the transverse textured material.

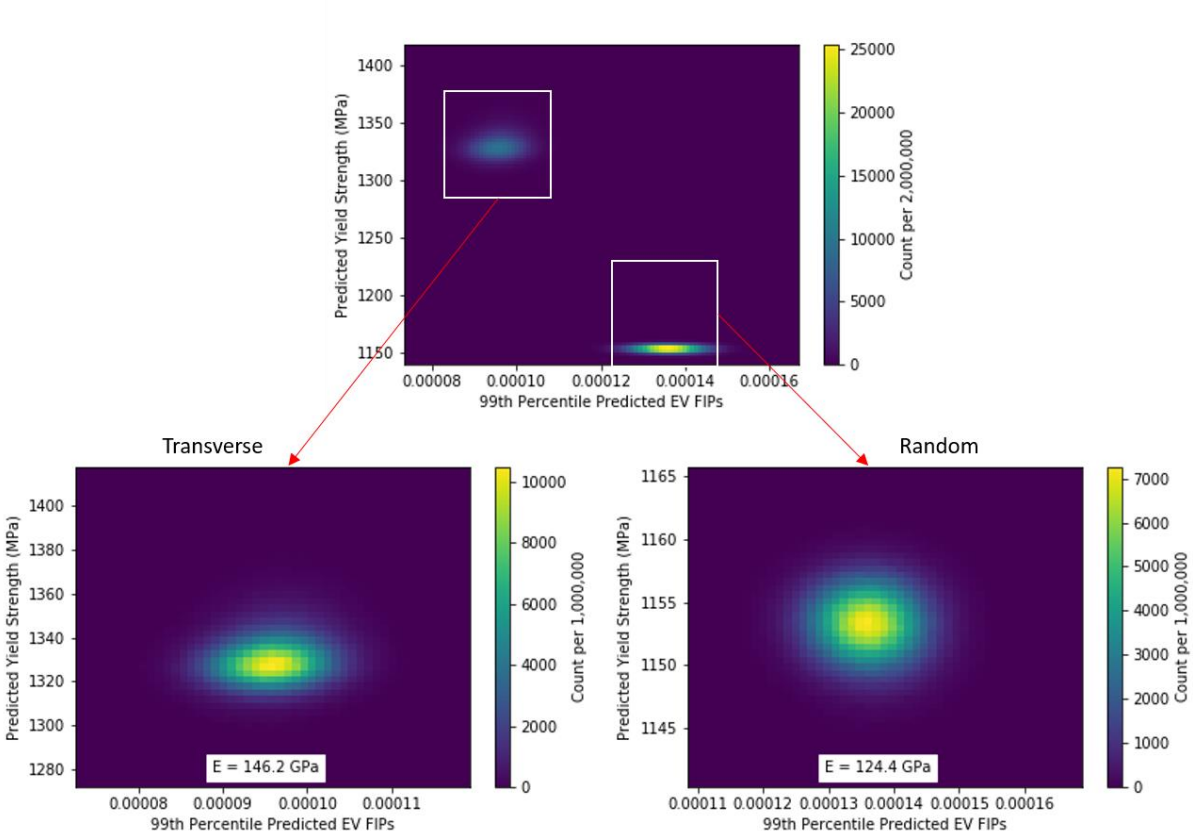

Figure 5.9. Output uncertainty distributions for predicted 99th percentile extreme value FIPs and predicted yield strength for sample Ti64 materials with (left) transverse texture and (right) random texture.

Finally, Figure 5.10 shows the full workflow that has been established to quantify and propagate uncertainty in microstructure attributes through SP linkages in turn quantifying uncertainty in properties of interest. Surrogate models were used to replace SP linkages for yield strength and fatigue life, the latter of which was quantified using extreme value FIPs as a surrogate measure of fatigue. Elastic moduli were calculated directly using CPFEM simulations that were used to train the yield strength surrogate model, as modulus of elasticity is constant across the grain size and phase information input space and only changes with the categorical crystallographic texture input. Using surrogate models, uncertainty in phase information, grain size, and spatial statistics were propagated to

quantify uncertainty in yield strength and predicted 99th percentile extreme value FIPs using 10,000 random samples from the input space in just 40 seconds of CPU time, representing eight orders of magnitude reduction in CPU time compared with the same number of samples propagated using the high fidelity CPFEM simulations. That is to say, it would take ~180 million times more computational time to propagate this uncertainty through the CPFEM model without the GP surrogate model. This was achieved by training models with between 10 to 13 samples, and it introduces 1.86% to 2.27% increase in epistemic uncertainty in the form of noise.

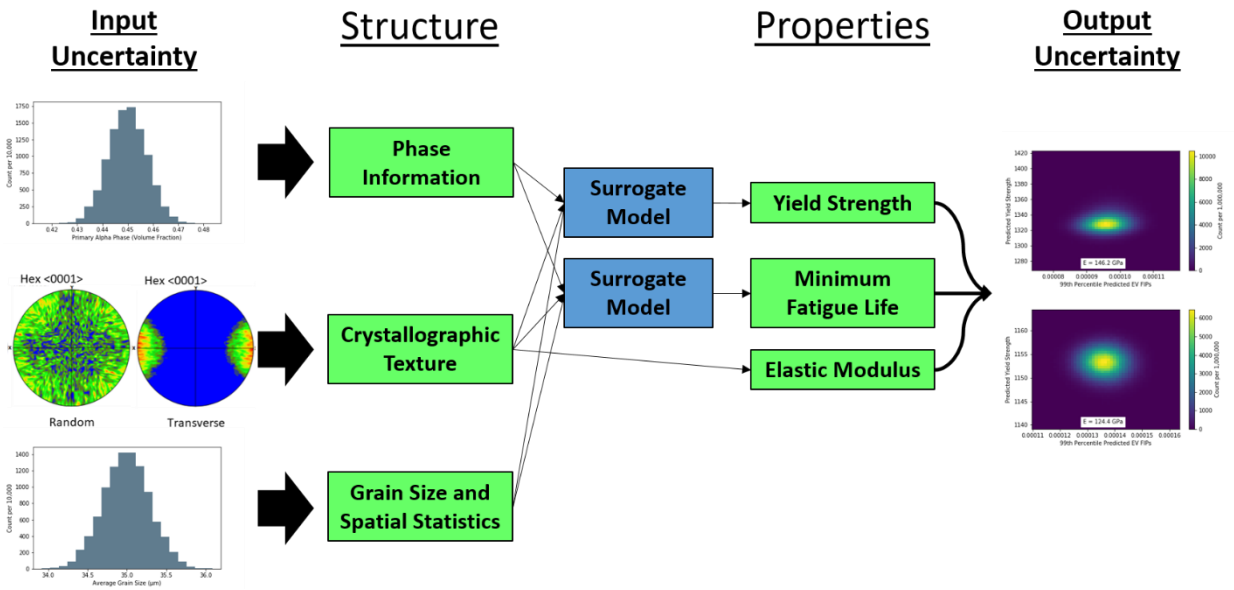

Figure 5.10. Schematic of uncertainty propagation workflow with Gaussian process surrogate models shown by blue boxes.

5.4 Chapter Summary

In this chapter it was shown that uncertainty in predicted extreme value FIPs can be greatly reduced by using properly selected ensemble size and thresholding FIPs. The

reduction of this uncertainty results in less noisy data that can greatly improve the quality of a GP regression model trained on the data, and thus allow for a reasonably reliable surrogate model to be achieving 95% accuracy or better with as few as 10 to 13 training samples. Using such a machine learning surrogate model, uncertainty can be rapidly propagated through PSPP linkages. In this chapter, the process of propagating uncertainty from structure to properties was demonstrated. Using the methodology established herein, and extending it to a full PSPP map, a material manufacturer could reliably and robustly predict uncertainty in performance of a part using their material, by understanding the uncertainty in their processing steps, and using computational models to predict performance from properties, properties from structure, and structure from processing.

Chapter 6: Uncertainty Informed Inductive Design Exploration Method Case Study: Robust Design of Ti64 Microstructure for Multiaxial Fatigue Loading

6.1 Modern Simulation-Informed Materials Design

Engineering design has historically relied on selecting materials from tabulated databases of properties. Over the past couple of decades, trends have moved toward concurrent design of material composition and microstructure together with the component/system level [133]. The traditional framework employed limited iteration due to dependence on costly and time-consuming physical experimentation. To improve this process, Olson [55] proposed a methodology based on an inductive approach that employs selected use of models that pursue deductive paths.

The bottom-up path is important to facilitate understanding the physics associated with PSP linkages. However, the top-down approach is essential to design of materials for specific sets of performance requirements. IDEM is a useful methodology that exploits Olson's concept by pursuing bottom-up mappings (either experimental or computational) to assess feasible or accessible structures and properties, followed by top-down searches to identify candidate solutions for multi-level robust design under uncertainty [48, 97, 134, 135]. IDEM also allows for an application specific materials optimization strategy [50].

Achieving desired performance usually requires tradeoff between conflicting goals since there is generally no clear optimal solution when one considers the effects of aleatory

and epistemic uncertainty. Therefore, a Pareto optimal solution is generally recommended when dealing with complex optimization problems under uncertainty [51].

6.2 Methodology

The methodology used for uncertainty quantification, inductive design exploration, multiaxial fatigue modeling are discussed in this section.

6.2.1 Uncertainty Quantification

As previously discussed at length throughout this dissertation, uncertainty in ICME workflows arises from several sources. In this chapter, with a focus on demonstrating a full uncertainty informed inductive design exploration method, types of uncertainty considered consists of the following:

- Aleatory uncertainty: herein the inherent uncertainty in the quantification of the various microstructure attributes is considered as aleatory uncertainty. Microstructure statistic uncertainty results from natural stochasticity in microstructures that emerges from the PS linkages. Once quantified, it must be propagated through SP linkages to determine uncertainty in output properties of interest. In this chapter the uncertainty associated with the average grain size and volume fraction of primary alpha phase are quantified and propagated to properties of interest; modulus of elasticity, yield strength, and extreme value FIPs. Each of these uncertainties is considered for materials with multiple different crystallographic textures that are subject to various loading conditions.

- Epistemic uncertainty: herein the model uncertainty resulting from “noise” in outputs of simulations using ensembles of finite size and number of SVEs as previously discussed in Chapter 4 and 5, as well as uncertainty introduced by using a GP regression model as a surrogate for the more costly, high fidelity CPFEM model, are both considered as sources of epistemic uncertainty. The noise is accounted for by studying the variance in across five samples for each texture and loading scenario and applying this variance to the GP surrogate model training data using a “WhiteNoise” kernel in the implementation of the GP regression model using Scikit Learn [136]. The GP regression uncertainty was accounted for using the built in standard deviation computation provided when predicting outputs using a GP regression model in Scikit Learn [136].

In this work, a Matérn kernel function was used to approximate the SP linkages. A Matérn kernel is a stationary kernel that is a generalization of the infinitely differentiable radial basis function kernel. The generalization allows for the user to determine the differentiability of the kernel function with a parameter ν. This controls the smoothness of the resulting function. Additionally, the Matérn kernel is parameterized by a length-scale parameter $l > 0$, which can be a scalar for isotropic variation or a vector with the same length as the input vector $\mathbf{x}$ for anisotropic variation. The Matérn kernel [32] was given previously by Equation **(5.2.1)**.

The GP surrogate models in this work were trained with ten data point training sets sampled from the microstructure space using LHS and validated using the LOOCV method. The LOOCV method was used to compare the quality of predictions from the surrogate model with predictions from the high fidelity ICME model.

6.2.2 Inductive Design Exploration Method

Historically, materials design and development has been approached with trial-and-error strategies along with empirical relationships and simple sequential design and deployment protocols. [2] This traditional framework employed limited iteration due to dependence on costly and time-consuming physical experimentation. To improve this process Olson [55] proposed a methodology based on an inductive, goal/means (top-down) approach that employs selected use of models that pursue deductive, cause and effect (bottom-up) paths.

The bottom-up path is important to facilitate understanding of the physics associated with PSP linkages. However, the top-down approach is essential to design of materials for specific sets of performance requirements. The Inductive Design Exploration Method (IDEM) is a useful methodology that exploits Olson's concept by pursuing bottom-up mappings (either experimental or computational) to assess feasible or accessible structures and properties, followed by top-down searches to identify candidate solutions for multi-level robust design under uncertainty [97]. IDEM also allows for an application specific materials optimization strategy [50].

Three robust solution schemes were introduced by Choi et al. [137] that seek to optimize performance by minimizing variance of different elements of the solution space: Type I robust solutions seek to minimize variation due to noise, type II robust solutions aim to minimize variation due to control factors, and type III robust solutions aim to minimize variation due to uncertainty inherent in the model [51]. These three robust solution schemes are illustrated alongside an optimal solution on a plot of design variable versus response in Figure 6.1.

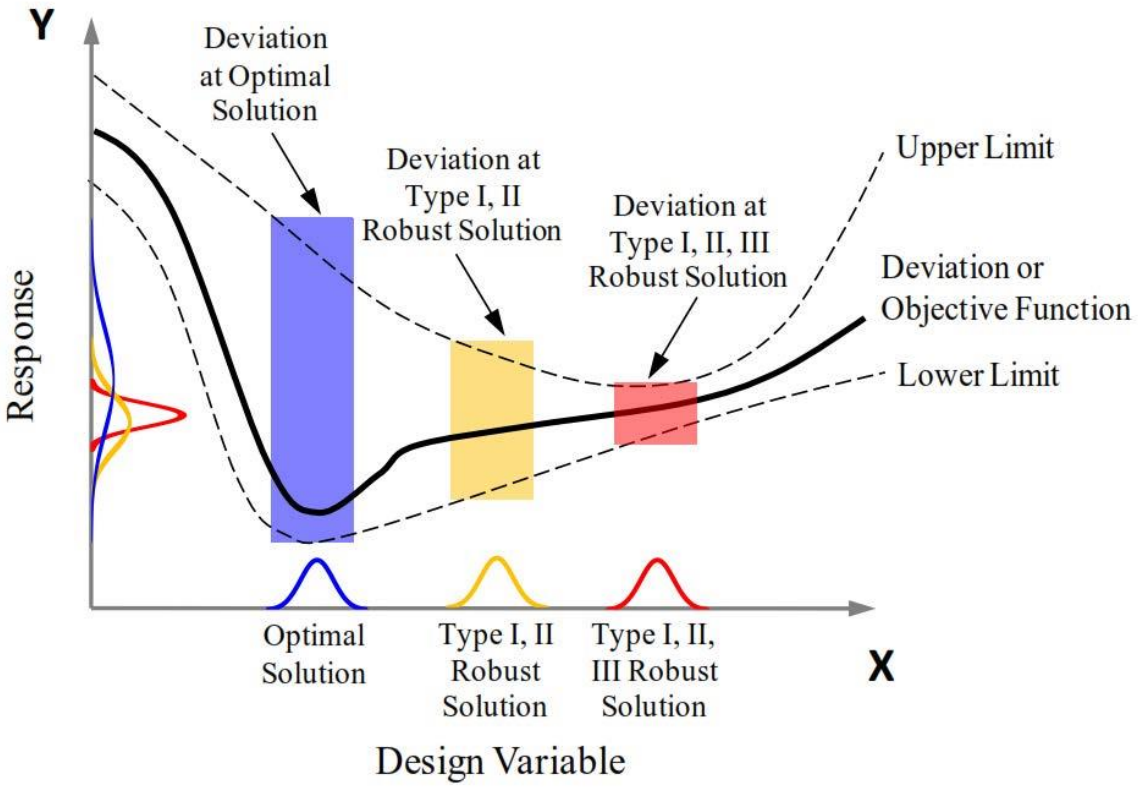

Figure 6.1. Comparison of optimal and robust solutions [51].

In the current work, the type I robust solution approach corresponds to minimizing the noise portion of the epistemic uncertainty resulting from the choice of size and number of SVEs in the simulated ensemble. The type II robust solutions approach corresponds to minimizing the variation in output properties of interests due to the aleatory uncertainty in microstructure attributes. While we cannot decrease aleatory uncertainty in a given microstructure, if we have multiple microstructures that satisfy our design constraints, we can choose the microstructure with the least associated aleatory uncertainty. Lastly, in the context of this work the type III robust solution should aim to minimize the uncertainty

associated with the GP regression model used as a surrogate to propagate uncertainty through structure property linkages.

IDEM uses models or other functional relationships to link levels in design such as process to structure and structure to properties. Feasible inputs at one level are determined by sampling and propagating through linkages to see what values satisfy the response requirements of the next level. The points that do not meet the design criteria are labeled infeasible. The border between the feasible and infeasible values can be defined iteratively and this constitutes the feasible input space for design [50].

The steps in IDEM are illustrated in Figure 6.2. Step 1 shows the deductive path where computational models, metamodels, or experiments are used for PS and SP mappings, establishing feasible regions of design space. A feasible region in process space is defined by the allowable ranges of process parameters (e.g. annealing time, annealing temperature, etc.) and the feasible region in structure space is established by propagating these parameters and their associated uncertainties to a multi-dimensional structure space made up of ranges of relevant microstructure parameters. Likewise, structure space and uncertainties are propagated to property space. Step 2 shows the inductive path where feasible solutions are explored based on ranged sets of performance requirements that intersect with the bottom-up mappings, as shown by the dashed ellipses within yellow regions. IDEM can determine the feasible structure space and in turn the associated regions of process parameter space by propagating through these design levels [97].

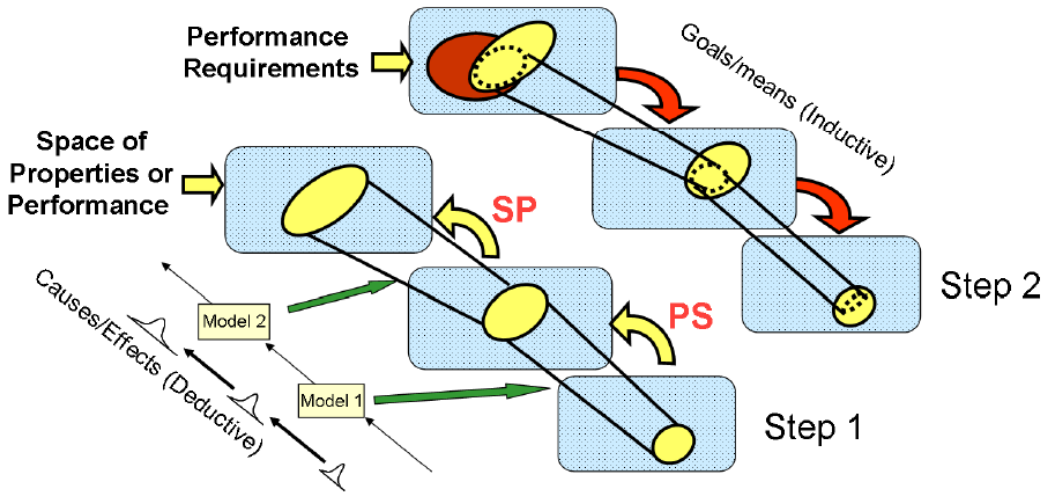

Figure 6.2. Inductive design exploration method [97].

IDEM is an attractive approach for robust design as it provides a computational workflow for generating robust design decision support in the face of uncertainty [48]. IDEM was implemented in an open source python computational environment called pyDEM [49]. The existing functionality of pyDEM is demonstrated in Figure 6.3 [50].

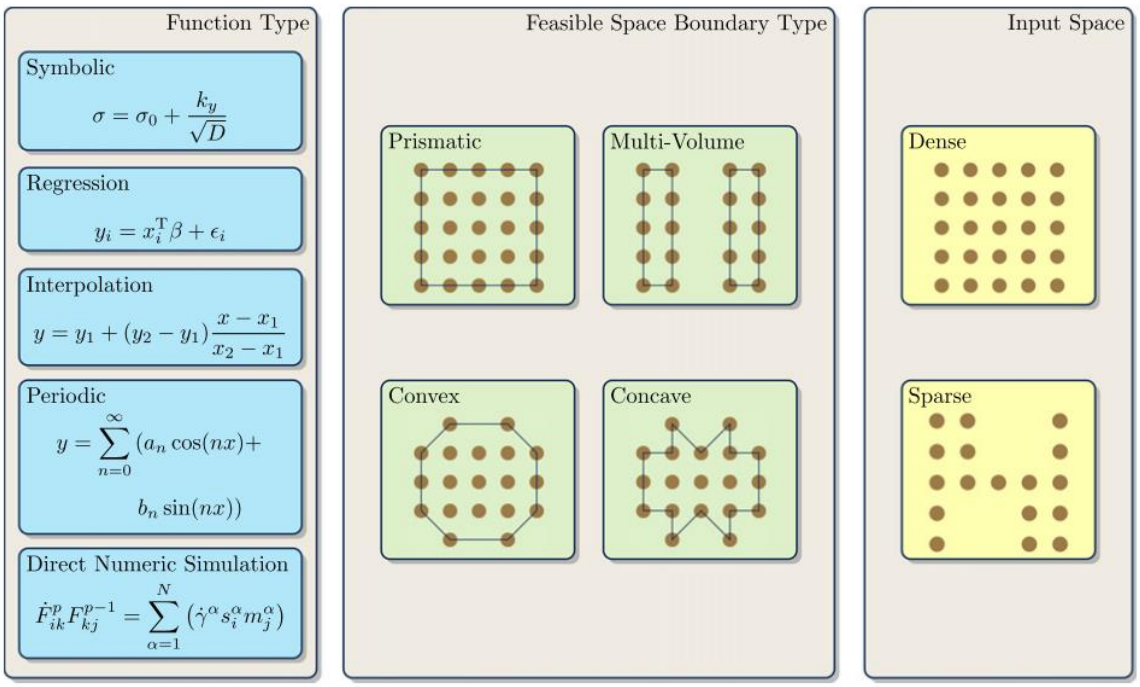

Figure 6.3. The various function types, feasible space boundary types, and input spaces available in pyDEM [50].

As shown in Figure 6.3, pyDEM relies on functional relationships between levels in the inductive exploration of design space. For example, these mappings can consist of experiments, data correlations, analytic theory forms, or as in the case of the present work, a surrogate model. GP regression surrogate models were used here to facilitate a more general approach to UQ in inductive design. Additionally, pyDEM allows for a rudimentary UQ process by which a standard error (e.g. +/- 2%) can be applied to input variables. In the current work, the UQP methodology described across Chapters 4 and 5 were applied to include state of the art UQ.

In the pyDEM [50] implementation of IDEM, hyperrectangle approximations of the boundaries of the mapped output region are constructed. For *m* output functions, an *m* × 3

matrix **Z** can be constructed to describe the nominal and bounding functions with components z_{ij} being the jth bounding function of the ith output dimension. The hyperrectangle can be constructed using Equation ***(6.2.1)***, where $\bar{x}$ corresponds to the nominal input and $\bar{y}$ corresponds to the nominal output.

$$\Delta y_i = \left| \max_j \left(z_{ij}(\bar{x}) + \left| \frac{dz_{ij}}{dx_k} \Delta x_k \right| \right) - \bar{y} \right|, \quad b_i > \bar{y}_i$$
$$\Delta y_i = \left| \min_j \left(z_{ij}(\bar{x}) + \left| \frac{dz_{ij}}{dx_k} \Delta x_k \right| \right) - \bar{y} \right|, \quad b_i \leq \bar{y}_i \qquad \textbf{(6.2.1)}$$

However, in the present work, in the interest of achieving a more robust quantification of uncertainty, a full distribution of predictions for each nominal input is computed using the surrogate model. Instead of simply having a nominal, maximum, and minimum value associated with each output, we now have a histogram of outputs generated from random samples of the distribution of uncertainty in the nominal inputs. Therefore, one can determine a nominal value, a maximum likelihood value, a maximum limit, and a minimum limit with whatever confidence interval is chosen for a given application.

The next step in IDEM is the computation of an error margin to determine if the output range for $\bar{x}$ satisfies the performance requirements, and thus may be considered a robust solution. The error margin must have a consistent threshold for accepting or rejecting a potential solution and be defined for all i dimensions in the input and output spaces as explained by Choi et al. [135]. Several error margins are currently implemented

in pyDEM. For this work, since uncertainty has been quantified robustly with full statistical distributions as previously described, the criteria was chosen based on the likelihood of satisfying design criteria. A robust solution is herein considered to be one with greater than 99% chance achieving the goals of the design, i.e., the entire statistical distribution lies within the desirable output space.

6.2.3 Multiaxial Fatigue

Experiments remain essential in providing decision support for materials design; however, the vast majority of fatigue experiments consider simplified uniaxial cyclic loading. In practice, materials are often subjected to multiaxial cyclic stress and strain conditions. To account for this, life prediction methods are generally calibrated to fatigue datasets that are often limited to a relatively small set of uniaxial experiments, sometimes with a bit of additional information regarding other stress states (e.g., cyclic torsion or tension-tension). Additionally, fatigue crack initiation experiments are complicated by a multitude of uncertainties caused by; specimen design, influence of strain gradients and stress concentrations, load frames, test configuration, test controllers, strain measurement, inference of damage, access to the surface, and definition of an initiated crack [138].

As a result of the relative lack of experimental data for multiaxial fatigue and the large degree of associated uncertainty, engineering components exposed to multiaxial fatigue loading conditions are often designed using conservative forms of multiaxial fatigue criteria and excessive safety factors. Thus, multiaxial fatigue is an area where an ICME methodology can be of great use to better understand and design for complicated loading conditions.

Over the years, several important investigations of different aspects of multiaxial fatigue on Ti64 have been carried out to understand; surface roughness effects [139], load sequence effects [140], and crack growth behavior [141]. Wu et al. [142] correlated experimental data of fatigue life of Ti64 under multiaxial fatigue conditions to the FS FIP, which is the basis for the FIP used in this work, as previously described. Building on these works, Stopka et al. [138] investigated extreme value FIP response of Ti64 under multiaxial cyclic loading in both bulk material and near surface with large strains corresponding the low cycle fatigue (LCF) conditions and small strains corresponding the HCF conditions. The results of this work suggested that there is not a significant difference in extreme value FIP response near surface versus in the bulk material for Ti64 exposed to high cycle multiaxial fatigue conditions. As such, in the present work, when studying Ti64 exposed to high cycle multiaxial fatigue conditions, periodic boundary conditions were used to simulate bulk material response rather than attempting to model surface effects that are likely negligible for this particular study.

6.3 Results and Discussion

In this Section, the results of this research are discussed. First, in Section 6.3.1, a PSPP map is presented for Ti64 and the structure-property linkages being modeled are highlighted. Additionally, a CPFEM model representing these structure-property linkages is explored across the microstructure space to establish the bottom up deductive model path. Second, in Section 6.3.2, GP regression models are trained on CPFEM simulation data for uniaxial and biaxial loading conditions across the entire microstructure space and uncertainty quantification and propagation through these surrogate models is discussed.

Lastly, in Section 6.3.3, UQ is integrate with IDEM and this new UQ informed IDEM framework is utilized to inductively design a Ti64 microstructure to satisfy specified design constraints for the properties of interest.

All CPFEM simulations used to compute FIPs in this work were based on the third full cycle of three loading cycles with a strain ratio of R=0 under strain-controlled strain cycling, periodic boundary conditions, at a strain amplitude of 0.6% in the 11 direction at a strain rate of 0.001 s^{-1} and a strain amplitude of 0.3% in the 22 direction at a strain rate of 0.0005 s^{-1}. Room temperature and quasistatic strain rate conditions were employed. For simulations referred to as "11" throughout the rest of this work, SVEs were strained uniaxially along the 11- or x-direction corresponding to the out of the page direction in the Hex <0001> pole figures in Figure 6.4. For simulations referred to as "22" throughout the rest of this work, SVEs were strained uniaxially along the 22- or y-direction corresponding to the up direction in the Hex <0001> pole figures in Figure 6.4. Biaxial fatigue loading conditions in this work refer to a strain ratio of 2:1 in the 11:22 loading directions. An example of one of the SVEs used for CPFEM simulations in this work is also shown in Figure 6.4. In the current work, only these two loading scenarios were explored, however, in the event that alternate strain states were of interest for design, the concept of a gamma plane could be utilized to translate between various loading scenario using iso-FIP contours as described by Stopka et al. [138].

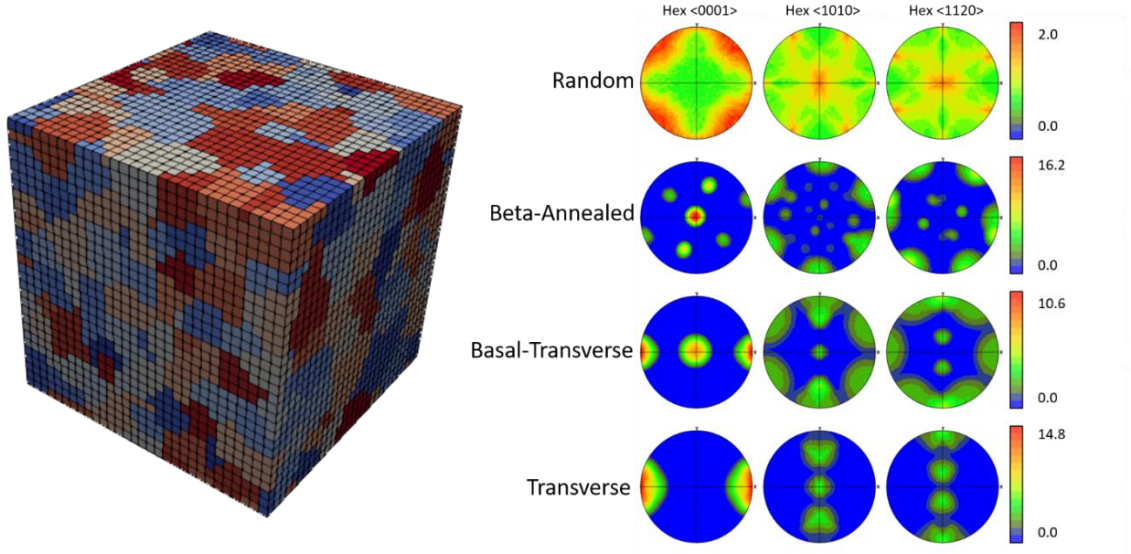

Figure 6.4. Examples of (left) SVE used in simulations for this work, and (right) pole figures of four crystallographic textures considered.

To represent statistical distributions of potential sites for fatigue crack formation, local quantities were computed at every integration point/element within the digital microstructures, after which volume averaging was performed to compute FIPs. No more than one FIP was taken from each grain to prevent localized characterization. Since the nonlocal sub-band averaging scheme for the FIP considers every combination of eight neighboring elements, only the top SBA FIP from each grain was considered in order to avoid duplicative counting of SBA FIPs that are directly adjacent within a given grain. The top SBA FIPs are then extracted to characterize an extreme value distribution. These were fit to a Fréchet extreme value distribution to enable comparison of trends in the extreme value distribution of FIPs among various SVE ensembles. Additional test parameters for all simulations in Section 6.3.1, 6.3.2, and 6.3.3 are given in Table 6.1.

Table 6.1. Computational simulation parameters.

Parameter	Value
# of applied cycles	3
Strain ratio	0
Temperature	300K
Elements per SVE	30^3
Boundary conditions	Periodic

6.3.1 Establishing a Deductive Structure-Property Path Using CPFEM Simulations for Ti64 Subjected to Multiaxial Fatigue

The first step toward uncertainty informed inductive design exploration is establishing the bottom up linkages of interest for the design exploration at hand. Here the Ti64 PSPP map that was first discussed in detail in Chapter 3 of this dissertation is relied on again. Here the same SP linkages as highlighted in Figure 5.1 are considered. In order to inductively design these microstructure attributes to achieve targeted sets of properties, the CPFEM model must be used to study the bottom-up cause-and-effect route through these structure-property linkages across the feasible microstructure space. Of course, due to the high computational cost, a limited number of simulations is selected to build a training set for a GP regression model that will then act as a reduced-order surrogate.

Here, as in previous chapters, phase information, crystallographic texture, and grain size and spatial statistics are quantified as; volume fraction of primary alpha phase (from 0.3 to 0.6), crystallographic texture (random, transverse, basal-transverse, or beta-annealed), and average grain size (from 10 μm to 60 μm), respectively.

The output properties of interest here are the modulus of elasticity, yield strength, and extreme value FIP response. The first two are quantified simply by applying simulated uniaxial strain to a large enough SVE that for all practical purposes serves as a RVE for stress-strain behavior for loading beyond macroscopic yield. In this case, a SVE containing 500 grains made up of 30x30x30 elements was loaded with strain-controlled computational uniaxial strain up to 1.6%. The elastic stiffness is taken as the slope of the linear region of the macroscopic stress-strain curve and the yield strength is determined using the 0.5% offset yield criteria [143]. The 0.5% offset yield criterion is implemented by plotting a line with a slope equaling the elastic stiffness and offsetting this line from the stress-strain curve by 0.005 along the positive x-direction (strain). The yield strength is determined by y-value (stress) at which this line intersects the stress-strain curve. Examples of macroscopic stress-strain curves used to calculate the elastic stiffness and yield strength in both loading directions with four different crystallographic textures for one particular microstructure attribute set (30 μm average grain size and 0.6 volume fraction of primary alpha phase) are shown in Figure 6.5. Here we can see that for the three materials with non-random crystallographic texture, there is a discernable difference between the yield strength and elastic stiffness in the 22-direction compared with those in the 11-direction. As expected, these materials are stiffer and stronger in the 11-direction. In particular, there is a significant reduction in elastic stiffness and yield strength in the 22-direction for transverse textured materials, going from the highest elastic stiffness in the 11-direction to the lowest elastic stiffness in the 22-direction.

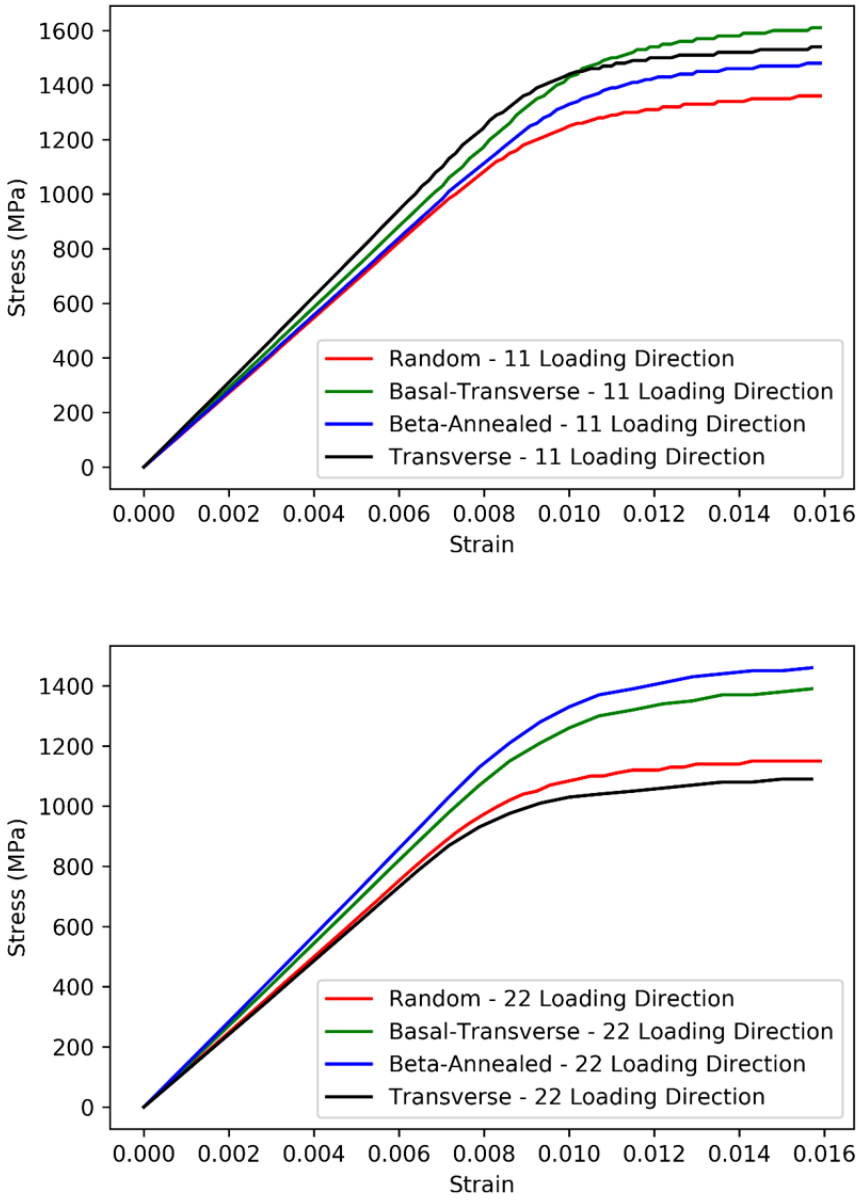

Figure 6.5. Stress-strain curves for all four textures considered with 0.60 volume fraction primary alpha phase and 30 micron average grain size for (top) 11-direction and (bottom) 22-direction.

The extreme value FIP response is first quantified by fitting the extreme value SBA FIPs from ensembles of SVEs to a Fréchet distribution as was described in Section 3.4, and then from there the 99th percentile of these Fréchet distributions can be used to compare

performance of different materials. It is this predicted 99th percentile extreme value FIP response that was estimated with the GP regression models and used as a design criterion for IDEM in the present work.

Figure 6.6 shows examples of extreme value SBA FIP responses fit to Fréchet distributions for both uniaxial and biaxial fatigue conditions with four different crystallographic textures for one particular microstructure attribute set (30 μm average grain size and 0.6 volume fraction of primary alpha phase). At the higher end of the FIP distributions the beta-annealed texture appears to perform better in both loading conditions for this particular microstructure. The predicted 99th percentile extreme value FIP response that is characterized in this work corresponds to a y-axis value of 4.6 in the plots shown in Figure 6.6. It is worth noting that in uniaxial loading the basal-transverse texture actually performs better at the lower end, for example at the 10th percentile corresponding to a y-axis value of -0.834. This indicates that fatigue performance of these two textures is comparable for these uniaxial loading condition, but a more conservative design approach would be to design for the lowest high end FIPs, which is why this work focuses on the 99th percentile. Additionally, the beta-annealed texture outperforms all other textures across the entire distribution for biaxial fatigue loading conditions with the particular microstructure attributes examined in these plots.

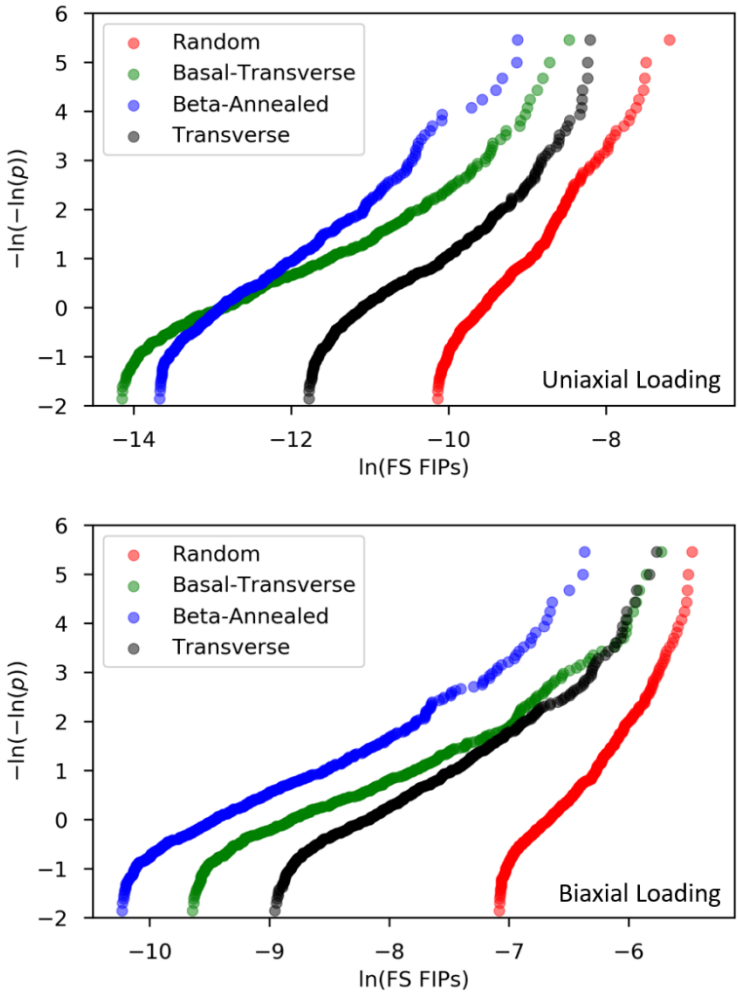

Figure 6.6. Extreme value SBA FIP distributions for all four textures considered with 0.60 volume fraction primary alpha phase and 30 □m average grain size plotted on a Fréchet plot for both (top) uniaxial loading and (bottom) biaxial loading.

Clearly, it can become quite complicated to interpret these results across multiple loading conditions, with four different crystallographic textures with three different quantities of interest (elastic stiffness, yield strength, and 99th percentile FIP performance), particularly when a large feasible microstructure space is considered, in this case adding two more dimensions to the problem. Figure 6.7 shows a summary of all of the properties of interest for the one particular example microstructure that has been examined in this

section. By examining these results, one could ascertain that either the beta-annealed or basal-transverse textures are likely the best option for this particular example microstructure. However, one could not say with any degree of certainty which would be a more robust solution in the face of epistemic and aleatory uncertainty. Thus, it is necessary to develop surrogate models facilitating uncertainty quantification and propagation to determine a robust design solution.

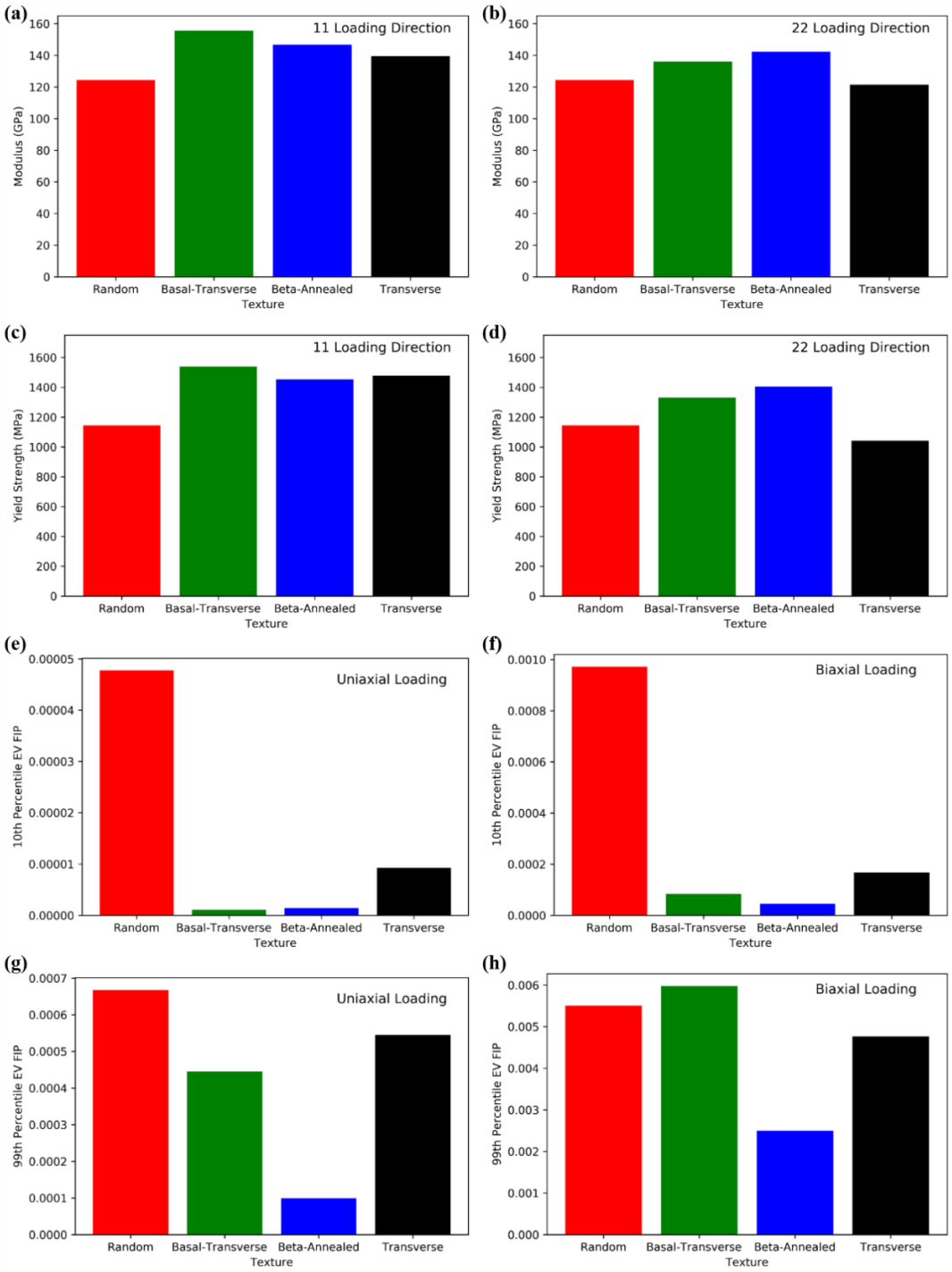

Figure 6.7. Bar graphs showing the properties of interest for all four crystallographic textures; (a) elastic stiffness for the 11-direction, (b) elastic stiffness for the 22-direction, (c) yield strength for the 11-direction, (d) yield strength for the 22-direction, (e) 10^{th} percentile extreme value FIPs for uniaxial loading conditions, (f) 10^{th} percentile extreme value FIPs for biaxial loading conditions, (g) 99^{th} percentile extreme value FIPs for uniaxial loading conditions, and (h) 99^{th} percentile extreme value FIPs for biaxial loading conditions.

6.3.2 Training Gaussian Process Regression Models for Uncertainty Propagation through Structure-Property Linkages

The first step in training surrogate models is to establish a reliable dataset. LHS can be used to ensure a diverse training set across the entire input space of interest. However, it is also necessary to quantify the epistemic uncertainty, in the form of noise, and reduce it to a level that facilitates high quality model regression. Following the methodology described in Section 5.3 of this dissertation, and using equations ***(5.3.1)*** and ***(5.3.2)*** the LOOCV approach was implemented to quantify the noise in predicted 99^{th} percentile extreme value FIPs for each loading conditions and four all four crystallographic textures, and the size and number of SVEs in an ensemble were selected to limit this noise. Ultimately, ensembles of 40 SVEs and 400 grains per SVE were used to limit noise in simulations for materials with random, transverse, basal-transverse, and beta-annealed crystallographic textures to the levels shown in Table 6.2. Larger ensembles were required in this section as compared with Chapter 5 to reduce noise to a manageable level because of the different loading conditions as well as the consideration of the basal-transverse, which resulted in the largest level of noise (19.2% for basal-transverse texture in biaxial loading).

Table 6.2. Noise in predicted 99th percentile extreme value FIPs with chosen ensemble.

Texture	Uniaxial Noise	Biaxial Noise
Random	10.8%	6.95%
Transverse	18.44%	11.15%
Basal-Transverse	15.3%	19.2%
Beta-Annealed	10.55%	8.83%

Having reduced noise to an acceptable level, a LHS strategy was used to sample from the two continuous inputs; average grain size, and volume fraction of primary alpha phase. Ten samples were taken from the input space for each texture. To generate training data for the GP surrogate models predicting 99^{th} percentile extreme value FIPs, the same HCF loading conditions as described previously in Section 5.3 were used and the ensembles for each training point consisted of 40 SVEs and 400 grains per SVE. The extreme value distributions of SBA FIPs were characterized using the top 400 FIPs from the sub group of extreme value FIPs as described previously in Section 5.3.2.

The GP surrogate model was trained using a linear combination of a Matérn kernel and a white noise kernel, the latter of which was included to capture the noise in the training data. The resulting GP models for each texture consist of two input dimensions (average grain size, and volume fraction of primary alpha phase) and two outputs (predicted 99^{th} percentile extreme value FIPs, and standard deviation in the predicted values).

The trained surrogate models for all four crystallographic textures and both uniaxial and biaxial fatigue loading conditions are shown in Figure 6.8. The ten training data sampled using LHS are shown in red in each of the plots. The adjusted performance metric shown on each plot is a measure of how well the surrogate model predicts the output property of interest, relative to the performance of the high fidelity CPFEM model simulations with noise reduced. This was calculated using a LOOCV technique as previously described in Section 5.3.3. As shown by both the noise values in Table 6.2 and the adjusted score values in Figure 6.8, there is less uncertainty associated with modeling the random and beta-annealed textures than there is with the transverse and basal-transverse textures. This is an important factor in determining a robust design solution. If

two candidate microstructures offer similar nominal performance, the microstructure for which there is less uncertainty in output properties will provide a more robust solution.

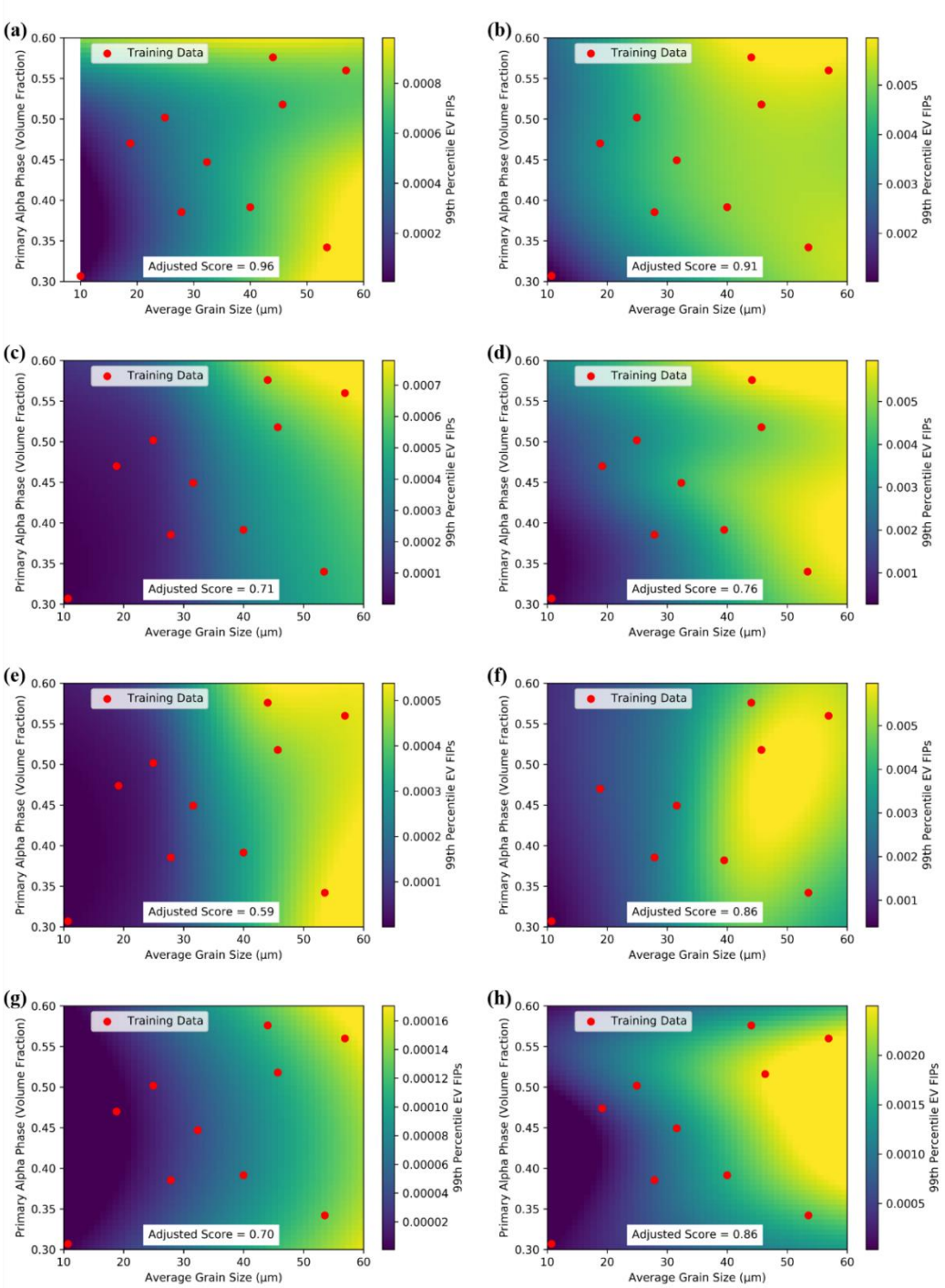

Figure 6.8. Gaussian process regression models for predicting 99th percentile extreme value FIPs for each crystallographic texture and loading scenario across entire microstructure attribute space considered with adjusted LOOCV scores labeled; (a) random texture uniaxial loading, (b) random texture biaxial loading, (c) transverse texture uniaxial loading, (d) transverse texture biaxial loading, (e) basal-transverse texture uniaxial loading, (f) basal-transverse texture biaxial loading, (g) beta-annealed texture uniaxial loading, and (h) beta-annealed texture biaxial loading.

Having trained GP regression models to act as reduced-order surrogate models for materials across the entire feasible space with both loading scenarios, it is now possible to propagate combined aleatory and epistemic uncertainty to the output properties of interest. Figure 6.9 shows an example of a typical distribution of microstructure attributes in this design space being propagated to an output distribution of predicted 99th percentile extreme value FIPs using a GP regression model. Here, the nominal microstructure attributes are a random texture, an average grain size of 40 μm, and a primary alpha phase volume fraction of 0.55. The nominal predicted 99th percentile extreme value FIP value is 0.0019, however there is range of about 0.0016 to 0.0022 covered by the output distribution. Similarly, every point in the entire feasible microstructure space has its own associated uncertainty distribution that can be propagated to property space using this approach.

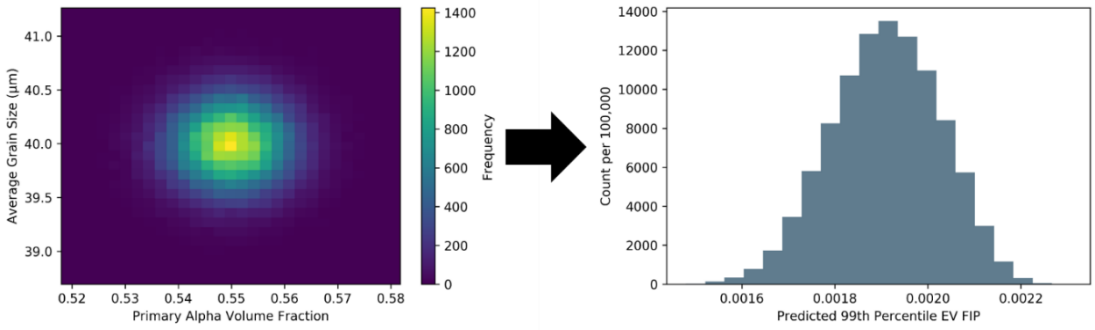

Figure 6.9. Example of distribution of aleatory microstructure statistic uncertainty and the associated uncertainty distribution in predicted 99th percentile extreme value FIP response for random texture with uniaxial loading conditions.

6.3.3 Uncertainty Informed Inductive Design of Ti64 Microstructure for Multiaxial Fatigue Conditions

Now that a reduced order surrogate model has been established to allow rapid exploration of properties across the entire feasible microstructure space with uncertainty quantification, an inductive design exploration case study can be carried out. For this case study the design criteria were set as; a yield strength value greater than 1350 MPa in the 11-direction and 675 MPa in the 22 direction, an elastic stiffness of 135 GPa in the 11-direction and 67.5 GPa in the 22-direction, and predicted 99^{th} percentile extreme value FIPs of less than 0.001 in both loading scenarios. These design criteria were set as representative of a high strength, high stiffness, and fatigue resistant Ti64 microstructure that an engineer might design for a jet engine turbine blade. The specific target values of each were selected somewhat arbitrarily to represent rough estimates of realistic properties of interest for the mentioned application. However, the purpose of the present work is not to design a Ti64 microstructure for a specific application, but rather to demonstrate the framework for uncertainty informed IDEM that could be used to support such a robust design of a microstructure.

A two-dimensional version of the IDEM process for the present case study is illustrated in the schematic shown in Figure 6.10. The entire microstructure attribute space and property space are shown by the large gridded squares. Within those squares the smaller orange rectangle and oval represent the feasible space for Ti64. That is, the orange rectangle shows the ranges of Ti64 microstructures that are physically possible to realize through processing and the orange oval shows the corresponding properties. The red areas show the desirable space for this design. An engineer designing a jet engine turbine blade

would want to minimize FIPs (maximizing high cycle fatigue resistance) and maximize yield strength. Thus, the red area in the property space corresponds to those goals, while the red area in the structure space corresponds to the microstructure attributes that might provide such properties. Lastly, the green space is the overlap of the feasible space (orange) and desirable space (red). It is this green space where an engineer would aim for in their microstructure design.

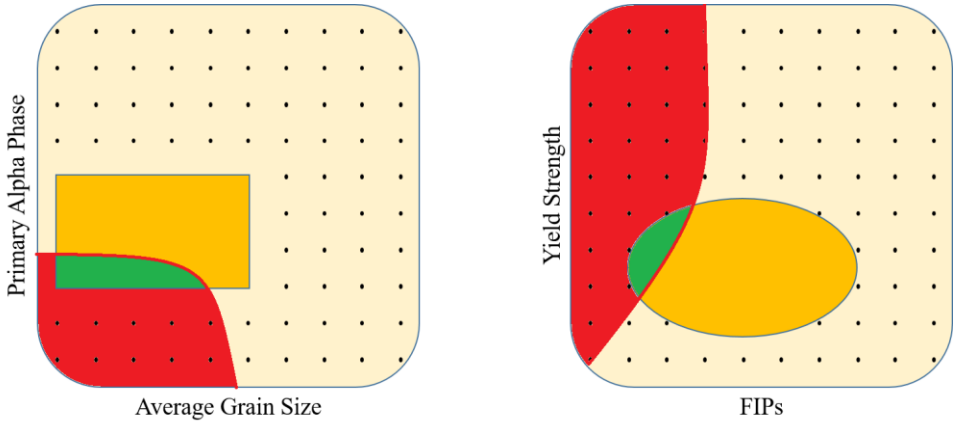

Figure 6.10. Diagram illustrating outcomes of the inductive design process; (left) microstructure space includes achievable microstructure attributes in orange, desirable microstructure attributes in red, and the overlap of the two in green, and (right) the property space with corresponding achievable properties in orange, desirable properties in red, and the overlap in green.

Using the GP regression reduced order surrogate models established in Section 6.3.2 the feasible microstructure space was gridded from 0.3 to 0.6 volume fraction of primary alpha phase in increments of 0.01, and from 10 μm to 60 μm average grain size in increments of 1 μm providing a gridded space of 1581 nominal microstructures per crystallographic texture. First, for the sake of comparison, GP models were used to predict all of the output properties of interest (predicted 99^{th} percentile extreme value FIPs, elastic

stiffness, and yield strength) without any uncertainty quantification. The results of all of the GP model predictions across the entire microstructure space were screened against the design criteria for output properties of interest. Figure 6.11 shows the screened results without uncertainty quantification considered. The yellow areas represent viable microstructures, these are microstructures that, based on the nominal GP predictions, satisfy all of the design criteria. Here we can see that all four textures provide some candidate microstructures that satisfy all the design constraints, with beta-annealed texture having the widest range of viable microstructure attributes.

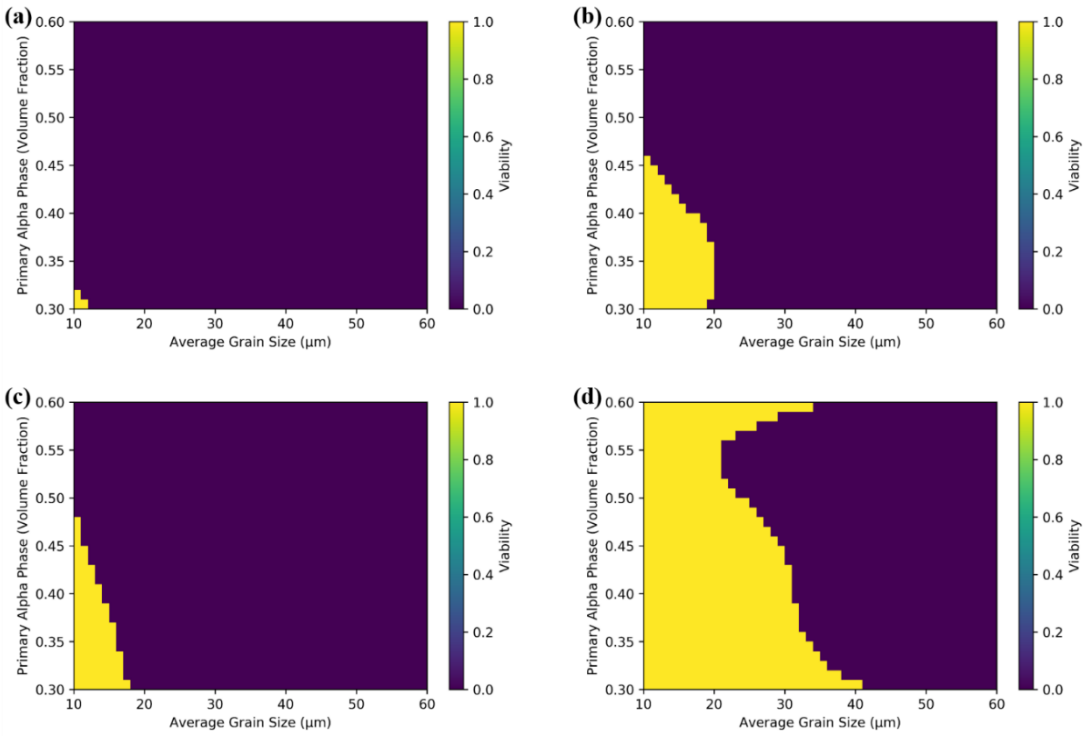

Figure 6.11. Results of inductive design exploration using no uncertainty quantification across achievable microstructure space for all four crystallographic textures with yellow corresponding to viable microstructures that satisfy design constraints and purple corresponding to non-viable microstructures; (a) random texture, (b) transverse texture, (c) basal-transverse texture, and (d) beta-annealed texture.

In order to incorporate the UQ framework that has been established in this dissertation, the same process is taken to predict nominal microstructures, however, for each set of nominal microstructure attributes a distribution of the uncertainty in microstructure attributes is generated as shown previously in Figure 6.9. Here, 1,000 sample microstructures are generated from a Gaussian distribution of average grain size and volume fraction of primary alpha phase for each of the 1581 nominal microstructures in the feasible microstructure space. Each output property of interest as well as the standard deviation of the GP regression model uncertainty (accounting for both the uncertainty introduced by the use of the surrogate model as well as the noise in the training data generated using CPFEM simulations) are computed using the GP regression model with all 1,581,000 microstructure attribute combinations. Next, distributions of output properties for each of the 1,581,000 microstructure attribute combinations are generated using a Gaussian distribution with the GP prediction as the mean value and the GP standard deviation prediction as the standard deviation. Essentially an outer loop of 1,000 samples accounts for microstructure attribute uncertainty and an inner loop of 100 samples accounts for GP model uncertainty with each microstructure attribute set. This process is carried out at all 1,581 nominal microstructure attribute combinations across the feasible design space and this results in 158,100,000 samples, made up of 1,581 sets of 100,000 samples that make up a distribution of uncertainty in output properties for a given nominal set of microstructure attributes. Each of these distributions are then queried to determine what percentage of samples for a given uncertainty distribution of output properties satisfy all of the design constraints. Each of the 1,581 nominal microstructures in the gridded feasible microstructure space are then assigned a robustness score from 0.0 to 1.0 computed based

on the percentage likelihood that the output properties for that microstructure will satisfy the design constraints. This whole process takes ~31 seconds of CPU time and was repeated for all four crystallographic textures and the results are shown in Figure 6.12. Microstructures having a robustness score of 1.0 are considered robust solutions as all 100,000 samples making up the output property uncertainty distribution for those microstructures satisfy all of the design constraints. This methodology also provides precise likelihood predictions between 0.0 and 1.0 allowing an engineer to decide their own desired confidence interval for robustness. In the present work only microstructures that had a perfect 1.0 score were considered robust.

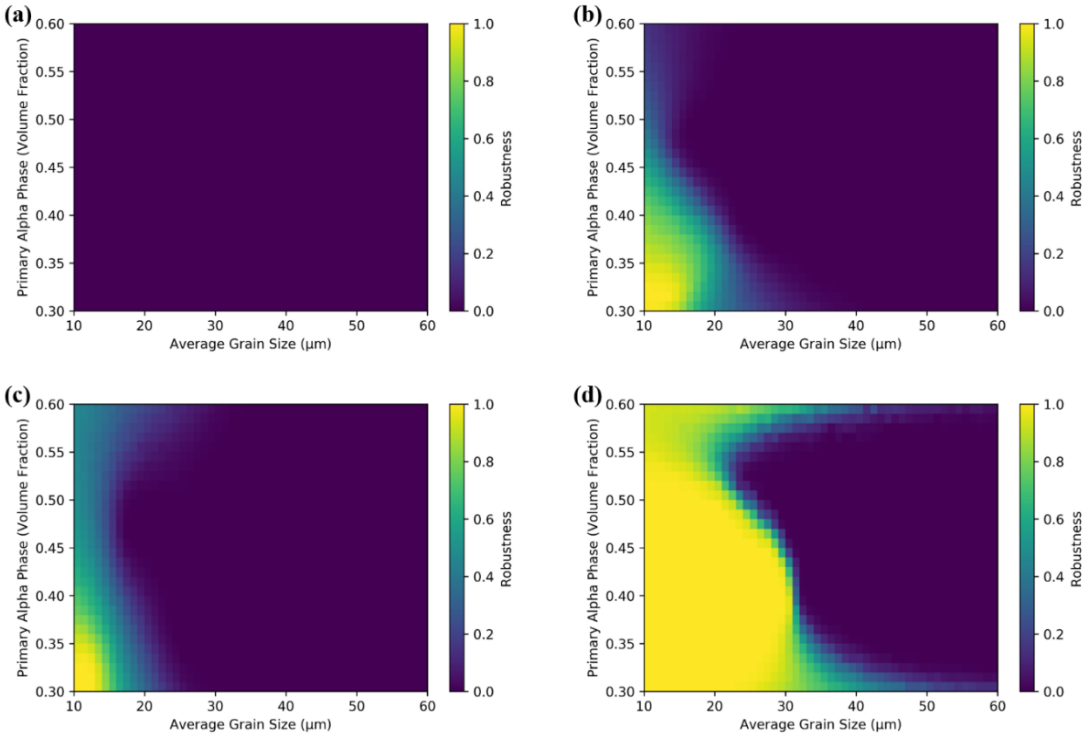

Figure 6.12. Results of uncertainty informed inductive design exploration across achievable microstructure space for all four crystallographic texture. The color scale shows the level of robustness of each microstructure with 0.0 meaning there is no chance that it will satisfy the design constraints and 1.0 meaning that there is greater than 99% likelihood that it will satisfy the design constraints; (a) random texture, (b) transverse texture, (c) basal-transverse texture, and (d) beta-annealed texture.

It is illuminating to compare the results of the inductive design exploration both with and without UQ to demonstrate the value added by considering uncertainty. Figure 6.13 shows both the fully robust solutions in yellow, and the solutions that would be considered nominally viable without considering uncertainty in teal. Clearly, if one does not consider uncertainty in this problem there are a great deal of seemingly viable microstructures that they might select that in fact will fail to satisfy the design constraint some fraction of the time. Additionally, by examining Figure 6.13, it can be seen that even though there is a larger number of viable solutions with a transverse texture (Figure 6.13b)

than there are with the basal-transverse texture (Figure 6.13c), there are actual no robust microstructure solutions having transverse texture, while there are a small number of robust microstructure solutions with the basal-transverse texture.

Finally, the beta-annealed texture (Figure 6.13d) provides the largest range of robust microstructure solutions. It is interesting to observe the shape of the viable space relative to the robust space. By examining the viable space in the beta-annealed plot one might conclude that microstructures at the ends of the limits of volume fraction of primary alpha phase provide the best solution. Conversely, by examining the robust space, one would conclude that it is better to have a more moderate volume fraction of primary alpha phase. The reason for this apparent discrepancy is that GP regression models, like all regression models, can interpolate between training data with a higher degree of certainty than they can extrapolate beyond the limits of the training data. As a result of this, while the model predicts that there are viable solutions near the limits of microstructures space, there is a higher degree of certainty in the model predictions further from those bounds. Thus, by incorporating uncertainty quantification it is possible to eliminate solutions with lower likelihood of successfully satisfying the design criteria and focus on the most promising, robust microstructure solutions.

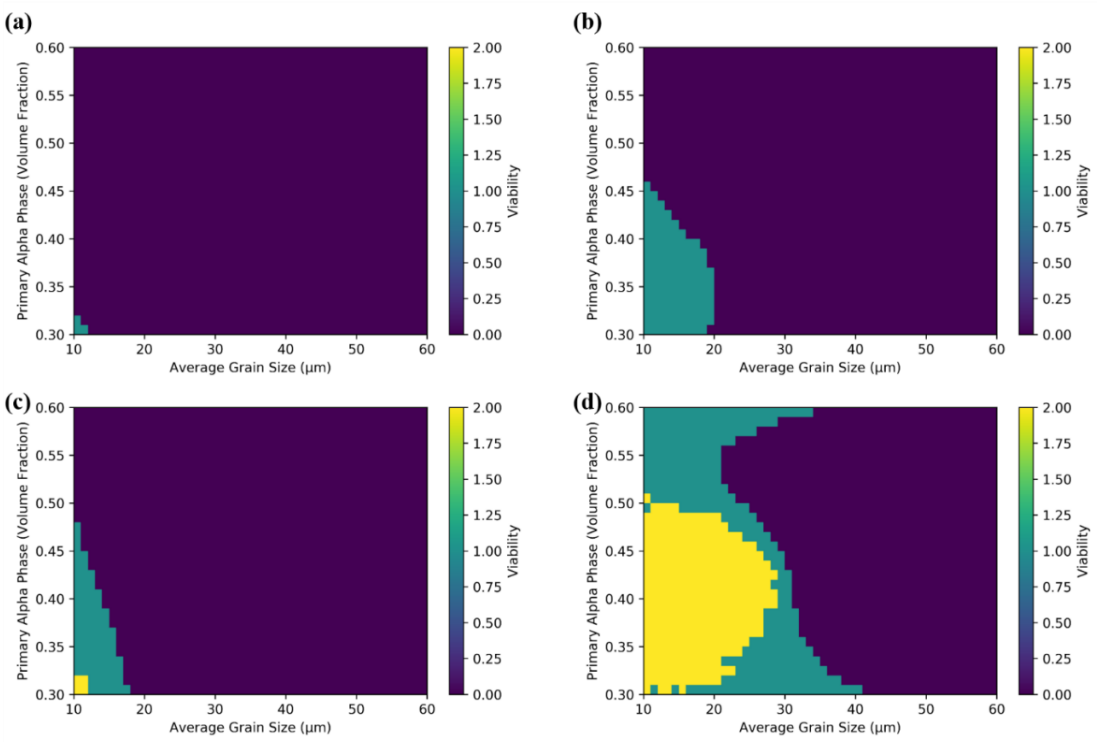

Figure 6.13. Comparison of results from inductive design exploration with and without uncertainty quantification. Color scale shows robust microstructures in yellow (corresponding to a score of 2.0) , microstructures that appear nominally viable but are not robust in teal (score of 1.0), and microstructures that are neither robust nor nominally viable in purple (score of 0.0); (a) random texture, (b) transverse texture, (c) basal-transverse texture, (d) beta-annealed texture.

In the current work the entire feasible microstructure space was enumerated and the GP model was utilized to predict uncertainty distributions for output properties of interest at all 1581 nominal microstructure attribute combinations for both uniaxial and biaxial loading, and for all four crystallographic textures of interest. This “brute-force” approach to design exploration with the GP surrogate model was used because, once the surrogate model was trained, it was very computational inexpensive to enumerate the entire design space, at approximately 30 seconds per texture and loading scenario, or a total of approximately four minutes for both loading scenarios and all four crystallographic

textures on a single CPU. However, in the event that the design space is significantly larger than the example shown in the present work, and it becomes undesirable to enumerate the entire design space, the computational cost of this workflow could be reduced by using an analytical approach to evaluating the uncertainty in the GP model rather than random sampling from a distribution generated from the mean and variance of the GP predictions. Further, the methodology laid out in this chapter could be used to coarsely determine the robust space and then a finer grid could be used near the boundaries of the robust space to iteratively refine the boundaries in a computationally efficient manner.

Of course, once a robust solution space is defined, a design engineer can then define an objective function assigning relative value to each of the output properties of interest and determine their optimal solution within the robust space. For the purposes of a formal optimization of that kind, the GP adaptive sampling strategy can be revised to focus on sampling candidate microstructures with the greatest likelihood of improvement over any of the existing samples, rather than the uncertainty driven adaptive sampling strategy implemented above, which is more appropriate in the design exploration stage. However, such an objective function would depend on the specific application and is beyond the scope of this work.

6.4 Chapter Summary

In this chapter, a framework is presented that facilitates the integration of the uncertainty quantification methodology from previous chapters with the inductive design exploration method. The uncertainty informed IDEM is then utilized to conduct robust

optimization of a Ti64 microstructure for a multiaxial fatigue critical application. The IDEM framework provided a way to constrain the input space and define the robustness and viability criterion. To achieve this, structure-property linkages were defined and a CPFEM model was used to simulate the effects of varying microstructure on the material properties considering both uniaxial and biaxial fatigue conditions. GP regression models were trained on the results of CPFEM simulations to provide reduced-order surrogate models facilitating uncertainty propagation through structure-property linkages. These surrogate models were used for rapid uncertainty-informed design exploration across the entire feasible microstructure space and all possible microstructures were evaluated to find microstructure candidates that provide a robust solution to a designated set of design criteria. Ultimately, a number of microstructures having both the basal-transverse and beta-annealed crystallographic textures were identified as candidate robust Pareto solutions, subject to designer preference.

Chapter 7: Conclusions and Recommendations

This chapter provides context for the scientific and technological contributions of this dissertation. The advances put forth by each section are summarized with respect to the overarching goal of the work. Additionally, perspectives gained over the course of this work on potentially fruitful directions for future research are summarized.

7.1 Overview of Contributions

The work contained in this dissertation has identified challenges in establishing uncertainty informed integrated computational materials engineering (ICME) workflows aimed at design and optimization of fatigue critical metallic alloys. The grand challenge of creating a materials design infrastructure that allows engineers to customize materials for specific applications requires that these advanced computational modeling tools comprising ICME provide useful decision support – hence, the uncertainty of information emerging from these tools must be quantified. Therefore, uncertainty quantification (UQ) and propagation is pivotal to the development of useful workflows that can facilitate design of materials using computational modeling. In this work, several key gaps in UQ for ICME were addressed.

Chapter 3 focused on understanding the material systems at hand. The complex interplay between processing, structure, properties, and performance of the Ti64 and Al7075-T6 material systems was captured in process-structure-property-performance (PSPP) maps and the sensitivity of key properties for fatigue critical applications was

explored through a global sensitivity analysis using the crystal plasticity finite element method (CPFEM) models. Additionally, importance sampling techniques were employed to coarsely propagate uncertainty distributions from microstructure attributes to properties. This acted as a first pass at uncertainty quantification and propagation that demonstrated the value in propagating distributions through structure-property linkages to gain insight on property distributions for design. However, due to the large computational expense of the high fidelity CPFEM model, it was clear from the results of this study that some form of reduced-order surrogate model would be needed to efficiently propagated uncertainty distributions.

Next, in Chapter 4, epistemic model form and model parameter uncertainty for the CPFEM model were addressed. While all sources of uncertainty are complicated and difficult to strictly categorize, it is useful in practice to differentiate between the inherent, irreducible aleatory uncertainties and epistemic uncertainties that can be reduced by increasing knowledge of the system. Quantifying each form of uncertainty is a significant challenge in itself and thus an entire chapter was dedicated to handling epistemic uncertainty. The model form uncertainty addressed in the context of the CPFEM fatigue simulations utilized in this work was the uncertainty in output fatigue indicator parameter (FIP) distributions resulting from the choice of size and number of statistical volume elements (SVEs) in an ensemble. Model parameter uncertainty was addressed by quantifying the uncertainty in FIP distributions resulting from CPFEM simulations using a model with parameters calibrated using experimental macroscale stress-strain results. A repeatable framework for epistemic uncertainty quantification for crystal plasticity models

aimed at studying FIP response of material systems was demonstrated. Additionally, interval bounds of uncertainty for the model at hand were provided.

In a similar manner, Chapter 5 was aimed at establishing a framework for uncertainty quantification. However, the focus of Chapter 5 was on aleatory UQ in the form of microstructure attribute distributions resulting from variability in processing from product-to-product and from batch-to-batch. Specifically, when using computational modeling tools to design a material for optimized performance, it is important to understand that once a material with desirable properties is designed for an application and a method of processing that material is established, in practice there will be a distribution of properties that are realized by repeating ostensibly the same processing route. Rather than designing a material solely to have optimized nominal properties, it is valuable for design engineers to understand the distribution of uncertainty for each property. This is especially true for fatigue critical applications, where the worst-case scenario is of the most interest, and robust design is at a premium. To this end, machine learning methods were utilized in the form of reduced order Gaussian process (GP) regression models. These GP models were trained to act as surrogates to the costly CPFEM simulations, facilitating rapid propagation of distributions of microstructure statistic uncertainty to provide statistical distributions of output properties of interest. Additionally, the uncertainty introduced by using a reduced order surrogate model in place of the CPFEM model was accounted for.

Lastly, in Chapter 6, the aforementioned various sources of uncertainty were consolidated, and these uncertainty quantification workflows were integrated with the inductive design exploration method (IDEM). With uncertainties well understood, a robust design case study was carried out on Ti64 to demonstrate the value of UQ in such a

framework. Specifically, several key microstructure attributes in a Ti64 alloy were designed to optimize the performance of a jet engine turbine blade exposed to multi-axial fatigue conditions.

Ultimately, the goal of this entire dissertation was to advance scientific and engineering frameworks and tools to facilitate effective multi-objective robust materials design. Uncertainty quantification was identified as a key gap that needed to be addressed to accomplish this goal. By decomposing the UQ problem into parts through Chapters 3, 4 and 5, and then reconciling the various forms of uncertainty into a combined UQ-informed IDEM framework in Chapter 6, several key gaps were addressed and a framework for robust design of metallic alloys for fatigue critical applications was demonstrated.

7.2 Recommendations for Future Work

Over the course of completing the work presented in this dissertation, a great deal of perspective on the key gaps in UQ for ICME was gained. In this section several of the most promising avenues for future research in this field are identified and discussed.

7.2.1 Investigation of Constitutive Model Form Uncertainty

One of the major contributions of this work was the investigation of epistemic uncertainty in the context of an ICME framework. Here, model form uncertainty was addressed by studying the uncertainty associated with the size and number of SVEs in an ensemble. However, this is not the only model form uncertainty worth considering. The constitutive model itself is, in essence, an approximation of the physics at play that are

being modeled. However, there are often different approaches to the same problem. In the case of constitutive models for CPFEM, there is a large body of research investigating different model forms for many different material systems. For example, Hennessey et al. [37] investigated three different constitutive model forms for Al7075-T6 alone. Typically, all of the competing established models have been calibrated and proven to agree well with experimental data for the given scenarios they are being developed for. This suggests that one should not necessarily aim to determine one model that is the "best", but rather, there can be value gained from each different approach to the problem.

An in-depth study of constitutive model form uncertainty spanning all established models for a given material system could help create a more robust workflow for materials design. This could be approached with an interval type method similar to how model parameter uncertainty was handled in Chapter 4. For example, if three competing constitutive models were each calibrated to the same experimental macroscopic stress-strain data, an interval of uncertainty in FIP response of the material system could be quantified by comparing the resulting extreme value FIP response of each model subjected to the same loading conditions.

7.2.2 Extension of Uncertainty Quantification and Propagation Methodology to Process-Structure Models

Another major area of interest for future research, building on the frameworks established in this dissertation, would be to explore similar uncertainty quantification and propagation workflows for computational models focused on process-structure linkages. A founding principle of ICME is the need to integrate the various different computational

materials modeling tools that have been established. The work presented in this dissertation focused on structure property linkages using a CPFEM model; however, both the UQ and IDEM frameworks discussed herein are specifically designed to address the full spectrum of PSPP linkages for a material system.

A long-term goal should be the development of an ICME ecosystem that integrates all of the various modeling tools available, using each for its own particular strength, to provide signal to an overarching design framework like IDEM. A logical next step toward overcoming this grand challenge of integrating computational modeling tools to study PSPP linkages would be to tackle aleatory uncertainty quantification and propagation through process-structure linkages using CALPHAD as the physics-based model and GP regression as a reduced order surrogate to propagate uncertainty distributions.

7.2.3 Extension of Aleatory Uncertainty Quantification Framework to Quantify Uncertainty in Additional Key Microstructure Attributes

Along similar lines as the previous section, it is re-emphasized here that it is vital for ICME workflows to consider uncertainty quantification for all aspects robust design of a material system with performance requirements for a specific application. In this dissertation, three key microstructure attributes were the focus of the aleatory uncertainty quantification study in Chapter 5 and the material design case study in Chapter 6. These were the average grain size, the volume fractions of primary alpha phase in alpha-beta titanium, and the crystallographic texture. One of the major challenges addressed for this work was determining how best to featurize these aspects of the microstructure so that a statistical distribution representing their uncertainty could be assigned and propagated. Of

course, there are several other important microstructure attributes that should be considered in the design of metallic alloys.

Long-term, it would be valuable to model all of the relevant structure property linkages for every different material system of interest, and establish uncertainty quantification and propagation tools for each, along the lines of the framework established in this dissertation. However, this is a significant and time-consuming problem. A more tractable short-term goal would be to focus on residual stress and surface effects and determine how best to represent each of these to enable uncertainty quantification. These two particular features are of interest relative to others in view of their relevance to the emerging field of additive manufacturing.

Additive manufacturing provides new realm of possibilities for materials design, but also poses a lot of challenges in terms of material robustness. Uncertainty quantification for microstructure attributes like residual stress and surface effects that are particularly important to the issue of robust additive manufacturing could be a vital step toward the future of the field.

7.2.4 Utilization of Multiscale Experimental and Modeling Techniques to Reduce Epistemic Uncertainty

Lastly, uncertainty reduction is of great practical importance for material design using ICME. There are a number of ways that epistemic uncertainty can be reduced. In Chapters 4 and 5 of this dissertation, the noise-like uncertainty associated with the size and number of SVEs in an ensemble were studied and the uncertainty was reduced to a point where a GP regression model could be successfully trained on FIP data. However, this is

just one aspect of epistemic uncertainty. Other sources of epistemic uncertainty, like model parameter uncertainty, could be reduced by using multiscale modeling tools. For example, the constitutive model parameters used for the Ti64 model in this work were calibrated using experimental macroscopic stress-strain data, however, with a particular interest in driving forces for fatigue at the mesoscale, it would be beneficial to consider synchrotron data to calibrate the model to experimental FIP data.

Similarly, integrating computational models from multiple length scales can provide more information about a material system than any one length scale alone. There has been a large body of research in hierarchical multiscale modeling of materials and this remains a promising area of research. In particular, by understanding the physics at play at smaller length scales, one could decrease uncertainty in model parameters for a CPFEM model, effectively shrinking the epistemic uncertainty interval and providing more robust decision support for materials design.

Appendix A: Crystal Plasticity Finite Element Models

This section provides in depth details about the crystal plasticity finite element models used for the Ti64 and Al7075-T6 material systems in this dissertation. The Ti64 model description was adapted from Smith [144] and the Al7075-T6 model description was adapted from Hennessey [37].

A.1 Crystal Plasticity Framework

The crystal plasticity model assumes thermally activated dislocation glide through the lattice [145, 146]. The deformation gradient is multiplicatively decomposed into dislocation slip and elastic lattice deformation, including rigid body rotation of the crystalline lattice, i.e.,

$$\mathbf{F}=\mathbf{F}^{e}\cdot\mathbf{F}^{p} \qquad \textit{(A.1.1)}$$

where $\mathbf{F}^{e}$ is representative of the elastic stretching and rigid body rotation of the lattice and $\mathbf{F}^{p}$ describes the cumulative effect of dislocation migration through the lattice. The plastic velocity gradient for the isoclinic, lattice invariant intermediate configuration is determined by summing the crystallographic shearing rates over all of α slip systems [145], i.e.,

$$\hat{\mathbf{L}}^{p}=\sum_{\alpha=1}^{N_{sys}}\dot{\gamma}^{\alpha}\left(\mathbf{s}_{0}^{\alpha}\otimes\mathbf{n}_{0}^{\alpha}\right)=\dot{\mathbf{F}}^{p}\cdot\left(\mathbf{F}^{p}\right)^{-1} \qquad \textit{(A.1.2)}$$

where $\mathbf{n}_0^\alpha$ and $\mathbf{s}_0^\alpha$ are the slip plane and slip direction normal vectors, respectively, in the reference configuration. These vectors have the same orientation in both the reference and isoclinic intermediate configurations.

A.2 Ti64 Power Law Flow Rule Crystal Plasticity Model

The power law formulation was first implemented for Ti-6Al-4V by Mayeur [147]; it was then extended to describe complex loading histories by Zhang et al. [102] and high-cycle fatigue (HCF) loading by Bridier et al. [148]. Przybyla and McDowell [82] utilized this calibrated model to investigate HCF performance over a range of Ti64 microstructures by employing extreme value statistics. The power law shearing rate relation is given by

$$\dot{\gamma}^\alpha = \dot{\gamma}_o \left\langle \frac{\left|\tau^\alpha - \chi^\alpha\right| - \kappa^\alpha}{D^\alpha} \right\rangle^M \operatorname{sgn}\left(\tau^\alpha - \chi^\alpha\right) \qquad \textbf{\textit{(A.2.1)}}$$

Here, D^α is the drag stress on the α^{th} slip system, $\dot{\gamma}_o$ is the reference shearing rate, χ^α is the back stress, and κ^α is the threshold stress. The threshold stress is defined as the sum of the Hall-Petch strength term and a softening term, κ_s^α, i.e.,

$$\kappa^{\alpha} = \frac{\kappa_y}{\sqrt{d}} + \kappa_s^{\alpha} \qquad \textbf{(A.2.2)}$$

where κ_y is the Hall-Petch slope and *d* is the mean slip distance in the α-phase (primary or secondary). The strength contribution of the Hall-Petch term is assumed not to evolve so that the evolution of the threshold stress is governed solely by the softening term, which follows a dynamic recovery law, i.e.,

$$\dot{\kappa}^{\alpha} = \dot{\kappa}_s^{\alpha} = -\mu\kappa_s \left|\dot{\gamma}^{\alpha}\right| \qquad \textbf{(A.2.3)}$$

where μ is the softening rate coefficient. The initial value of κ_s^{α}, prior to the breakdown of short range order, is given by $\left(\kappa_s^{\alpha}\right)_{t=0}$. It is assumed that drag stress depends only on the critical resolved shear stress, i.e.,

$$D^{\alpha} = \tau_{CRSS}^{\alpha} \qquad \textbf{(A.2.4)}$$

Here, CRSS τ_{CRSS}^{α} is the critical resolved shear stress on the α_{th} slip system. The drag stress does not evolve so that $\dot{D}^{\alpha} = 0$. The back stress is initially set to zero and it evolves according to an Armstrong-Frederick direct hardening/dynamic recovery relation [149], i.e.,

$$\dot{\chi}^{\alpha} = h\dot{\gamma}^{\alpha} - h_D \chi^{\alpha} \left| \dot{\gamma}^{\alpha} \right| \qquad \textbf{(A.2.5)}$$

In Equation ***(A*.2.5)**, h is the direct hardening coefficient and h_D is the dynamic recovery coefficient. The saturated value of the back stress is determined by the ratio of the direct hardening constant divided by the dynamic recovery term corresponding to $\dot{\chi}^{\alpha} = 0$, i.e.,

$$\chi_{sat} = \frac{h}{h_D} \qquad \textbf{(A.2.6)}$$

The critical resolved shear stress (CRSS) of the α + β colony grains is known to be higher than that of the primary α-phase grains for slip systems due to the presence of the lamellar interfaces. To account for this difference in the CRSS, a factor of 1.25 is applied to the basal slip systems and the prismatic slip system that is oriented parallel to the lamellar laths [148], i.e.,

$$\tau^{\alpha}_{CRSS}\left(\alpha+\beta\right) = 1.25\tau^{\alpha}_{CRSS}\left(\alpha\right) \qquad \textbf{(A.2.7)}$$

The critical resolved shear stress in compression has also been modified to account for the tension-compression asymmetry observed experimentally. It has been hypothesized that the physical basis of this asymmetry is the non-planar core structure observed in a-type screw dislocations in titanium [150], and core constriction necessary to render the dislocations mobile is not of Schmid character. To model this non-Schmid behavior, Qin and Bassani [151] suggested that the critical resolved shear stress be augmented by a strength term with linear dependence on secondary shear stresses, i.e.,

$$\tau^{*\alpha} = \tau^{\alpha} + \sum_{i}^{N_{sys}} \alpha_i^{\alpha} \tau_i^{\alpha} \qquad \textbf{(A.2.8)}$$

where $\tau^{*\alpha}$ is the modified critical resolved shear stress, N_{sys} is the number of influential secondary slip systems for core spreading, and α_i^{α} are model parameters that reflect core constriction contributions. Screw dislocations on prismatic slip planes dominate slip of α-Ti [150]. It has been proposed that these prismatic dislocations can dissociate into the pyramidal planes that share common slip directions [147, 150].

In the current framework, the prismatic threshold stress is increased in compression by the addition of a non-planar dislocation core strength term. A simple first order 3D criterion for activation of this asymmetry term is adopted as det**(F)** < 1, i.e., indicative of compressive dilatation. While this specific formulation can distinguish between uniaxial tension and compression loading conditions, additional work is necessary to assess whether the condition on det**(F)** is sufficient or requires modification for more complex multiaxial stress states, e.g., combined axial-torsion loading or shear. The asymmetric strength contribution is described by the relations

$$\begin{aligned} \tau_{CRSS}^{prism} &= \tau_{CRSS}^{prism}\Big|_0 + \eta\left(\left|\tau_{RSS}^{pyr1,1}\right| + \left|\tau_{RSS}^{pyr1,2}\right|\right), J = \det(\mathbf{F}) < 1 \\ \tau_{CRSS}^{prism} &= \tau_{CRSS}^{prism}\Big|_0, J \geq 1 \end{aligned} \qquad \textbf{(A.2.9)}$$

where the terms $\tau_{RSS}^{pyr1,1}$ and $\tau_{RSS}^{pyr1,2}$ represent the resolved shear stresses on the two first order pyramidal systems that share the same slip direction as the prismatic plane under consideration, η is a parameter that defines the sensitivity of the asymmetry strength to the resolved shear stress on these pyramidal planes, and $\tau_{CRSS}^{prism}\Big|_0$ is the critical resolved shear stress for the prismatic slip systems for positive det**(F)**. A summary of the previously identified model parameters appears in Table A.1.

Table A.1. Calibrated parameter values for Ti64 constitutive model at room temperature (partially adapted from [91]).

Property	Value
$\dot{\gamma}_o$	0.001 s^{-1}
κ_y	12.7 MPa $mm^{0.5}$
$\chi_{t=0}$	0 MPa
$\left(\tau_{cr}^{\alpha}\right)_{basal}$	339 MPa
$\left(\tau_{cr}^{\alpha}\right)_{prism}$	266 MPa
$\left(\tau_{cr}^{\alpha}\right)_{pyr\langle a\rangle}$	450 MPa
$\left(\tau_{cr}^{\alpha}\right)_{pyr\langle a+c\rangle}$	551 MPa
$(\kappa^{\alpha}_s)_{t=0}$	42 MPa
η	22
C11	172,832 MPa
C12	97,910 MPa
C13	73,432 MPa
C33	192,308 MPa
C44	49,700 MPa
$\mu_{threshold}$	2
H	8000 MPa
h_D	8000

A.3 Al7075-T6 Constitutive Model

The crystal plasticity modeling framework of McGinty [152], applied originally to Oxygen Free High Conductivity (OFHC) Cu, serves as the basis for the constitutive model implementation. The flow rule is defined by

$$\dot{\gamma}^{(\alpha)} = \dot{\gamma}_0 \left| \frac{\tau^{(\alpha)} - \chi^{(\alpha)}}{g^{(\alpha)}} \right|^m \operatorname{sgn}(\tau^{(\alpha)} - \chi^{(\alpha)}) \qquad \textit{(A.3.1)}$$

where $\dot{\gamma}^{(\alpha)}$ is the shearing rate for slip system α, $\dot{\gamma}_0^{(\alpha)}$ is the reference shearing rate, and τ^{α}, χ^{α} and g^{α} are the corresponding slip system shear stress, back stress and drag stress, respectively. Here m is the strain rate sensitivity exponent. The hardening law, which governs the evolution of the back stress and drag stress on each slip system, has the general form

$$\begin{aligned} \dot{g}^{\alpha} &= \hat{g}(\dot{\gamma}^{\beta}, g^{\alpha}) \\ \dot{\chi}^{\alpha} &= \hat{\chi}(\dot{\gamma}^{\alpha}, \chi^{\alpha}) \end{aligned} \qquad \textbf{\textit{(A.3.2)}}$$

In ***(A.3.2)*** the rate of evolution of the drag stress, representing isotropic hardening, is a function of the shearing rate on all slip systems as well as the current value of the drag stress. However, the kinematic hardening response, captured by the evolution of the back stress, is only a function of the shearing rate on the current slip system as well as the current value of the back stress.

This model was introduced in order to address some of the shortcomings of the Armstrong-Frederick [152] back stress formulation when loaded cyclically with an imposed mean strain. The model incorporates a two-term, Ohno-Wang [153] (OW) type equation for the back stress, adapted from a polycrystal macroscopic model proposed by McDowell [154]. The rate of change of this from of the back stress is given by

$$\dot{g}^{(\alpha)} = H_{dir} \sum_{\beta=1}^{N_{sys}} h^{\alpha\beta} \left| \dot{\gamma}^{(\beta)} \right| - H_{dyn} g^{(\alpha)} \sum_{\beta=1}^{N_{sys}} \left| \dot{\gamma}^{(\beta)} \right| \qquad \textbf{\textit{(A.3.3)}}$$

where $h^{\alpha\beta}$ is the latent hardening matrix, controlling the relative contributions of self and latent hardening of the slip systems. A summary of the previously identified model parameters appears in Table A.2.

Table A.2. Calibrated parameter values for Al7075-T6 constitutive model at room temperature (adapted from [37]).

Property	Value
C11	107.3 GPa
C12	60.9 GPa
C44	28.3 GPa
$\dot{\gamma}_o$	0.001 s^{-1}
m	75
G_0	35 MPa
h_1	2,000 GPa
r_1	20,000
h_2	135 GPa
r_2	1421
m_i	200

References

1. McDowell, D.L. and D. Backman, *Simulation-Assisted Design and Accelerated Insertion of Materials.* Computational Methods for Microstructure-Property Relationships, 2011: p. 617-647.
2. White, A., *The Materials Genome Initiative: One year on.* Mrs Bulletin, 2012. **37**(8): p. 715-716.
3. McDowell, D.L., et al., *Integrated Design of Multiscale, Multifunctional Materials and Products.* Integrated Design of Multiscale, Multifunctional Materials and Products, 2010: p. 1-370.
4. Goulding, A.N., Leung, J. F., & Neu, R. W., *Communicating Materials Systems Knowledge through Processing-Structure-Properties-Performance (PSPP) Maps.* Smartech, 2018.
5. Ghanem, R., D. Higdon, and H. Owhadi, *Handbook of uncertainty quantification*. 2017, New York: Springer.
6. Bostanabad, R., et al., *Uncertainty quantification in multiscale simulation of woven fiber composites.* Computer Methods in Applied Mechanics and Engineering, 2018. **338**: p. 506-532.
7. Patrone, P., A. Kearsley, and A. Dienstfrey. *The role of data analysis in uncertainty quantification: case studies for materials modeling*. in *2018 AIAA Non-Deterministic Approaches Conference*. 2018.
8. Otis, R.A. and Z.-K. Liu, *High-throughput thermodynamic modeling and uncertainty quantification for ICME.* JOM, 2017. **69**(5): p. 886-892.

9. Honarmandi, P. and R. Arróyave, *Uncertainty Quantification and Propagation in Computational Materials Science and Simulation-Assisted Materials Design.* Integrating Materials and Manufacturing Innovation, 2020: p. 1-41.

10. Yeratapally, S.R., et al., *Bayesian uncertainty quantification and propagation for validation of a microstructure sensitive model for prediction of fatigue crack initiation.* Reliability Engineering & System Safety, 2017. **164**: p. 110-123.

11. Bandyopadhyay, R., V. Prithivirajan, and M.D. Sangid, *Uncertainty quantification in the mechanical response of crystal plasticity simulations.* JOM, 2019. **71**(8): p. 2612-2624.

12. Bandyopadhyay, R., et al., *Microstructure-sensitive critical plastic strain energy density criterion for fatigue life prediction across various loading regimes.* Proceedings of the Royal Society A, 2020. **476**(2236): p. 20190766.

13. Kotha, S., D. Ozturk, and S. Ghosh, *Parametrically homogenized constitutive models (PHCMs) from micromechanical crystal plasticity FE simulations, part I: Sensitivity analysis and parameter identification for Titanium alloys.* International Journal of Plasticity, 2019. **120**: p. 296-319.

14. Kotha, S., D. Ozturk, and S. Ghosh, *Uncertainty-quantified parametrically homogenized constitutive models (UQ-PHCMs) for dual-phase α/β titanium alloys.* npj Computational Materials, 2020. **6**(1): p. 1-20.

15. Jiang, Z., W. Chen, and B.J. German, *Multidisciplinary Statistical Sensitivity Analysis Considering Both Aleatory and Epistemic Uncertainties.* AIAA Journal, 2016. **54**(4): p. 1326-1338.

16. Zaman, K., M. McDonald, and S. Mahadevan, *Probabilistic Framework for Uncertainty Propagation With Both Probabilistic and Interval Variables.* Journal of Mechanical Design, 2011. **133**(2): p. 1-14.

17. Jiang, Z., W. Chen, and B. German, *Statistical Sensitivity Analysis Considering both Aleatory and Epistemic Uncertainties in Multidisciplinary Design*, in *15th AIAA/ISSMO Multidisciplinary Analysis and Optimization Conference*. 2014, American Institute of Aeronautics and Astronautics. p. 2870.

18. Swiler, L.P., M.S. Eldred, and B.M. Adams, *Dakota: bridging advanced scalable uncertainty quantification algorithms with production deployment.* Handbook of Uncertainty Quantification, 2017: p. 1651-1693.

19. Chernatynskiy, A., S.R. Phillpot, and R. LeSar, *Uncertainty quantification in multiscale simulation of materials: A prospective.* Annual Review of Materials Research, 2013. **43**: p. 157-182.

20. Ma, Y., et al., *Hybrid uncertainty quantification for probabilistic corrosion damage prediction for aging RC bridges.* Journal of Materials in Civil Engineering, 2014. **27**(4): p. 04014152.

21. Hu, Z. and S. Mahadevan, *Uncertainty quantification in prediction of material properties during additive manufacturing.* Scripta Materialia, 2017. **135**: p. 135-140.

22. Cai, G. and S. Mahadevan, *Uncertainty quantification of manufacturing process effects on macroscale material properties.* International Journal for Multiscale Computational Engineering, 2016. **14**(3).

23. McDonald, M. and S. Mahadevan, *Uncertainty Quantification and Propagation in Multidisciplinary Analysis and Optimization*, in *12th AIAA/ISSMO Multidisciplinary Analysis and Optimization Conference*. 2008, American Institute of Aeronautics and Astronautics. p. 6038.

24. Bessa, M.A., et al., *A framework for data-driven analysis of materials under uncertainty: Countering the curse of dimensionality.* Computer Methods in Applied Mechanics and Engineering, 2017. **320**: p. 633-667.

25. Martin, J.D. and T.W. Simpson, *Use of Kriging Models to Approximate Deterministic Computer Models.* AIAA Journal, 2005. **43**(4): p. 853-863.

26. Hombal, V. and S. Mahadevan, *BIAS MINIMIZATION IN GAUSSIAN PROCESS SURROGATE MODELING FOR UNCERTAINTY QUANTIFICATION.* 2011. **1**(4): p. 321-349.

27. Bilionis, I. and N. Zabaras, *Bayesian uncertainty propagation using Gaussian processes.* Handbook of Uncertainty Quantification, 2016: p. 1-45.

28. Le Maître, O.P., et al., *Uncertainty propagation using Wiener–Haar expansions.* Journal of Computational Physics, 2004. **197**(1): p. 28-57.

29. Karniadakis, G.E., *Uncertainty quantification (UQ).* 2011.

30. Venturi, D., H. Cho, and G.E. Karniadakis, *Mori-Zwanzig approach to uncertainty quantification.* Handbook of uncertainty quantification, 2016: p. 1-36.

31. Owen, N., et al., *Comparison of surrogate-based uncertainty quantification methods for computationally expensive simulators.* SIAM/ASA Journal on Uncertainty Quantification, 2017. **5**(1): p. 403-435.

32. Pedregosa, F., et al., *Scikit-learn: Machine learning in Python.* Journal of machine learning research, 2011. **12**(Oct): p. 2825-2830.

33. Reed, R.P., United States. National Bureau of Standards., and Battelle Memorial Institute. Columbus Laboratories., *The Economic effects of fracture in the United States*. Special publication. 1983, Washington, D.C.: U.S. Dept. of Commerce, National Bureau of Standards.

34. Wöhler, A., *Versuche über die Festigkeit der Eisenbahnwagenachsen.* Zeitschrift für Bauwesen, 1860. **10**: p. 160-161.

35. Basquin, O. *The exponential law of endurance tests*. in *Proc Am Soc Test Mater*. 1910.

36. Hennessey, C., G.M. Castelluccio, and D.L. McDowell, *Sensitivity of polycrystal plasticity to slip system kinematic hardening laws for Al 7075-T6.* Materials Science and Engineering: A, 2017. **687**: p. 241-248.

37. Hennessey, C.D., *Modeling microstructurally small crack growth in Al 7075-T6*. 2015, Georgia Institute of Technology.

38. McDowell, D. and F. Dunne, *Microstructure-sensitive computational modeling of fatigue crack formation.* International journal of fatigue, 2010. **32**(9): p. 1521-1542.

39. McDowell, D., et al., *Microstructure-based fatigue modeling of cast A356-T6 alloy*. Engineering Fracture Mechanics, 2003. **70**(1): p. 49-80.

40. Shyam, A. and W. Milligan, *A model for slip irreversibility, and its effect on the fatigue crack propagation threshold in a nickel-base superalloy.* Acta materialia, 2005. **53**(3): p. 835-844.

41. Hoshide, T. and D. Socie, *Crack nucleation and growth modeling in biaxial fatigue.* Engineering fracture mechanics, 1988. **29**(3): p. 287-299.

42. McDowell, D., *Damage mechanics and metal fatigue: a discriminating perspective.* International Journal of Damage Mechanics, 1999. **8**(4): p. 376-403.

43. Fatemi, A. and D.F. Socie, *A critical plane approach to multiaxial fatigue damage including out-of-phase loading.* Fatigue & Fracture of Engineering Materials & Structures, 1988. **11**(3): p. 149-165.

44. Przybyla, C.P. and D.L. McDowell, *Microstructure-sensitive extreme value probabilities for high cycle fatigue of Ni-base superalloy IN100.* International Journal of Plasticity, 2010. **26**(3): p. 372-394.

45. Gumbel, E.J., *Statistics of extremes*. 2012: Courier Corporation.

46. Castillo, E., *Extreme value theory in engineering*. 2012: Elsevier.

47. Du, X. and W. Chen, *Efficient Uncertainty Analysis Methods for Multidisciplinary Robust Design.* AIAA Journal, 2002. **40**(3): p. 545-552.

48. Choi, H.-J., et al., *An inductive design exploration method for hierarchical systems design under uncertainty.* Engineering Optimization, 2008. **40**(4): p. 287-307.

49. Kern, P.C., et al., *pyDEM: A generalized implementation of the inductive design exploration method.* Materials & Design, 2017. **134**(Supplement C): p. 293-300.

50. Kern, P.C., et al., *pyDEM: A generalized implementation of the inductive design exploration method.* Materials & Design, 2017. **134**: p. 293-300.

51. McDowell, D.L., et al., *Integrated design of multiscale, multifunctional materials and products*. 2009: Butterworth-Heinemann.

52. Lütjering, G. and J.C. Williams, *Beta Alloys*. 2007: Springer.

53. Priddy, M.W., et al., *Strategies for rapid parametric assessment of microstructure-sensitive fatigue for HCP polycrystals.* International Journal of Fatigue, 2017. **104**(Supplement C): p. 231-242.

54. Williams, J., R. Baggerly, and N. Paton, *Deformation behavior of HCP Ti-Al alloy single crystals.* Metallurgical and Materials Transactions A, 2002. **33**(3): p. 837-850.

55. Olson, G.B., *Computational design of hierarchically structured materials.* Science, 1997. **277**(5330): p. 1237-1242.

56. Goulding, A., J.F. Leung, and R. Neu, *Communicating Materials Systems Knowledge through Processing-Structure-PropertiesPerformance (PSPP) Maps.* Journal of Materials Education, 2018. **40**(1-2): p. 1-18.

57. Goulding, A.N., *Implementing the materials genome initiative: Best practice for developing meaningful experimental data sets in aluminum-zinc-magnesium-copper alloys*. 2016, Georgia Institute of Technology.

58. Wöhler, A., *Versuche über die Festigkeit der Eisenbahnwagenachsen.* Zeitschrift für Bauwesen, 1860. **10**(1860): p. 160-161.

59. McDowell, D.L., *Basic issues in the mechanics of high cycle metal fatigue.* International Journal of Fracture, 1996. **80**(2-3): p. 103.

60. Anderson, T.L., *Fracture mechanics: fundamentals and applications*. 2017: CRC press.

61. Tokaji, K., et al., *Limitations of linear elastic fracture mechanics in respect of small fatigue cracks and microstructure.* Fatigue & Fracture of Engineering Materials & Structures, 1986. **9**(1): p. 1-14.

62. Akiniwa, Y., K. Tanaka, and E. Matsui, *Statistical characteristics of propagation of small fatigue cracks in smooth specimens of aluminium alloy 2024-T3.* Materials Science and Engineering: A, 1988. **104**: p. 105-115.

63. McDowell, D.L., *A perspective on trends in multiscale plasticity.* International Journal of Plasticity, 2010. **26**(9): p. 1280-1309.

64. Fatemi, A. and P. Kurath, *Multiaxial fatigue life predictions under the influence of mean-stresses.* Journal of Engineering Materials and Technology, 1988. **110**(4): p. 380-388.

65. Rovinelli, A., et al., *Assessing reliability of fatigue indicator parameters for small crack growth via a probabilistic framework.* Modelling and Simulation in Materials Science and Engineering, 2017. **25**(4): p. 045010.

66. Brown, M.W. and K. Miller, *A theory for fatigue failure under multiaxial stress-strain conditions.* Proceedings of the Institution of Mechanical Engineers, 1973. **187**(1): p. 745-755.

67. Rovinelli, A., et al., *Predicting the 3D fatigue crack growth rate of small cracks using multimodal data via Bayesian networks: In-situ experiments and crystal plasticity simulations.* Journal of the Mechanics and Physics of Solids, 2018. **115**: p. 208-229.

68. Nicolas, A., et al., *Predicting fatigue crack initiation from coupled microstructure and corrosion morphology effects.* Engineering Fracture Mechanics, 2019. **220**: p. 106661.

69. Castelluccio, G.M. and D.L. McDowell, *Assessment of small fatigue crack growth driving forces in single crystals with and without slip bands.* International journal of fracture, 2012. **176**(1): p. 49-64.

70. Przybyla, C.P., et al., *Microstructure-sensitive HCF and VHCF simulations.* International Journal of Fatigue, 2013. **57**: p. 9-27.

71. Pineau, A., et al., *Failure of metals II: Fatigue.* Acta Materialia, 2016. **107**: p. 484-507.

72. Musinski, W.D. and D.L. McDowell, *Microstructure-sensitive probabilistic modeling of HCF crack initiation and early crack growth in Ni-base superalloy IN100 notched components.* International Journal of Fatigue, 2012. **37**: p. 41-53.

73. Shenoy, M., J. Zhang, and D.L. McDowell, *Estimating fatigue sensitivity to polycrystalline Ni-base superalloy microstructures using a computational approach.* Fatigue & Fracture of Engineering Materials & Structures, 2007. **30**(10): p. 889-904.

74. Salajegheh, N. and D.L. McDowell, *Microstructure-sensitive weighted probability approach for modeling surface to bulk transition of high cycle fatigue failures dominated by primary inclusions.* International Journal of Fatigue, 2014. **59**: p. 188-199.

75. Musinski, W.D. and D.L. McDowell, *Simulating the effect of grain boundaries on microstructurally small fatigue crack growth from a focused ion beam notch*

through a three-dimensional array of grains. Acta Materialia, 2016. **112**: p. 20-39.

76. Musinski, W.D. and D.L. McDowell, *On the eigenstrain application of shot-peened residual stresses within a crystal plasticity framework: Application to Ni-base superalloy specimens.* International Journal of Mechanical Sciences, 2015. **100**: p. 195-208.

77. Prasannavenkatesan, R., et al., *3D modeling of subsurface fatigue crack nucleation potency of primary inclusions in heat treated and shot peened martensitic gear steels.* International Journal of Fatigue, 2009. **31**(7): p. 1176-1189.

78. Salajegheh, N., et al., *Finite Element Simulation of Shielding/Intensification Effects of Primary Inclusion Clusters in High Strength Steels Under Fatigue Loading.* 2014. **136**.

79. Hennessey, C.D., *MODELING MICROSTRUCTURALLY SMALL CRACK GROWTH IN AL 7075-T6*, in *George W. Woodruff School of Mechanical Engineering*. 2015, Georgia Institute of Technology.

80. Gall, K., et al., *On the driving force for fatigue crack formation from inclusions and voids in a cast A356 aluminum alloy.* International Journal of Fracture, 2001. **108**(3): p. 207-233.

81. Xue, Y., et al., *Microstructure-based multistage fatigue modeling of aluminum alloy 7075-T651*. 2007. **74**: p. 2810-2823.

82. Przybyla, C.P. and D.L. McDowell, *Simulated microstructure-sensitive extreme value probabilities for high cycle fatigue of duplex Ti–6Al–4V.* International Journal of Plasticity, 2011. **27**(12): p. 1871-1895.

83. Przybyla, C.P. and D.L. McDowell, *Microstructure-sensitive extreme-value probabilities of high-cycle fatigue for surface vs. subsurface crack formation in duplex Ti–6Al–4V.* Acta Materialia, 2012. **60**(1): p. 293-305.

84. Gumbel, E.J. *Les valeurs extrêmes des distributions statistiques*. in *Annales de l'institut Henri Poincaré*. 1935.

85. Rowenhorst, D., et al., *3D crystallographic and morphological analysis of coarse martensite: Combining EBSD and serial sectioning.* Scripta Materialia, 2006. **55**(1): p. 11-16.

86. Jin, H., et al., *Three-dimensional texture determination of 6111 aluminium alloy sheet by precise serial sectioning and EBSD measurement.* Materials science and technology, 2005. **21**(4): p. 419-428.

87. Mandal, S., et al., *Generation of statistically representative synthetic three-dimensional microstructures.* Scripta Materialia, 2018. **146**: p. 128-132.

88. Smith, M., *ABAQUS/Standard User's Manual, Version 6.9.* 2009, Simulia: Providence.

89. Groeber, M.A. and M.A. Jackson, *DREAM.3D: A Digital Representation Environment for the Analysis of Microstructure in 3D.* Integrating Materials and Manufacturing Innovation, 2014. **3**(1): p. 5.

90. Kern, P.C., *Improvements to the computational pipeline in crystal plasticity estimates of high cycle fatigue of microstructures*. 2016, Georgia Institute of Technology.

91. Smith, B., D. Shih, and D. McDowell, *Cyclic plasticity experiments and polycrystal plasticity modeling of three distinct Ti alloy microstructures.* International Journal of Plasticity, 2018. **101**: p. 1-23.

92. Kanit, T., et al., *Determination of the size of the representative volume element for random composites: statistical and numerical approach.* International Journal of Solids and Structures, 2003. **40**(13): p. 3647-3679.

93. McDowell, D.L., *Damage Mechanics and Metal Fatigue: A Discriminating Perspective.* International Journal of Damage Mechanics, 1999. **8**(4): p. 376-403.

94. Smith, R.C., *Uncertainty quantification: theory, implementation, and applications*. Vol. 12. 2013: Siam.

95. Möller, B. and M. Beer, *Engineering computation under uncertainty–capabilities of non-traditional models.* Computers & Structures, 2008. **86**(10): p. 1024-1041.

96. Rasmussen, C.E., *Gaussian processes in machine learning*, in *Advanced lectures on machine learning*. 2004, Springer. p. 63-71.

97. Choi, H.J., et al., *An inductive design exploration method for the integrated design of multi-scale materials and products.* Proceedings of the ASME International Design Engineering Technical Conferences and Computers and Information in Engineering Conference, 2005, Vol 2, Pts A and B, 2005: p. 859-870.

98. McDonald, M. and S. Mahadevan, *Uncertainty Quantification and Propagation in Multidisciplinary Analysis and Optimization*, in *12th AIAA/ISSMO Multidisciplinary Analysis and Optimization Conference*. 2008, American Institute of Aeronautics and Astronautics.

99. Lacy, T.E., R. Talreja, and D.L. McDowell, *Effects of damage distribution on evolution*, in *Applications of continuum damage mechanics to fatigue and fracture*. 1997, ASTM International.

100. Priddy, M.W., et al., *Strategies for rapid parametric assessment of microstructure-sensitive fatigue for HCP polycrystals.* International Journal of Fatigue, 2017. **104**: p. 231-242.

101. Mayeur, J. and D. McDowell, *A three-dimensional crystal plasticity model for duplex Ti–6Al–4V.* International journal of plasticity, 2007. **23**(9): p. 1457-1485.

102. Zhang, M., J. Zhang, and D. McDowell, *Microstructure-based crystal plasticity modeling of cyclic deformation of Ti–6Al–4V.* International Journal of Plasticity, 2007. **23**(8): p. 1328-1348.

103. Huang, Y., *A user-material subroutine incroporating single crystal plasticity in the ABAQUS finite element program*. 1991: Harvard Univ.

104. SIMULIA, *ABAQUS 6.16-1*. 2016, SIMULIA Providence, RI.

105. Zhang, M., J. Zhang, and D.L. McDowell, *Microstructure-based crystal plasticity modeling of cyclic deformation of Ti–6Al–4V.* International Journal of Plasticity, 2007. **23**(8): p. 1328-1348.

106. Tallman, A.E., *Hierarchical Multiscale Materials Modeling: Calibration, Uncertainty Quantification, and Decision Support*. 2018, Georgia Institute of Technology.

107. Millman, K. and M. Aivazis, *Python for Scientists and Engineers*. Vol. 13. 2011. 9-12.

108. Renard, A., et al., *The cyclic stress-strain response of polycrystalline Al Zn Mg alloy and commercial alloys based on this system.* Materials Science and Engineering, 1983. **60**(2): p. 113-120.

109. Arcari, A., *ENHANCED STRAIN-BASED FATIGUE METHODOLOGY FOR HIGH STRENGTH ALUMINUM ALLOYS*, in *Department of Engineering Mechanics*. 2010, Virginia Institute of Technology: Blacksburg, VA.

110. McDowell, D.L., *Simulation-based strategies for microstructure-sensitive fatigue modeling.* Materials Science and Engineering: A, 2007. **468**: p. 4-14.

111. McDowell, D.L. and J.-Y. Berard, *A δJ-based approach to biaxial fatigue* Fatigue & Fracture of Engineering Materials & Structures, 1992. **15**(8): p. 719-741.

112. Castelluccio, G.M. and D.L. McDowell, *Mesoscale modeling of microstructurally small fatigue cracks in metallic polycrystals.* Materials Science and Engineering: A, 2014. **598**: p. 34-55.

113. Castelluccio, G.M. and D.L. McDowell, *Microstructure and mesh sensitivities of mesoscale surrogate driving force measures for transgranular fatigue cracks in polycrystals.* Materials Science and Engineering: A, 2015. **639**: p. 626-639.

114. Stopka, K.S., G. Whelan, and D.L. McDowell, *MICROSTRUCTURE-SENSITIVE ICME WORKFLOWS FOR FATIGUE CRITICAL APPLICATIONS.* 2019.

115. Li, C. and S. Mahadevan, *An efficient modularized sample-based method to estimate the first-order Sobol′ index.* Reliability Engineering & System Safety, 2016. **153**: p. 110-121.

116. Saltelli, A., et al., *Global sensitivity analysis: the primer*. 2008: John Wiley & Sons.

117. Turkmen, H.S., et al., *On the mechanical behaviour of AA 7075-T6 during cyclic loading.* International Journal of Fatigue, 2003. **25**(4): p. 267-281.

118. Zhao, T. and Y. Jiang, *Fatigue of 7075-T651 aluminum alloy.* International Journal of Fatigue, 2008. **30**(5): p. 834-849.

119. Hidalgo, P., et al., *Influence of the processing temperature on the microstructure, texture, and hardness of the 7075 aluminum alloy fabricated by accumulative roll bonding.* Metallurgical and Materials Transactions A, 2010. **41**(3): p. 758-767.

120. Roy, S., et al., *Development of solidification microstructure in boron-modified alloy Ti–6Al–4V–0.1B.* Acta Materialia, 2011. **59**(14): p. 5494-5510.

121. Wang, Y.C. and T.G. Langdon, *Influence of phase volume fractions on the processing of a Ti–6Al–4V alloy by high-pressure torsion.* Materials Science and Engineering: A, 2013. **559**: p. 861-867.

122. Gey, N. and M. Humbert, *Characterization of the variant selection occurring during the α→β→α phase transformations of a cold rolled titanium sheet.* Acta Materialia, 2002. **50**(2): p. 277-287.

123. Boschert, S. and R. Rosen, *Digital Twin—The Simulation Aspect*, in *Mechatronic Futures: Challenges and Solutions for Mechatronic Systems and their Designers*,

P. Hehenberger and D. Bradley, Editors. 2016, Springer International Publishing: Cham. p. 59-74.

124. Kraft, E.M. *The air force digital thread/digital twin-life cycle integration and use of computational and experimental knowledge*. in *54th AIAA Aerospace Sciences Meeting*. 2016.

125. Whelan, G. and D.L. McDowell, *Uncertainty quantification in ICME workflows for fatigue critical computational modeling.* Engineering Fracture Mechanics, 2019. **220**: p. 106673.

126. Wang, B. and T. Chen, *Gaussian process regression with multiple response variables.* Chemometrics and Intelligent Laboratory Systems, 2015. **142**: p. 159-165.

127. Liu, H., J. Cai, and Y.-S. Ong, *Remarks on multi-output Gaussian process regression.* Knowledge-Based Systems, 2018. **144**: p. 102-121.

128. Sen, I., et al., *Microstructural effects on the mechanical behavior of B-modified Ti–6Al–4V alloys.* Acta Materialia, 2007. **55**(15): p. 4983-4993.

129. Roy, S., et al., *Development of solidification microstructure in boron-modified alloy Ti–6Al–4V–0.1 B.* Acta Materialia, 2011. **59**(14): p. 5494-5510.

130. Attallah, M., et al., *Comparative determination of the α/β phase fraction in α+ β-titanium alloys using X-ray diffraction and electron microscopy.* Materials characterization, 2009. **60**(11): p. 1248-1256.

131. Collins, P.C., et al., *Development of methods for the quantification of microstructural features in α+ β-processed α/β titanium alloys.* Materials Science and Engineering: A, 2009. **508**(1-2): p. 174-182.

132. Lütjering, G., *Influence of processing on microstructure and mechanical properties of (α+ β) titanium alloys.* Materials Science and Engineering: A, 1998. **243**(1-2): p. 32-45.

133. McDowell, D.L., *Simulation-assisted materials design for the concurrent design of materials and products.* JOM, 2007. **59**(9): p. 21-25.

134. Choi, H.-J., et al. *An inductive design exploration method for the integrated design of multi-scale materials and products*. in *International Design Engineering Technical Conferences and Computers and Information in Engineering Conference*. 2005.

135. Choi, H., et al., *An inductive design exploration method for robust multiscale materials design.* Journal of Mechanical Design, 2008. **130**(3).

136. Pedregosa, F., et al., *Scikit-learn: Machine learning in Python.* the Journal of machine Learning research, 2011. **12**: p. 2825-2830.

137. Choi, H.-J., et al., *An approach for robust design of reactive power metal mixtures based on non-deterministic micro-scale shock simulation.* Journal of Computer-Aided Materials Design, 2005. **12**(1): p. 57-85.

138. Stopka, K.S. and D.L. McDowell, *Microstructure-sensitive computational multiaxial fatigue of Al 7075-T6 and duplex Ti-6Al-4V.* International Journal of Fatigue, 2020. **133**: p. 105460.

139. Fatemi, A., et al., *Torsional fatigue behavior of wrought and additive manufactured Ti-6Al-4V by powder bed fusion including surface finish effect.* International Journal of Fatigue, 2017. **99**: p. 187-201.

140. Shamsaei, N., et al., *Multiaxial fatigue of titanium including step loading and load path alteration and sequence effects.* International Journal of Fatigue, 2010. **32**(11): p. 1862-1874.

141. Hoshide, T., E. Kakiuchi, and T. Hirota, *Microstructural effect on low cycle fatigue behaviour in Ti-alloys under biaxial loading.* Fatigue & Fracture of Engineering Materials & Structures, 1997. **20**(6): p. 941-950.

142. Wu, Z.-R., X.-T. Hu, and Y.-D. Song, *Multiaxial fatigue life prediction for titanium alloy TC4 under proportional and nonproportional loading.* International Journal of Fatigue, 2014. **59**: p. 170-175.

143. Baumeister, T. and A.M. Sadegh, *Marks' standard handbook for mechanical engineers*. Vol. 1. 1978: McGraw-Hill New York.

144. Smith, B.D., *Microstructure-sensitive plasticity and fatigue of three titanium alloy microstructures*. 2013, Georgia Institute of Technology.

145. Asaro, R.J., *Micromechanics of crystals and polycrystals.* Advances in applied mechanics, 1983. **23**(1): p. 115.

146. McGinty, R., *Multiscale representation of polycrystalline inelasticity Ph. D*. 2001, thesis. Georgia Institute of Technology, Atlanta.

147. Mayeur, J.R., *Three dimensional modeling of Titanium-Aluminum alloys with application to attachment fatigue*. 2004, Citeseer.

148. Bridier, F., et al., *Crystal plasticity modeling of slip activity in Ti–6Al–4V under high cycle fatigue loading.* International Journal of Plasticity, 2009. **25**(6): p. 1066-1082.

149. Armstrong, P.J. and C. Frederick, *A mathematical representation of the multiaxial Bauschinger effect*. Vol. 731. 1966: Central Electricity Generating Board [and] Berkeley Nuclear Laboratories ….

150. Naka, S., et al., *The low-temperature plastic deformation of α-titanium and the core structure of a-type screw dislocations.* Philosophical Magazine A, 1988. **57**(5): p. 717-740.

151. Qin, Q. and J.L. Bassani, *Non-Schmid yield behavior in single crystals.* Journal of the Mechanics and Physics of Solids, 1992. **40**(4): p. 813-833.

152. McGinty, R.D., *Multiscale representation of polycrystalline inelasticity.* 2002.

153. Ohno, N. and J.-D. Wang, *Kinematic hardening rules with critical state of dynamic recovery, part I: formulation and basic features for ratchetting behavior.* International journal of plasticity, 1993. **9**(3): p. 375-390.

154. McDowell, D., *Stress state dependence of cyclic ratchetting behavior of two rail steels.* International Journal of Plasticity, 1995. **11**(4): p. 397-421.